TECHNISCHE UNIVERSITÄT MÜNCHEN
Lehrstuhl für Biologische Bildgebung
Chair for Biological Imaging

Real-time Optoacoustic Monitoring of Ablation Treatments in Medicine

Dipl.-Ing. Erwin Bay

Vollständiger Abdruck der von der Fakultät für Elektrotechnik und Informationstechnik der Technischen Universität München zur Erlangung des akademischen Grades eines

Doktor-Ingenieurs

genehmigten Dissertation.

Vorsitzender: Univ.-Prof. Dr. Bernhard Wolf

Prüfer der Dissertation:

1. Univ.-Prof. Vasilis Ntziachristos, Ph.D.
2. Univ.-Prof. Dr.-Ing. Christian Jirauschek

Die Dissertation wurde am 06.10.2015 bei der Technischen Universität München eingereicht und durch die Fakultät für Elektrotechnik und Informationstechnik am 27.02.2016 angenommen.

Contents

Abstract

Therapeutic procedures based on tissue ablation have been applied in various medical fields for the purpose of removing or destroying diseased tissues, such as tumors or malfunctioning cardiac tissue. Although tissue ablation has been increasingly used in clinical practice replacing conventional surgical or medicative treatments, the lack of sensory feedback during ablation procedures still yields a non-negligible risk of ineffective treatments or collateral damage to healthy surrounding tissues, causing repeated treatments or severe complications, respectively.

The aim of this work was therefore to investigate how Optoacoustics, a promising and versatile modality in Biomedical Imaging and Sensing, can be utilized to monitor biophysical processes occurring during ablation, in order to provide direct and precise feedback on the outcome of the ablation procedure. To cover all biophysical processes and corresponding alterations of tissue structure and composition, two fields of clinical ablation treatments were covered in this work: laser ablation aiming at removing diseased tissues and radio-frequency cardiac ablation with the objective of destroying malfunctioning cardiac muscle tissue. For both fields, novel optoacoustic monitoring techniques were developed and tested in *ex vivo* studies. As shown by the experimental results, Optoacoustics holds great potential of providing valuable real-time feedback on the ablation parameters that are most critical for treatment success, in laser ablation as well as in radio-frequency cardiac ablation. Limitations of the current monitoring methods and prototypes were identified and technological solutions for future development towards clinical prototypes were specified.

Publications, Conference Proceedings and Talks

Publications in Peer-Reviewed Journals

[1] Erwin Bay, Alexandre Douplik, Daniel Razansky, "Optoacoustic monitoring of cutting efficiency and thermal damage during laser ablation", *Lasers in Medical Science*, **29**(3), p. 1029-1035, May 2014

[2] Erwin Bay, Xose Luís Deán-Ben, Genny A. Pang, Alexandre Douplik, Daniel Razansky, "Real-time monitoring of incision profile during laser surgery using shock wave detection", *Journal of Biophotonics*, **8**(1-2), p. 102-111, Jan 2015

[3] Genny A. Pang*, Erwin Bay*, Xose Luís Deán-Ben, Daniel Razansky, "Three-dimensional optoacoustic monitoring of lesion formation in real time during radiofrequency catheter ablation", *Journal of Cardiovascular Electrophysiology*, **26**(3), p. 339-345, Mar 2015 (*authors contributed equally)

[4] Xose Luís Deán-Ben, Erwin Bay, Daniel Razansky, "Functional optoacoustic imaging of moving targets using microsecond-delay acquisition of multispectral three-dimensional tomographic data", *Nature: Scientific Reports 4*, article number 5878, published online Jul 2014

Conference Proceedings

[1] Erwin Bay, Alexandre Douplik, Daniel Razansky, "Optoacoustic monitoring of cutting and heating processes during laser ablation", *Proceedings of SPIE 8581*, March 2013

[2] Erwin Bay, Xose Luís Deán-Ben, Genny A. Pang, Alexandre Douplik, Daniel Razansky, "Three-dimensional tracking of lesion profile during laser surgery based on shock wave detection", *Proceedings of SPIE 8943*, March 2014

Talks and Posters

[1] Erwin Bay, Alexandre Douplik, Daniel Razansky, "Monitoring of Pressure Waves induced during Laser Ablation", *Oral Presentation at ASLMS Annual Conference*, April 2012

[2] Erwin Bay, Alexandre Douplik, Daniel Razansky, "Optoacoustic monitoring of cutting and heating processes during laser ablation", *Poster Presentation SPIE Photonics West*, February 2013

[3] Erwin Bay, Xose Luís Deán-Ben, Genny A. Pang, Alexandre Douplik, Daniel Razansky, "Three-dimensional tracking of lesion profile during laser surgery based on shock wave detection", *Oral Presentation SPIE Photonics West*, February 2014

1 Introduction

1.1 Motivation

1.1.1 Ablation therapies in Medicine

Tissue ablation can be defined as the therapeutic use of heat for the purpose of destroying or removing unhealthy tissue. Many types of energy sources can be utilized for different therapeutic purposes, including laser light [1, 2], focused ultrasound [3], radio-frequency current [4] and microwave fields [5]. The energy source is employed in a way to create a desired outcome in the treated tissue volume, spanning from mild temperature rise to coagulation, carbonization or tissue removal.
Therapeutic procedures based on tissue ablation have been successfully applied in various fields such as cardiology, oncology and ophthalmology. In radio-frequency ablation of the heart [6], a widely used treatment of cardiac arrhythmia, heat is delivered into the cardiac muscle in order to destroy tissue related to faulty electric pathways with the effect of restoring correct cardiac rhythm. Fig.1.1 demonstrates clinical application of radio-frequency cardiac ablation. As can be obtained from the clinical setup in Fig.1.1(a), a RF generator is used to provide radio-frequency current for the treatment, typically at a frequency of 500KHz. In order to deliver the current to the target area within the cardiac muscle, a catheter is inserted through the femoral vein and advanced into the cardiac chamber, as shown in Fig.1.1(b). After the exact target location has been identified based on electric potential measurements along the cardiac wall, electric current is conducted through an electrode at the catheter tip into the cardiac muscle. Resistive heating leads to significant rise in temperature and irreversible coagulation of myocardial tissue (Fig.1.2). Due to a much smaller surface area of the tip electrode compared to the area of the grounding pad, current density is much higher at the tip electrode. As a consequence, thermal ablation is

confined to a small volume in the vicinity of the catheter tip, yielding a lesion of a depth on the order of several millimeters.

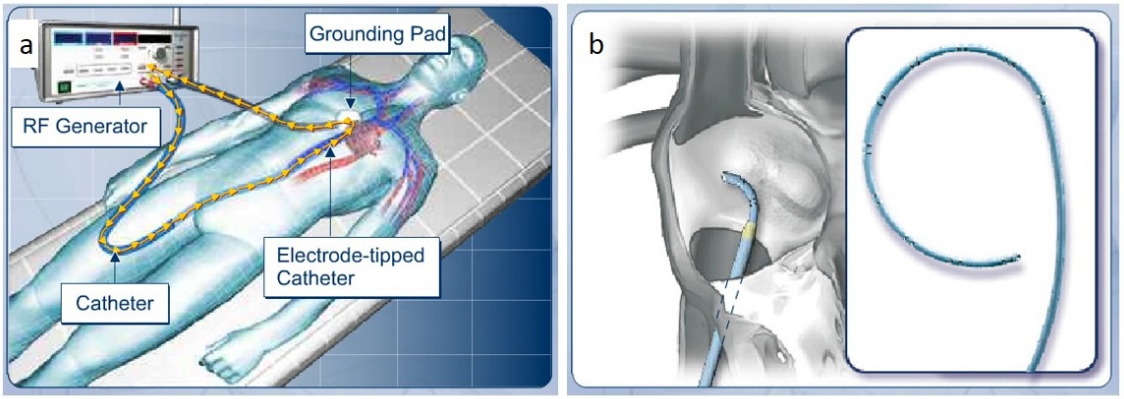

Figure 1.1: (a) clinical setup of radio-frequency cardiac ablation. (b) catheter inserted into cardiac chamber. (Images courtesy of Biosense Webster Inc.)

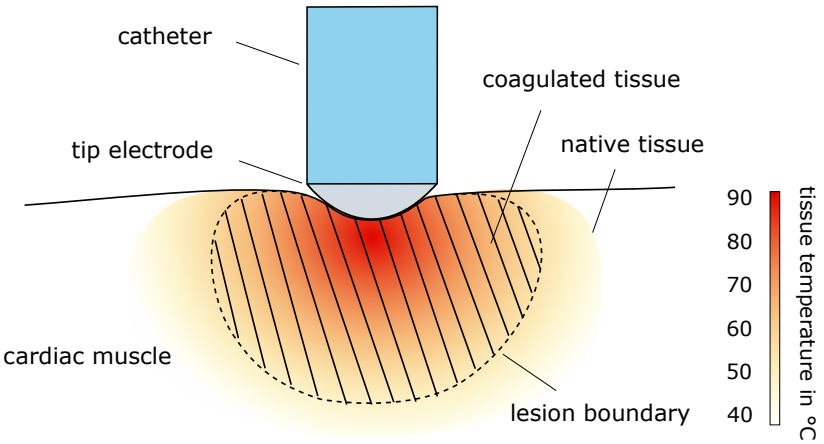

Figure 1.2: Schematic showing lesion in the cardiac muscle generated during radio-frequency ablation

Similarly, in thermal ablation of tumors [7–9], often referred to as local hyperthermia, heat is selectively delivered into the tumor in order to induce coagulation and to destroy cancer cells. In contrast, only low levels of energy are used in regional or whole-body hyperthermia to fight cancer [10]. The resulting mild increase in temperature improves the effectiveness of conventional treatments such as radiation or chemotherapy, which are performed concurrently.

Other applications of tissue ablation are characterized by significantly higher levels of

energy density. In laser ablation, as used in a multitude of surgical procedures [11–13], focused high energy laser light is used to remove or excise various types of soft or hard tissues. For instance, laser light can be applied to create very precise incision profiles in bone tissue (Fig.1.3), as showcased in an *ex vivo* study for laser osteotomy [14].

Figure 1.3: result of ablation procedure in laser osteotomy. (Reprinted with permission from [14]. Copyright 2005, Elsevier GmbH)

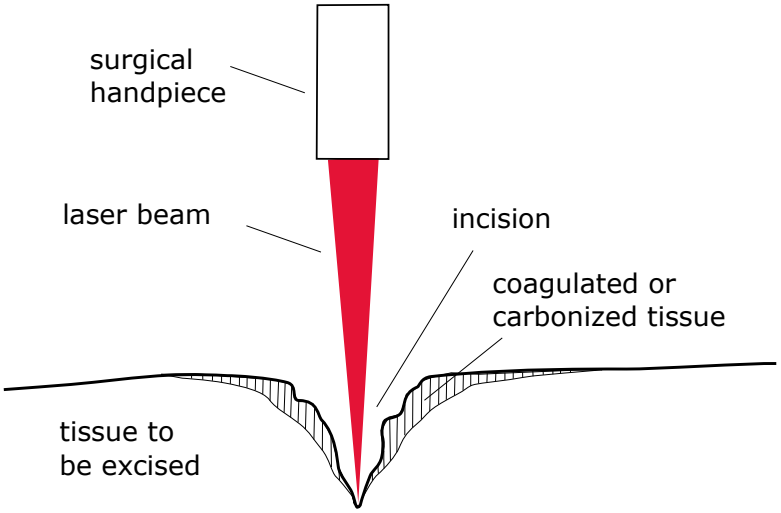

Figure 1.4: Schematic showing incision generated during laser ablation

Due to high energy density of the surgical laser beam, absorption of optical energy leads to explosive vaporization and tissue removal in the focus of the beam. As a side effect,

a fraction of optical energy is absorbed in the surrounding tissue generating a margin of coagulated tissue around the incision profile, as shown in Fig.1.4. In many applications of surgical lasers, coagulation of surrounding tissue is highly desirable, since it leads to hemostasis and significantly less bleeding than in applications using mechanical scalpels [15].

1.1.2 Need for sensory feedback

Most current ablation procedures rely solely on indirect indicators of ablation activity, such as the overall duration of the treatment, the delivered power or the resulting temperature measured in a single point, e.g. on the tissue surface. Based on indirect indicators, the geometry of the lesion or incision can merely be estimated, yielding judgements highly sensitive to experience and training. The size of a lesion might therefore be over- or underestimated, leading to an extent of tissue damage that is either insufficient, requiring repeated treatments, or excessive, causing undesired thermal damage to adjacent tissues and potentially serious, life-threatening complications, such as atrio-esophageal fistulae or cardiac tamponade in the case of radio-frequency ablation of the heart [16]. Similarly, while performing deep incisions in laser surgery, lack of haptic feedback leads to difficulties discerning the incision depth and incised tissue type causing a high risk of collateral damage to critical tissues that need to be preserved, such as blood vessels or nerves [17, 18]. A direct assessment of ablation activity, for instance by imaging the lesion or incision created during ablation, can provide reliable and accurate measurements of lesion size and incision profile, vastly improve decision making and ultimately yield more effective and much safer treatments.

1.2 Biophysics of thermal ablation

1.2.1 Coagulation and Carbonization

Sustained heating during thermal ablation leads to coagulation and carbonization of the heated tissues. Coagulation, mainly driven by heat induced alterations of proteins, depends on temperature and heating duration. Tissue is widely regarded as fully coagulated when heated at a constant reference temperature of 43° C for a duration of 240 minutes [19]. Moreover, a simple exponential relationship exists between temperature and heating duration [20], namely, above 43° C a one degree increase in temperature requires a two-fold decrease in exposure time for attaining the same effect. Consequently, at temperatures above 50° C tissue will be fully coagulated in less than a minute, at temperatures above 56° C in less than a second. Due to the change in its composition, coagulated tissue experiences a change in mechanical and optical properties compared to native tissue. For temperatures exceeding 100° C, the intracellular water in the remaining tissue will start boiling off, leaving carbonized tissue fragments. This biophysical process is referred to as carbonization or charring and yields very hard and dark tissue, typically in thin layers or fragments on the surface of the heated object.

1.2.2 Tissue Removal

A critical parameter in laser surgery is the ablation threshold. Under thermal confinement conditions, if the radiant exposure of a single laser pulse exceeds this tissue-specific threshold, the irradiated tissue will exhibit an explosive vaporization of intracellular water, leading to the ejection of water vapor and tissue fragments [2]. Thus, a certain tissue volume will be removed from the ablation site creating an incision, as shown in Fig.1.4. A fraction of incident laser light penetrates to a depth where the absorbed optical energy is not high enough to remove the tissue. As a result, the energy absorbed by the remaining tissue will be converted into heat leading to an increase in tissue temperature. This is particularly the case when optical energy is deposited at high repetition rates. Absorbed energy will accumulate over several consecutive pulses and lead to coagulation and carbonization in the remaining tissue.

1.3 Optoacoustics for monitoring of ablation

1.3.1 Principles of Optoacoustic Imaging and Sensing

Optoacoustics, also known as photoacoustics, has been widely applied as a promising new imaging and sensing technique for Biomedical Applications [21, 22]. In earlier applications, optoacoustic imaging has been mostly used to obtain hemoglobin-based optical contrast, since hemoglobin is one of the strongest absorbers in biological tissue. Examples are breast tumor detection [23], imaging of tumor angiogenesis [24, 25] and superficial vasculature [26], or functional brain imaging by monitoring the blood-oxygenation status [27]. In 2007 a new imaging modality, Multispectral Optoacoustic Tomography (MSOT), was proposed for Small Animal Imaging of Mice [28, 29]. The MSOT technique has enabled novel, whole body biodistribution studies of molecular probes [30, 31] and promises to deliver novel contributions to pre-clinical research and drug discovery [32].
The wide range of possible biomedical applications is due to the fact that Optoacoustics combines the advantages of optical and acoustic imaging. As a hybrid modality it provides strong absorption based contrast of optical imaging and high resolution und penetration depth of ultrasound. To this end, Optoacoustics capitalizes on the optoacoustic effect, i.e. the generation of acoustic pressure waves due to thermoelastic expansion caused by absorption of short optical pulses in the nanosecond range. As visualized in the schematic in Fig.1.5(a-c), the amplitude of the detected optoacoustic pressure wave is proportional to the optical absorption of the illuminated tissue (Fig.1.5(c)). This principle makes the technique very sensitive to variations in optical absorption and capable of resolving different absorbers with high spatial accuracy. If pressure waves are collected from a multitude of positions, with sufficient observation angle, an image can be reconstructed that shows an absorption map of the irradiated tissue. If this procedure is repeated for several illumination wavelengths absorbers can be clearly identified based on their characteristic, wavelength-dependent absorption profile using a spectral unmixing algorithm [28].

1.3.2 Sensitivity to thermal damage

Several researchers have investigated the effect of thermal damage on optical properties. A strong increase in scattering coefficient was observed during coagulation [33, 34], but

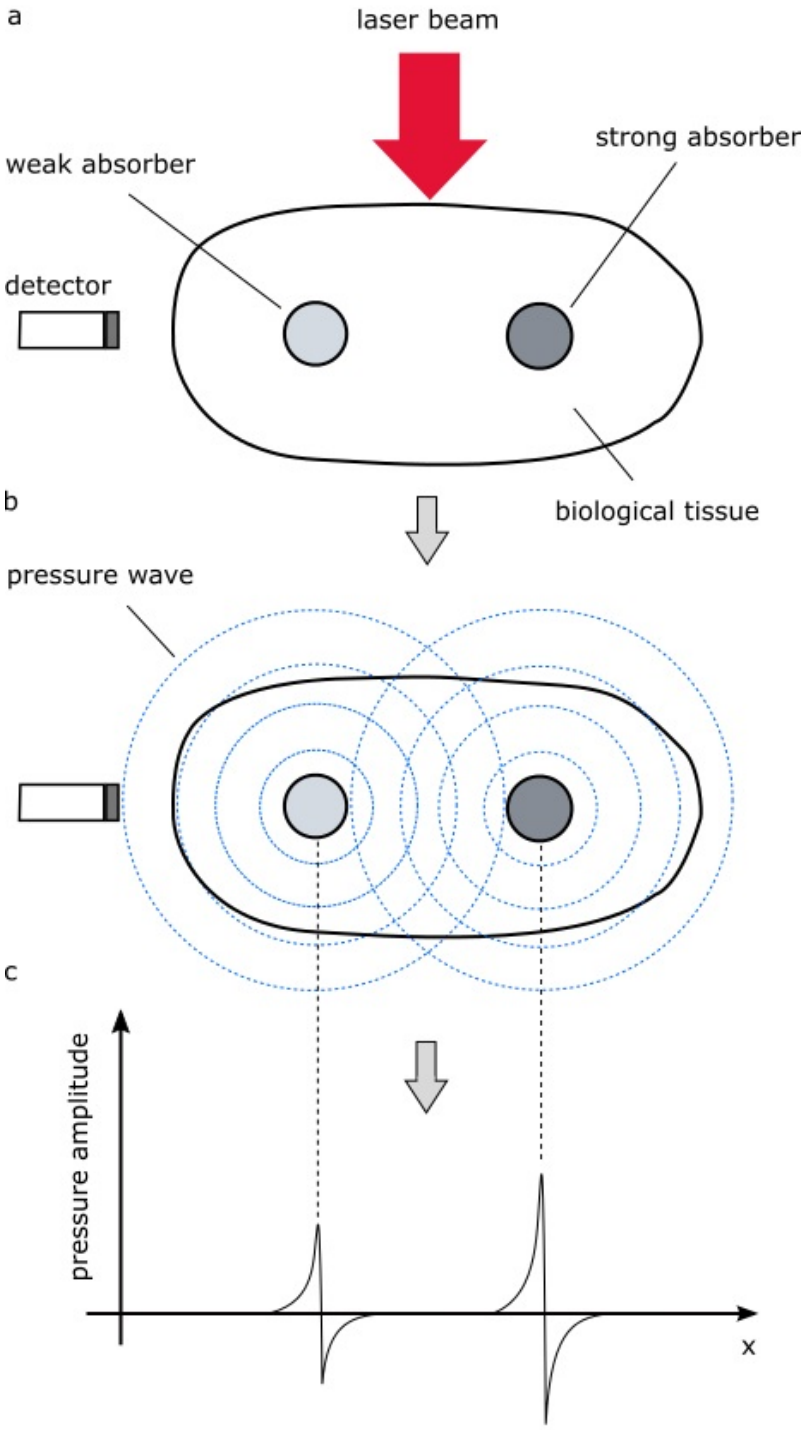

Figure 1.5: Schematic showing principle of optoacoustic sensing. (a) optical absorbers in tissue illuminated by short laser pulse (b) optocoustic pressure waves generated due to thermoelastic expansion (c) time-resolved signal of acoutic detector showing pressure signals

only minor or inconsistent dependency of optical absorption on temperature. However, the tissue samples used in these studies were purified from any residual blood, one of the major chromophores in many optoacoustic applications. Consequently, optoacoustic signals detected during coagulation of blood-rich tissues might also reflect differences between optical absorption of coagulated and native tissue.
An optoacoustic imaging study of in-vivo HIFU treatment of mouse kidneys showed a distinctive contrast between a zone of midly coagulated tissue of whitish appearance and the healthy background tissue [35]. Pixels representing coagulated tissue showed lower values than pixels representing vital background tissue. This negative contrast was attributed to a loss in concentration of water and oxygenated hemoglobin, the major chromophores at 1064nm, during the coagulation process. A thermally induced change in scattering properties was argued to be insignificant in case of mildly coagulated tissue and thus was not expected to contribute to the observed contrast. A recent imaging study performed after radio-frequency catheter ablation of myocardial tissue produced lesions containing highly coagulated tissue of brownish appearance surrounded by a transitional region of mildly coagulated, whitish tissue and the native background tissue [16]. Single-wavelength optoacoustic images showed an increase in signal within the strongly coagulated zone as compared to the surrounding tissues. A multi-wavelength analysis further revealed different spectral absorption profiles of strongly coagulated and native myocardial tissue.
There have been no studies so far investigating the effect of carbonization on the optoacoustic signal. However, owing to a drastic change in tissue color and the appearance of very dark, almost black charred tissue, an increase in optoacoustic signal amplitude can be naturally expected.
The distinct, inconsistent results of previous findings with respect to the effect of coagulation on the optoacoustic signal, can likely be explained by the different types of tissue used in the experiments (purified from blood vs non-prufied), the experiment type (*in vivo* vs *ex vivo*) or by the fact that different levels of thermal damage were induced (mild vs strong coagulation).

1.3.3 Detection of pressure waves

The absorption of pulsed laser light of a short duration on the order of several tens of nanoseconds leads to the generation of different types of pressure waves. Laser pulses with radiant exposures above the ablation threshold lead to explosive vaporization and

material ejection, followed by emission of a shockwave [2,36]. Pulses below the threshold lead to the optoacoustic effect followed by emission of a broadband optoacoustic wave. A good comparison of both signals can be found in the work of Esenaliev et al. [37].

1.3.4 Optoacoustics as promising modality for real-time feedback

Despite inconsistent results of previous work with respect to the effect of coagulation on optical properties [16, 33–35], likely due to variable experimental conditions, the optoacoustic technique seems to be very sensitive to heat-induced changes in optical properties and therefore might provide a very promising way to monitor thermal damage during ablation treatments. Moreover, ultrasonic sensors designed to detect optoacoustic pressure waves can in principle also be used to detect shockwaves emitted during tissue removal. Therefore, an optoacoustic feedback system might also be utilized to monitor the cutting process during laser ablation.

1.4 Thesis outline

The aim of this work was to investigate how Optoacoustics can be used in order to provide direct feedback during ablation procedures. To cover all possible biophysical processes, from coagulation and carbonization to tissue removal, two ablation treatments were covered in this work: radiofrequency catheter ablation of the heart and laser ablation for surgical procedures. The basic monitoring principles shown in this work, however, could also be adapted to other ablation treatments such as high intensity focused ultrasound and microwave ablation.
The second chapter of this thesis focuses on laser ablation and proposes several monitoring methods of varying complexity in order to overcome the difficulties of modern laser surgical procedures, i.e. collateral thermal damage and especially the lack of haptic feedback. The aim of the third chapter is to evaluate whether Optoacoustics can be used to monitor RF catheter ablation and to realize a specific monitoring principle and design that can be used in clinical treatments.

2 Optoacoustic Monitoring of Laser Ablation

2.1 Clinical Background: Surgical Applications of Lasers

Laser ablation has been so far widely applied in various surgical applications, ranging from ophthalmology to dermatology and oncology, owing to its several critical advantages over conventional scalpel based surgery [12, 17, 38]. In soft tissue applications, the fundamental advantage resides in the hemostatic effect of laser light. Besides tissue removal in the focus of the laser beam, the absorption of optical energy also causes heating of surrounding tissues. As a consequence, neighbouring blood vessels are sealed during coagulation [13, 17, 39, 40]. In this way, excessive bleeding can be avoided, leading to a simplified treatment protocol, reduced operational trauma and lower risk for malignant cells to be introduced into blood circulation [17].

2.2 Need for real-time monitoring

Although the use of the laser has become commonplace in several surgical applications of cutting hard and soft tissue, there are two major disadvantages of laser-induced cutting: the risk of collateral thermal damage and the lack of haptic feedback, which in turn can lead to undesired collateral damage to structures that need to be preserved such as nerve tissue. Real-time monitoring systems have a great potential to assist the surgeon with critical sensory information in order to better assess the ablation process within the target tissue and to prevent undesired results. In the future, a real-time sensory feedback might

even be used as a central part of a closed-loop control system in which all laser parameters, such as power and repetition rate, are automatically controlled to ensure an optimal incision of high precision and minimal collateral damage to surrounding tissues.
In this work, two studies were performed towards the goal of finding effective optoacoustic monitoring techniques for real-time feedback on the incision process. While the first study investigates how a cost-effective system comprising a single transducer can be used to assess thermal damage in surrounding tissues, the second study proposes a more elaborate, multi-element detector technique to reconstruct the three-dimensional incision profile during laser surgeries for precise depth profiling, which might reduce the risk of collateral damage arising from the lack of haptic feedback.
In addition to providing feedback on the incision process, optoacoustics might also be used in order to detect critical structures surrounding the incision. More specifically, a forward-looking optoacoustic sensing technique could detect critical structures, such as nerves, underneath the incision and might significantly increase safety when combined with three-dimensional incision profiling. To this end, experiments were performed towards distinguishing different tissue types, such as nerves and fat tissue, and preliminary results are shown at the end of the chapter.

2.3 Study 1: Optoacoustic monitoring of thermal damage and cutting efficiency

2.3.1 Motivation

A certain degree of coagulation of the soft tissues surrounding the incision is desirable in order to induce hemostasis, however, excessive coagulation or even carbonization may lead instead to extensive thermal damage to adjacent critical structures [13, 15, 41] and prolonged wound healing [42]. Successful laser surgery is thus characterized by an optimal trade-off between cutting and heating capabilities of the laser beam [41]. This, in turn, requires optimal control over several optical and mechanical parameters involved in the procedure. One can increase peak power of the laser to obtain a deeper cut while increasing pulse repetition rate may induce more coagulation [15]. At any given repetition rate and power settings, there is a strong dependence of cutting depth and extent of thermal damage on the speed at which the ablating beam transverses the target surface [43]. The

higher the beam velocity the lower is the cutting depth and the extent of thermal damage. As a consequence, in order to avoid complications, the surgeon should be able controlling various laser parameters and continuously observing their effects while moving the beam over the target surface [44]. This turns particularly challenging when surgical systems are operated remotely, as is often the case in many endoscopic and robot-guided surgeries. Therefore, any feedback system capable of delivering information about cutting efficiency or extent of thermal damage during the course of the procedure might prove valuable during treatment. A real-time closed-loop control system based on reliable sensory feedback of ablation activity could eventually alleviate cognitive load on surgeons by ensuring that the desired outcome, in terms of cutting depth or coagulation margin, is met. In this way, the surgeon could potentially move the beam intuitively and devote most attention to the specific target while avoiding the demanding task of concurrent control of the various laser parameters.

2.3.2 Overview of existing methods

There have been several attempts to establish optical or acoustic feedback systems during laser ablation [45–48]. Those were mainly directed towards discriminating different types of tissue, e.g. bone and nerve tissue, while monitoring of collateral thermal damage was not considered. Herein, we propose a novel ablation monitoring method based on the optoacoustic measurement technique. Generation of optoacoustic signals implies illuminating the sample with short intense pulses of laser radiation, whose absorption causes instantaneous heating and generation of ultrasonic waves propagating through the tissue [49]. By detecting the induced optoacoustic pressure waves, one can potentially determine optical absorption properties of the imaged tissue or, in fact, its color [22, 50]. It has been previously shown, that the optoacoustic technique is capable of reliably distinguishing vital and coagulated tissue [19, 35, 51], providing means to monitor thermal damage in real time. In this work, we demonstrate a method for direct detection of signals, emitted during the ablation process from tissue surrounding the ablation crater, which are further analyzed to provide an assessment of the collateral thermal damage. By comparing the optoacoustic data with shockwaves obtained during tissue removal, we are able to present, for the first time, how dynamics of the cutting and heating processes can be concurrently monitored during laser ablation of soft tissues. In practice, our method could potentially enable to keep track of the cutting efficiency of the laser beam as well as the ex-

tent of collateral thermal damage, eventually facilitating real-time control of laser ablation procedures.

2.3.3 Experimental design

An ex-vivo study was performed to investigate how both cutting and heating processes can be dynamically monitored using optoacoustics. For the experiments, fresh bovine muscle tissue from a slaughterhouse was used, for which no ethical approval was necessary. Care was taken to remove any fat or connective tissue from the specimen. In this way, cutting and thermal effects were only induced and monitored in a homogenous tissue volume, ensuring that any dynamic changes were solely due to ablative or thermal processes and not due to transitions between different tissue types.
The experimental setup is shown in Fig.2.1(a). The study was performed in a tank (300*150*40mm) filled with water at room temperature (20°C) in order to ensure good acoustic coupling between ultrasound transducer and the sample. Laser ablation and generation of optoacoustic signals was performed using a single frequency-doubled, Q-switched Nd-YAG laser (Edgewave GmbH, Germany) operating at 532nm. Additionaly, there was remanent infrared radiation at 1064 nm collinear with the 532nm beam. However, the infrared component contributed to less than 0.1% of the output energy and had therefore negligible effect on ablation and optoacoustic signal generation. Due to the short pulse duration of only 7.6ns (full width at half maximum), the laser was able to excite optoacoustic waves in tissue surrounding the ablation crater. At the same time, due to high optical absorption of blood and myoglobin at 532 nm, the laser was able to efficiently ablate with 4.5 mJ energy per pulse. Furthermore, due to the high pulse repetition rate of 4 kHz, resulting in an average power of 18W, it was also possible to cause significant thermal damage to adjacent tissues. The laser beam was guided into the water tank and focused onto the surface of a slab of fresh bovine muscle tissue (40*40*15mm) using a 50 mm lens adjusted by a manual translational stage (Thorlabs, Newton, NJ). In order to obtain accurate focusing, a digital camera (Canon EOS 550) was used to provide visual feedback. Additionally, laser safety glasses, having an OD of >7 in the wavelength range below 532nm (Thorlabs, Newton, NJ), were mounted in front of the camera to prevent damage to the CCD. From the photograph (Fig.2.1(b)), the distance of the focal spot from the tissue surface and the fluence could be estimated.

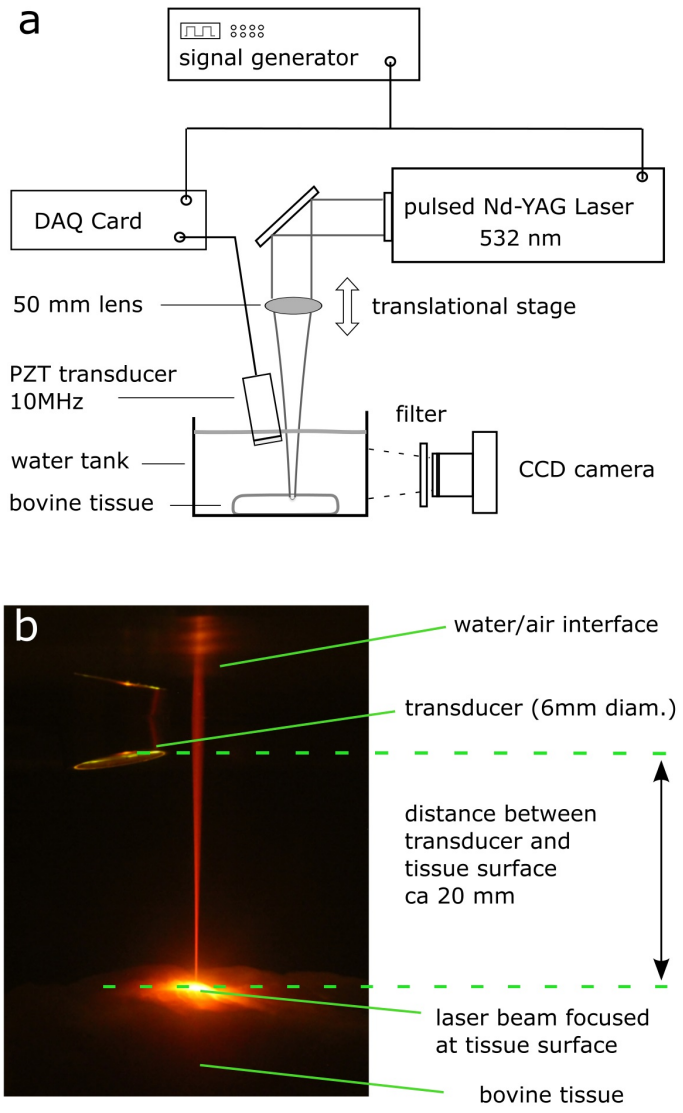

Figure 2.1: (a) Schematics of the experimental setup. (b) Photograph of the experiment. In order to avoid damage to the CCD, a filter was placed in front of the camera with high attenuation at 532 nm, which caused the image to appear red. (Figure published in [52], Copyright 2013, Springer-Verlag London)

Acoustic pressure waves were detected by an unfocused PZT transducer with a central frequency of 10 MHz and element diameter of 6mm (Model V312, Panametrics-NDT, Waltham, MA), placed at a distance of 20mm from the surface of the tissue. In order to maximize the sensitivity of the transducer, the angle between its axis and the laser beam was reduced to 10°. A 14-bit resolution PCI data acquisition card with a sampling

rate of 100 MS/s (NI PCI-5122, National Instruments Corp., Austin, TX) was utilized to record time-resolved signals. Data acquisition was controlled via a Labview-based interface (National Instruments Corp., Austin, TX). Laser pulse generation and acoustic data acquisition were both triggered externally by a signal generator (TTi Ltd, Huntingdon, UK) using a sequence of TTL pulses at 4KHz. Due to acoustic reflections at the walls of the water tank as well as the water-air interface, signals were overlaid by strong reverberations with frequencies extending up to about 30 KHz. These low frequency artifacts were removed using a Butterworth highpass filter with a cut-off frequency at 100 KHz, which has preserved the effective optoacoustic signal spectrum contained at higher frequencies. In order to better analyze and distinguish the different types of acoustic pressure waves, signals were further filtered by an array of bandpass filters, each one representing a digital Butterworth filter with bandwidth of 100 KHz. The peak-to-peak values of the filtered signals were subsequently analyzed, leading to a two dimensional map for the entire pulse train, with pixels indicating the peak to peak value for a specific pulse and spectral band. Since the very same laser pulses were used for both tissue ablation and generation of optoacoustic responses, two types of signals can be expected. In case of an ablation event, i.e. when absorption of optical energy at high irradiance leads to explosive vaporization and tissue removal, a shockwave is anticipated. When the irradiance at tissue surface was not high enough to cause ablation, the absorbed energy will instead lead to induction of thermoelastic expansion of the irradiated tissue volume. This reversible process thus leads to the emission of optoacoustic pressure waves. It is also well known that shockwaves generated by explosive vaporization as well as optoacoustic pressure waves induced via thermoelastic expansion may both significantly vary in their shape and amplitude [37, 53].

2.3.4 Results

Various experiments were carried out using different parameter settings for repetition rate (1, 2 or 4 kHz) and fluence at tissue surface (5 or 10 J/cm2). Each experiment was performed on a slab of fresh bovine muscle tissue for a duration of 1s. In this way, a suitable set of parameters that would lead to reproducible results characterized by a deep cut and excessive thermal damage, has been experimentally determined. The best result was attained at 4 kHz repetition rate with light fluence at tissue surface reaching approximately 10 J/cm2. In order to showcase how both cutting and thermal damage can be monitored

concurrently, the following analysis will focus on data obtained during this particular experiment.
As can be seen in the cross section photograph (Fig.2.2), tissue has been removed from the ablation zone, leaving a crater of nearly 1mm depth. Additionally, a large desaturated area of coagulated tissue as well as some dark-color carbonized tissue fragments can be clearly observed in the picture.

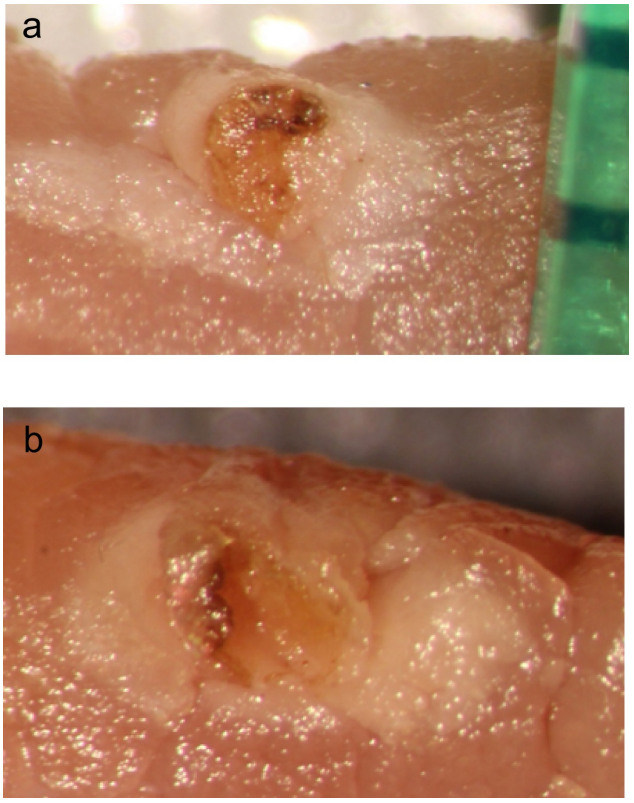

Figure 2.2: (a-b) Result of the ablation experiment with optimal parameter settings. Both sides of a crosssectional cut shown. Ruler increment corresponds to 1 mm.

Fig.2.3(a) shows signal recorded by the transducer for the first pulse out of the total number of 4000 pulses transmitted onto the tissue. A typical shockwave, having characteristic discontinuity at its leading edge and high peak-to-peak amplitude of around 200mV, can be observed in this case. In contrary, there was apparently no ablation event created for instance by pulse 22 (Fig.2.3(b)). Here only thermoelastic expansion of the irradiated tissue occurred, leading to an optoacoustic signal with a characteristic N-shaped form and significantly lower peak-to-peak amplitude in the range of 10mV.

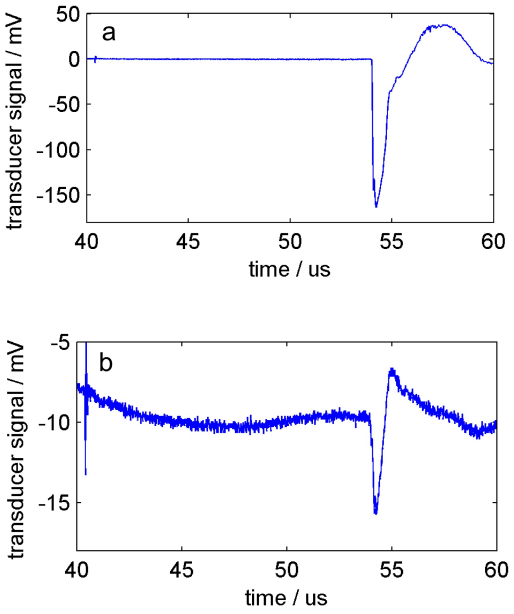

Figure 2.3: Typical acoustic responses, resulting from absorption of laser pulses by tissue, as recorded by the ultrasonic transducer. (a) The recorded response from the 1st pulse (out of a total of 4000 recorded pulses), corresponding to a typical shockwave. (b) The 22nd recorded response, representing a normal optoacoustic response that was not due to ablation. (Figure published in [52], Copyright 2013, Springer-Verlag London)

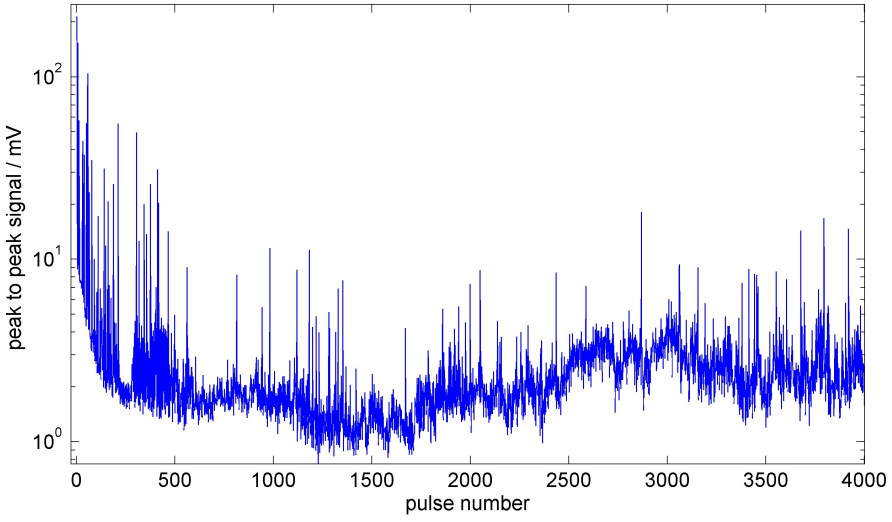

Figure 2.4: Peak-to-peak amplitude of the detected acoustic responses for the complete recorded pulse train. (Figure published in [52], Copyright 2013, Springer-Verlag London)

As revealed by the analysis of the peak-to-peak values of the entire pulse train (Fig.2.4), many signals with high peak-to-peak amplitude appeared in the beginning of the pulse train, which indicated successful removal of tissue. Later in time, considerable reduction in the shockwave amplitude occurred as more material has been removed from the focal zone of the laser beam.

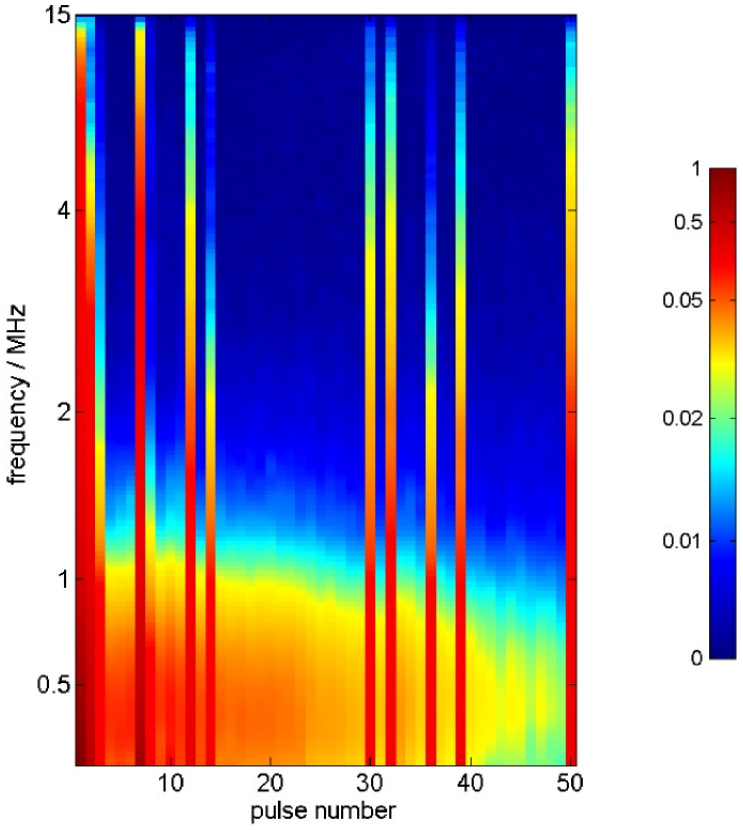

Figure 2.5: Filterbank analysis of the first 50 pulses. The frequencies have been scaled logarithmically in order to emphasize low frequency information (optoacoustic background signal) in more detail. Also note that the colors in the image are scaled nonlinearly over the presented dynamic range in order to provide more contrast for the optoacoustic signals in lower 5% of the dynamic range. (Figure published in [52], Copyright 2013, Springer-Verlag London)

In order to better distinguish the two classes of signals, their spectral characteristics were analyzed by filterbank analysis of the entire pulse train. For better visualization, Fig.2.5 only shows the spectral content of the first 50 recorded pulses. As can be readily recog-

nized, two very distinct classes of signals exist. The abrupt vertical lines indicate shockwaves from the ablated tissue as opposed to a continuous background signal representing the optoacoustic responses from the surrounding tissue. Due to nonlinear acoustic effects (discontinuity at leading edge), shockwaves cover a much broader range of frequencies up to 15 MHz, the upper bound of detection bandwidth of the transducer. On the other hand, the optoacoustically-generated signals, attributed to thermoelastic expansion of a bulky tissue volume, cover a significantly lower frequency range of up to 1.5 MHz and are further characterized by relatively low magnitude in the lower 5% of the dynamic range.
In order to selectively observe the dynamics of shockwaves, it is necessary to separate those from other responses not corresponding to the ablation events. This can readily be accomplished by image processing in the spectral domain where shockwaves appear as sharp broadband lines, as demonstrated in Fig.2.5.

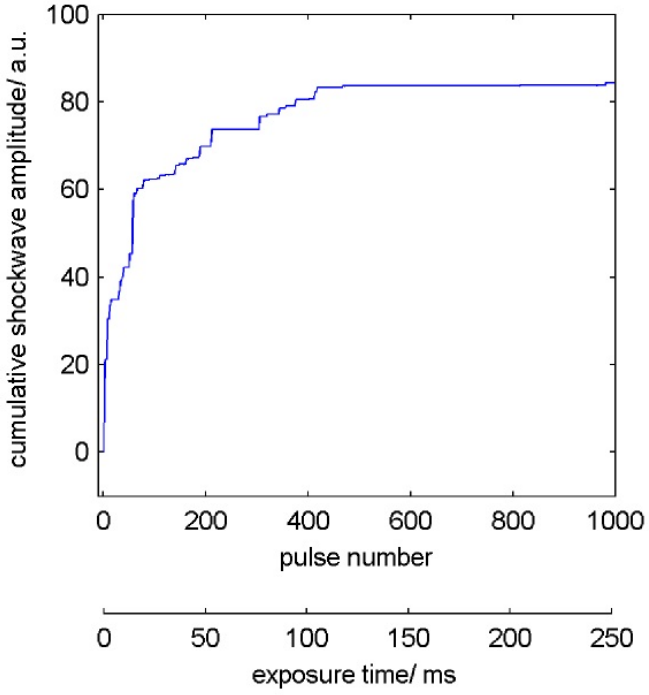

Figure 2.6: Cumulative shockwave amplitude for the first 1000 pulses. The graph was obtained by summation of peak to peak amplitude values along frequency dimension and subsequent integration along pulse dimension. Only shockwaves were taken into account for the calculation. (Figure published in [52], Copyright 2013, Springer-Verlag London)

In this way, after selecting the ablative pulses, the cumulative amplitude of the shock-

waves has been calculated (Fig.2.6). The data clearly shows a logarithmic increase until saturation is reached around pulse 500, i.e. ablation events no longer occur. On the other hand, if only optoacoustic responses are to be analyzed, it is convenient to remove the shockwave-related sharp lines from the spectral map. Fig.2.7 shows the spectrum of the background optoacoustic signals, obtained after removal of shockwaves, for the entire duration of the pulse train (4000 consecutive pulses).

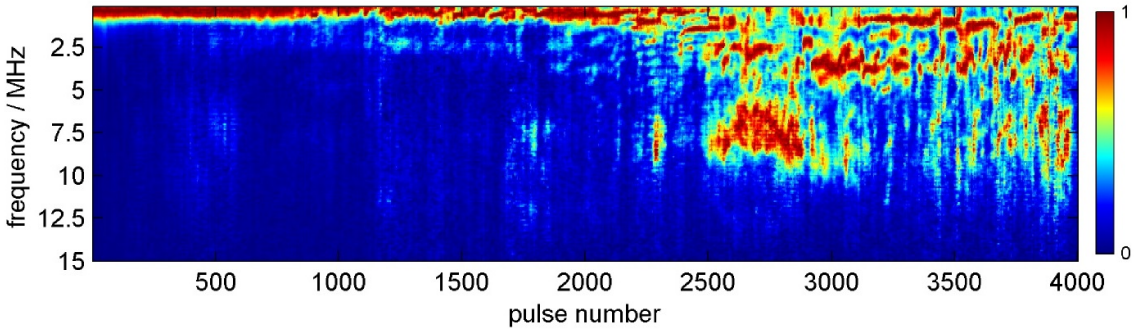

Figure 2.7: Filterbank analysis of the entire pulse train after removal of the shockwaves and interpolating the spectra of the corresponding pulses. Note that the values of each pulse were pulse-wise, linearly scaled to the range 0-1 in order to highlight the relative distribution of spectral energy with a value of 1 showing the maximum energy for each pulse. The result is particularly useful to highlight how the relative distribution of spectral energy changes over the pulse train.

Analysis of the spectral distribution of optoacoustic signals in Fig.2.7 reveals a significant shift in spectral content around pulse 2500. While in earlier pulses optoacoustic signal energy was mainly distributed in the lower frequency band of up to 1.5 MHz, the spectral content of the later optoacoustic pulses is being distributed over several distinct clusters extending up to frequencies in the 10 MHz range.

2.3.5 Discussion

Several interesting observations arise from the experimental results demonstrated in this study. For instance, long windows of non-ablative pulses can be readily recognized in Fig.2.5 (e.g. from pulse 16 to 29), which are eventually followed by a sudden occurrence of a shockwave. A possible explanation relies on the fact that, following removal of a

considerable amount of tissue, the remaining tissue is located further away from the focal zone of the laser beam, thus, the laser fluence is not high enough to cause ablation. As a result, over the following pulses, optical energy would only lead to heating and water evaporation, lowering the temperature-dependant ablation threshold until further ablation can eventually be induced. As can be also recognized, intensity of optoacoustic responses gradually decreases. A possible explanation would again be decrease in laser fluence on the surface due to tissue removal. However, as obtained from a closer analysis of pulses 15 to 29, the observed gradual change in the optoacoustic spectrum also takes place between two ablating pulses and therefore cannot be explained by tissue removal. Hence, it is likely to be concluded that the observed decrease in optoacoustic signal intensity can be attributed to coagulation effects around the ablation crater, accompanied by change in optical properties of the surrounding tissue. More specifically, a decrease in absorption coefficient might be caused by a loss in concentration of tissue chromophores (blood and myoglobin at 532nm), whereas an increase in scattering coefficient is likely to reflect changes in molecular composition due to protein denaturation. Besides lower absorption, increased scattering might also lead to a weaker optoacoustic response due to lower fluence in the surrounding tissue volume. Both phenomena, namely, decrease in absorption and increase in scattering coefficients, have been previously reported during coagulation [33–35]. Either of which or the combination of both, may serve as a plausible explanation for the observed loss in optoacoustic signal amplitude.
As can be readily observed from the results shown in Fig.2.6, after a considerable amount of tissue has been removed, ablation events become less frequent and of lower intensity, indicating that the cutting efficiency of the laser beam decreases over time. In particular, after 600 pulses there is no more removal of tissue, meaning that any further irradiation will only lead to thermal damage. In practice, this information can be used for decision-making regarding the optimal positioning of the laser beam, e.g., in order to prevent further collateral damage to the surrounding tissue, the focus of the laser beam can be moved deeper into tissue or shifted along the tissue surface to another location.

The significant change in spectral characteristics of optoacoustic signals after approximately 2500 pulses, as can be evinced from Fig.2.7, reflects an effective transition from a homogeneous volume of coagulated tissue into a heterogeneous volume containing several carbonized tissue fragments consequently formed during further heating. Due to their small size and very dark highly absorbing color, these charred tissue fragments are very likely to emit optoacoustic waves with much higher frequency components than the bulky

surrounding tissue. Moreover, the strong variability of emerging and disappearing signal clusters might bear witness to the formation of highly absorbing charred layers and their subsequent removal, presumably due to evaporation after further exposure to laser light. Furthermore, a delay exists between the two significant events, i.e. the end of tissue removal around pulse 600 (Fig.2.6) and the onset of carbonization around pulse 2500 (Fig.2.7). In our experiment, using energy of 4.5mJ per-pulse at a repetition rate of 4 kHz, the delay corresponded to ca. 1900 pulses or 0.48 sec.

In summary, the experimental data show that our method can be used to observe both the cutting efficiency in the focal zone as well as the dynamics of thermal damage in the surrounding tissue. Moreover, this can be achieved with a simple, inexpensive setup using one transducer and a single laser for ablation and optoacoustic monitoring. Widely available and highly optimized GPU based algorithms are able to perform spectral analysis of time-resolved signals of similar size (as in our experiments) on the order of several tens of microseconds. Exploiting these algorithms, our optoacoustic method could eventually be used for real-time feedback during laser surgery.
It has to be noted that, in order to investigate the basic monitoring principle, several simplifications were allowed in our ex-vivo study. First, only homogenous samples of bovine muscle tissue were ablated. Results will likely vary when heterogeneous samples are employed. For instance, the amplitude of shockwaves might change when connective or bone tissue is ablated instead of muscle tissue. In this case, the proposed method might need to be adapted and reevaluated. On the other hand, it might also prove beneficial in distinguishing different tissue types. Second, in order to provide acoustic coupling, the experiment was performed in a water tank. For clinical applications, coupling has to be maintained by different means. Given the trend towards contact laser scalpels [44, 54], a possible solution might be to integrate a compact acoustic detector within the same probe. It has to be further noted that the water used in our experiment likely acted as a heat sink, inducing an effect similar to laser cooling systems. Nevertheless, with suitable laser settings, we were still able to induce a significant degree of thermal damage. Clearly, in a different experimental setup with less or no water (as in a contact-based approach), the overall dynamics of ablation and thermal damage might vary. For instance, carbonization could have been induced much earlier during the pulse train. Third, our method was only tested using light at 532nm. Even though water is weakly absorbing at this wavelength, ablation and generation of optoacoustic responses still occurred in our experiments but mainly due to the strong absorption of the residual blood and myoglobin at this wave-

length. In clinical applications, a variety of lasers is used with wavelength dependent surgical effects, e.g. the C02 laser emitting light at 10.6µm, a wavelength characterized by strong water absorption. However, at any wavelength, tissue removal will be accompanied by emission of shock waves, which can be detected using the methodology suggested in the current work. Concerning thermal damage, we are not aware of any work investigating whether thermal effects can be monitored using laser light beyond the near-infrared region. Nevertheless, compact and relatively inexpensive Nd-YAG lasers are generally available. Since those are operated in the nanosecond range at wavelengths of 532 nm or 1064 nm, they could potentially be used as a second laser dedicated for monitoring of thermal damage.
As a final remark, optoacoustic signals naturally depend on many factors, such as illumination wavelength and energy, sensitivity and bandwidth of the ultrasonic detector as well as other environmental factors, including tissue properties (e.g. blood content). Nevertheless, the proposed method is directed towards observing relative changes in signal characteristics that occur on a very short time scale (about 100ms in our experiments). Other factors are very unlikely to change within such a short time frame, thus the ablation-related changes can most probably be observed with any given system configuration in any type of tissue.

2.3.6 Conclusion

The current study demonstrated how the optoacoustic technique can be used for monitoring of collateral thermal damage during laser ablation. We were able to observe the associated rapid transitions of the surrounding tissue from the native to the coagulated and from the coagulated to the carbonized state. Furthermore, our method was able to reveal deterioration of cutting efficiency during the ablation process. In practice, our findings could potentially enable real-time monitoring of cutting efficiency and concurrent assessment of collateral thermal damage. This might prove particularly useful in surgical applications controlled from distance where ablation effects are difficult to observe and control. Future work is aimed toward attempting the technique on different tissue types and adapting it to overcome potential limitations in a realistic clinical setting. Furthermore, more quantitative results, such as the precise cutting depth or coagulation margin, can possibly be obtained by extending the approach to imaging in two or three dimensions.

2.4 Study 2: Monitoring of three-dimensional cutting profile

2.4.1 Motivation

Although surgical lasers have replaced mechanical scalpels and drills in various surgical applications of cutting hard and soft tissue, the lack of haptic feedback during laser-based surgery always leads to difficulties discerning the incision depth and incised tissue type resulting in a high risk of undesired, collateral tissue damage [47,55,56]. In practice, intermittent visual inspection or measurement of the incision profile is often required to guarantee a certain incision depth [11], leading to an increase in the complexity and duration of treatments. Alternatives to measuring the incision depth include numerical simulations coupled with preoperative planning [57, 58]. However, current models have only been validated against controlled experiments assuming specific tissue composition and laser settings, and therefore, cannot be applied to more complex clinical scenarios involving interpersonal differences in tissue properties or unexpected changes in treatment protocol. Real-time sensory feedback with the capability of three-dimensional tracking of incision depth and profile during laser surgery would greatly reduce the risk of undesired tissue damage and,as a consequence, improve the implementation of laser ablation treatments in medicine.

2.4.2 Overview of existing methods

Several prior attempts have been made to provide sensory feedback for monitoring incision depth. An optical method was recently proposed in an ex-vivo study of pulsed laser ablation of bone tissue [59]. Inline coherent imaging was used to generate a one-dimensional depth profile along the incident beam path yielding depth information with axial resolution of 6 µm over the course of the ablation procedure. The technique was shown to have the capability to sense tissue properties ahead of the ablation front enabling the surgeon to anticipate structures up to 176 µm below the incision. However, only relatively shallow incisions with a depth of less than 500 µm were generated and monitored in the experiments. Indeed, sensing backscattered light from depths on the order of several millimeters might represent a significant challenge. One-dimensional measurement

of ablation depth of laser-generated incisions has also been demonstrated in corneal tissue using femtosecond optical ranging [60]. This method measured the time required for a femtosecond pulse to make a round trip between the tissue surface and the bottom of the incision. However, this method was also only demonstrated on micro-incisions with depths between 180 to 3070 μm and has yet to be demonstrated to be capable of real-time measurements.

Shock waves have been shown to be present as a result of the explosive ejection of ablation products in a wide combination of laser-tissue processes [37, 45, 61, 62]. Since shock waves originate from the exact position of the ablation event, time-of-flight measurements can provide information about the location of tissue removal. A one-dimensional method using time-of-flight measurement of acoustic waves for real-time monitoring of incision depth in pulsed laser ablation of bone tissue was previously proposed based on measurement of the time delay between the laser-induced acoustic signal from the surface and the bottom of the ablation crater [63]. While the results showed general possibility of depth profiling measurements, the precision and accuracy of the method are yet to be demonstrated.

In the present work, we demonstrate a new method to measure the three-dimensional profile of deep incisions generated by pulsed laser ablation. The proposed method has real-time monitoring capability, and is based on multi-position time-of-flight measurements of shock waves that are generated from the ablation location. Capabilities of the newly introduced technique were showcased in ex-vivo studies. Sensitivity analysis of the reconstructed incision profile to the configuration of the multi-sensor detector array was further performed, examining both the detector location with respect to the incident laser beam and the number of acoustic sensors employed in the detection scheme. We demonstrate that robust and accurate tracking of the incision profile can be obtained utilizing a simple and inexpensive detection scheme, which has the potential to provide real-time position feedback for a variety of surgical applications.

2.4.3 Experimental design

A schematic drawing of the experimental setup can be seen in Fig.2.8. Laser ablation in a soft tissue sample was performed using a Q-switched Nd-YAG laser (Spectra Physics, Santa Clara, CA), operating at 1064nm with pulse duration of 8ns (full width at half maximum).

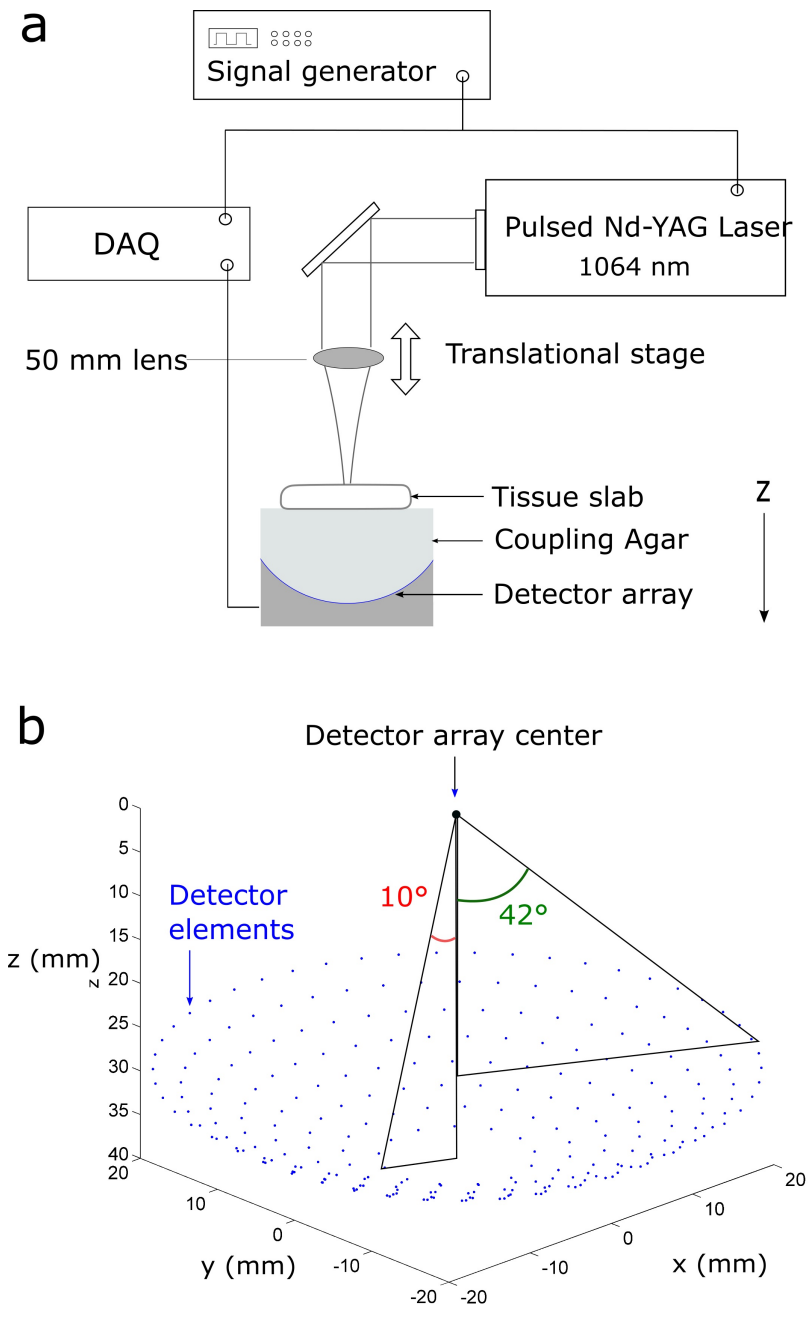

Figure 2.8: (a) Schematic of the experimental setup. (b) Plot showing the positions of each detector in the 256 detector array with detectors distributed on eight rings. Each detector is directed toward the center of the coordinate system. Each ring results in a different observation angle with respect to the central axis of the detector array. The observation angle from a detector of the innermost ring is 10° whereas from a detector of the outermost ring the observation angle is 42° as indicated in the figure. (Figure published in [64], Copyright 2015, WILEY-VCH Verlag GmbH Co. KGaA, Weinheim)

Given the high pulse energy of 150mJ emitted at a relatively low repetition rate of 5Hz, the laser beam was able to effectively generate deep incisions while causing a relatively low degree of thermal damage. Additionally, a 50 mm lens mounted on a manual translational stage (Thorlabs, Newton, NJ) was used to focus the beam into the tissue sample, which resulted in the capability to create a 9 mm deep incision.
Shock waves emitted from the origin of an ablation event were detected at multiple positions using an array of ultrasonic detectors with a central frequency of 4 MHz (Imasonic SAS, Voray sur l'Ognon, France) [65, 66]. The ultrasonic array consists of 256 piezocomposite detectors distributed on a spherical surface with 40 mm radius and covering a total angle of 90° (Fig.2.8(b)). Fresh bovine muscle tissue from the slaughterhouse was used in the experiments, for which no ethical approval was necessary. Tissue samples were carefully removed of fat and connective tissue, resulting in homogeneous muscle samples, and placed on a homogeneous body of agar in order to maintain effective acoustic coupling. Acoustic gel was used to guarantee ultrasonic transmission at the tissue-agar interface. The beam spot on the tissue surface, which represents the upper end of the incision profile to be created, was focused near the center of the spherical surface formed by the detector array, where the highest sensitivity and reconstruction accuracy is expected. Laser pulse generation and acoustic data acquisition were both triggered externally by a signal generator (Agilent Technologies, CA) using a sequence of TTL pulses at 5Hz. Time-resolved signals were recorded by a custom designed multi-channel data acquisition system (Falkenstein Mikrosysteme GmbH, Taufkirchen, Germany) with a sampling rate of 40 MS/s and 12-bit vertical resolution.

2.4.4 Reconstruction Method

In order to reconstruct the incision profile based on the detected shockwaves a novel reconstruction algorithm was developed. The position of the ablation event of each laser pulse was obtained by solving a non-linear system of equations describing the time-of-flight of the shock wave towards the detector array. The propagation time t_i of the shock wave until the i^{th} array detector is given by

$$t_i = \frac{1}{c} d_i = \frac{1}{c} \sqrt{(x - x_i)^2 + (y - y_i)^2 + (z - z_i)^2} \tag{2.1}$$

where d_i denotes the distance between the unknown position of the shock wave origin, located at coordinates (x,y,z), and the i^{th} detector, located at coordinates (x_i,y_i,z_i), and c denotes the average speed of the shock wave during its propagation to the detector, which is also considered unknown and is further assumed to be constant. The coordinate positions of the origin of the shock wave and the i^{th} detector are shown in Fig.2.9(a). The propagation time t_i can be expressed as a nonlinear function of (x_i,y_i,z_i) , (x,y,z) and c.

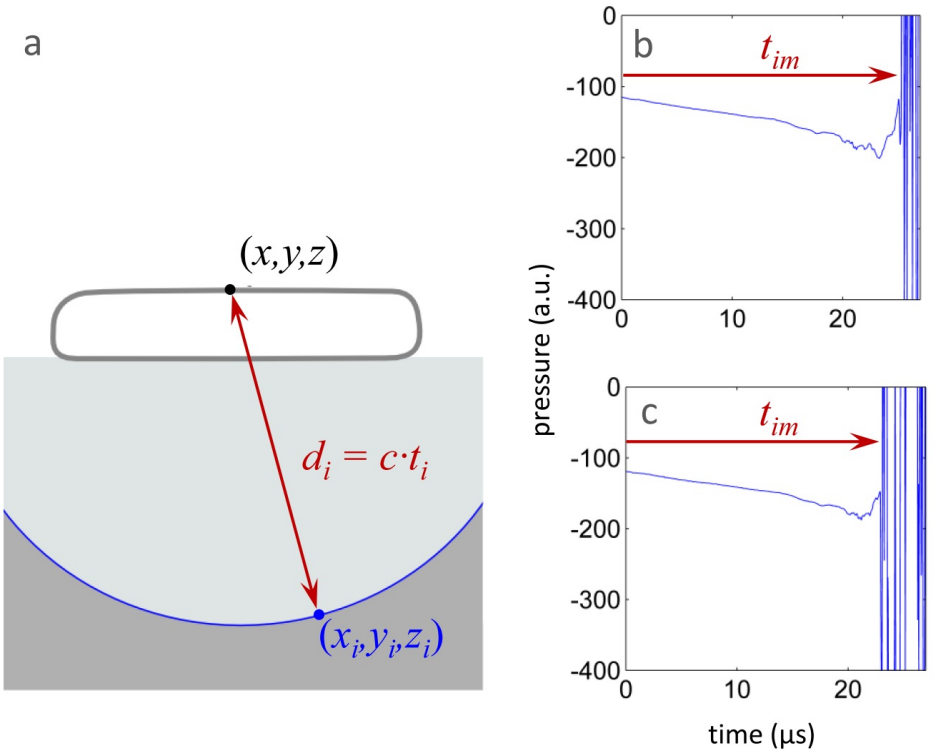

Figure 2.9: (a) Schematic illustrating the geometry of the inversion problem. The coordinate positions of the origin of the shock wave (x,y,z) and the i_{th} detector (x_i,y_i,z_i) are showcased. (b) Acquired signal for a single detector with an observation angle of 42° for a laser pulse 3.4 seconds after the start of the experiment. (c) Equivalent signal for a laser pulse 8.0 seconds after the start of the experiment. Time t_{im} indicates the measured time interval between the onset of the laser pulse and the arrival of the shock wave. (Figure published in [64], Copyright 2015, WILEY-VCH Verlag GmbH Co. KGaA, Weinheim)

The measured value of the time-of-flight for the i^{th} detector t_{im} can be then obtained from the time-resolved signal of the respective channel by taking the time elapsing between the onset of the laser pulse and the arrival of the shock wave at the detector.

The determination of the four unknown variables x, y, z, and c for each laser ablation pulse is based on a least-square minimization of the difference between the theoretical and measured time-of-flight for all the detectors of the array, i.e.

$$(x_{sol}, y_{sol}, z_{sol}, c_{sol}) = \underset{x,y,z,c}{\operatorname{argmin}} \|t_{im} - t_i\| \tag{2.2}$$

The reconstructed incision profile over the entire experiment can be visualized by plotting the solutions for the unknown positions (x, y, z) obtained for the entire pulse train.

2.4.5 Results

2.4.5.1 Shock wave detection

Two typical examples of shock waves recorded by the transducers are shown in Fig.2.9(b) and Fig.2.9(c). Representative measurements from a single detector with an observation angle of 34° at two different time instants after the start of the ablation experiment are shown. For laser pulses occurring at later instants in the experiment, the measured time interval t_{im} between the onset of the laser pulse and the arrival of the shock wave at the detector is getting shorter. This can be perceived in the examples shown with t_{im} = 25.5µs after 3.4s (Fig.2.9(b)), and t_{im} = 23µs after 8.0s (Fig.2.9(c)). Indeed, the origin of the shock wave, most certainly located at the bottom of the incision, moves closer to the detector as the ablation experiment progresses.

2.4.5.2 Time-resolved reconstruction of the incision

Fig.2.10(a) presents the x-, y-, and z-coordinates of the ablation location as the ablation process proceeds with time, determined by using data from all 256 detectors for the reconstruction. While the shock wave formed initially propagates at supersonic velocities in the vicinity of its origin, its speed is expected to quickly attenuate to the normal speed of sound in soft tissues, as was earlier observed in corneal tissue and water [62]. Given the speed of sound of 1580m/s for muscle tissue and 1540m/s for agar, a value of around 1550m/s is expected for the average speed of sound (the shockwave needs to travel through a volume comprising about 75% agar and 25% muscle tissue).

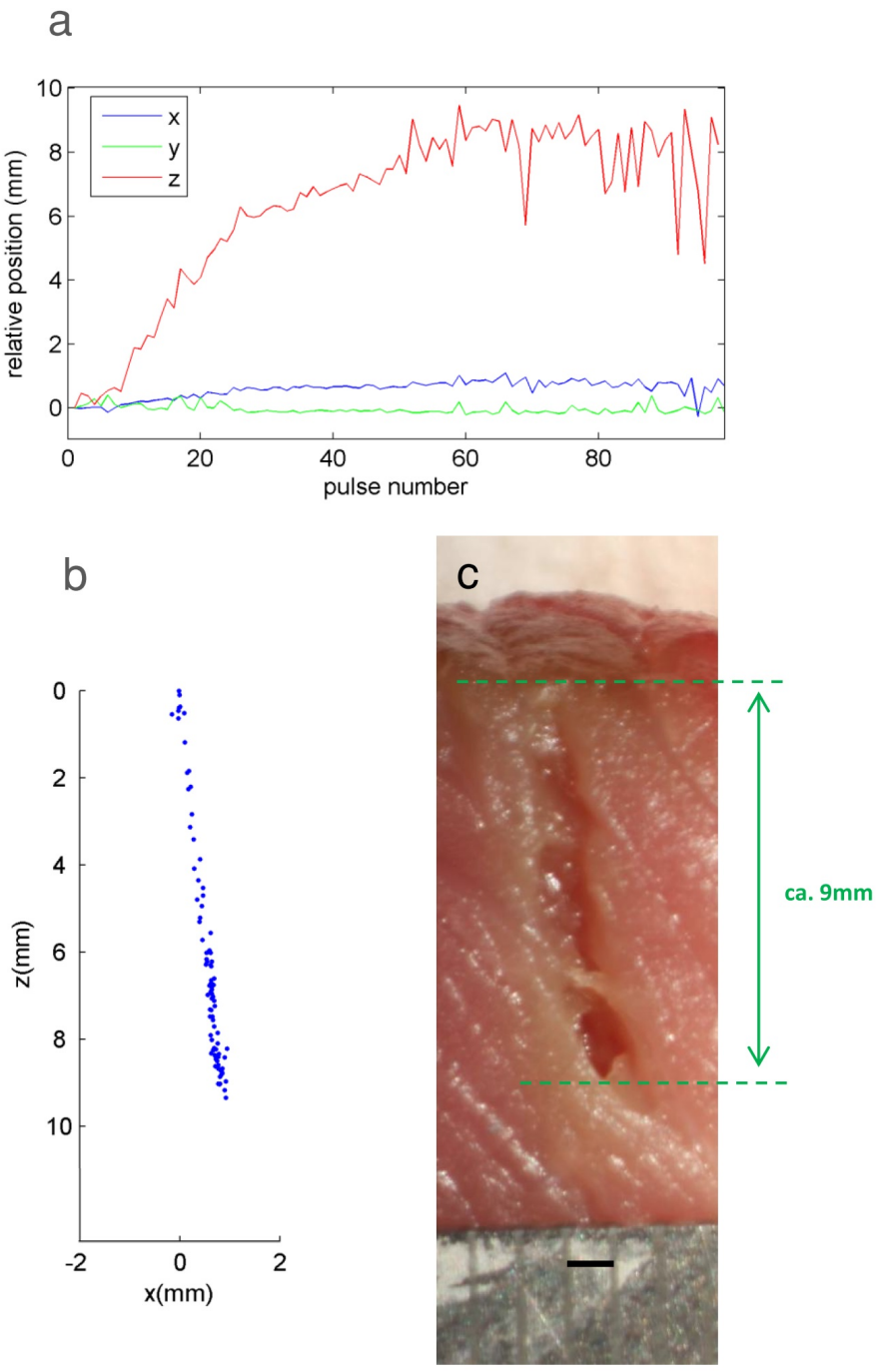

Figure 2.10: (a) Position of the bottom of the incision, assumed to be at the origin of the shock wave, as the ablation progresses in time. The x, y and z coordinates are relative to the reconstructed value for the initial laser pulse. (b) Reconstructed 3D incision profile in the x-z plane, where each dot represents a reconstructed relative position of bottom of incision for a single laser pulse. (c) Cross-section photograph of incision obtained from sliced tissue after completion of the experiment (ruler increment 1mm). (Figure published in [64], Copyright 2015, WILEY-VCH Verlag GmbH Co. KGaA, Weinheim)

Indeed, in our reconstructions the average speed of shock wave propagation was found to be within 2% of 1540 m/s. The x- and y-coordinate of the incision location range from 0.0 to 1.0mm and from 0.0 to 0.3mm, respectively, indicating that the path of the laser beam was not aligned precisely with the central axis of the detector array. The z-coordinate of the incision profile gradually increases from zero to 9.4 mm as the ablation process progresses. The depth of the ablation process ceases to increase after a depth of 9.4 mm, likely as a result of reduction in fluence below the ablation threshold due to divergence of the focused laser beam.
After about 50 laser pulses, in addition to the drastic reduction in the cutting efficiency, the amplitude of fluctuations in the z-coordinate of the origin of the ablation events in Fig.2.10(a) increases. This might be due to the fact that, as the incision gets deeper, shock waves are generated not only at the bottom of the incision, possibly due to ablation of previously generated tissue debris within the crater. Further investigations are necessary to determine the definitive cause behind oscillations in the z-coordinate as ablation efficiency is decreasing.
A projection of the reconstructed ablation positions along the x-z plane is displayed in Fig.2.10(b) while a corresponding cross-sectional photograph of the incision, obtained from sliced tissue after completion of the experiment, is shown in Fig.2.10(c). The reconstructed points in Fig.2.10(b), obtained from all 256 measured signals, show an incision profile that is slightly off parallel to the z-axis similar to the incision profile in the photograph in Fig.2.10(c), illustrating that the current technique can also measure incision geometry in the lateral directions. As can be established from Fig.2.10(b), the deepest point of the reconstructed profile is located at a depth of 9.4mm, which is in good agreement with the deepest part of the incision obtained from the photograph (Fig.2.10(c)).

2.4.5.3 Effect of sensor array geometry on incision reconstruction

To investigate how sensor array geometry can influence the reconstructed incision profile several reconstructions were performed, each using a subarray of the 256 detectors. Fig.2.11 shows 4 examples of different subarrays, each representing detectors distributed along a single ring of the 256 detector array such that all detectors within the subarray have the same observation angle. For each reconstruction at a specific observation angle, data from all the detectors in this ring were used. The corresponding reconstructions are shown in Fig.2.12. The incision profiles in the x-z plane clearly illustrate that the pre-

cision of the incision profile is the worst for the narrowest observation angle studied of 10°, while it improves with increasing observation angle, approaching the precision of the solution determined using data from all 256 detectors.

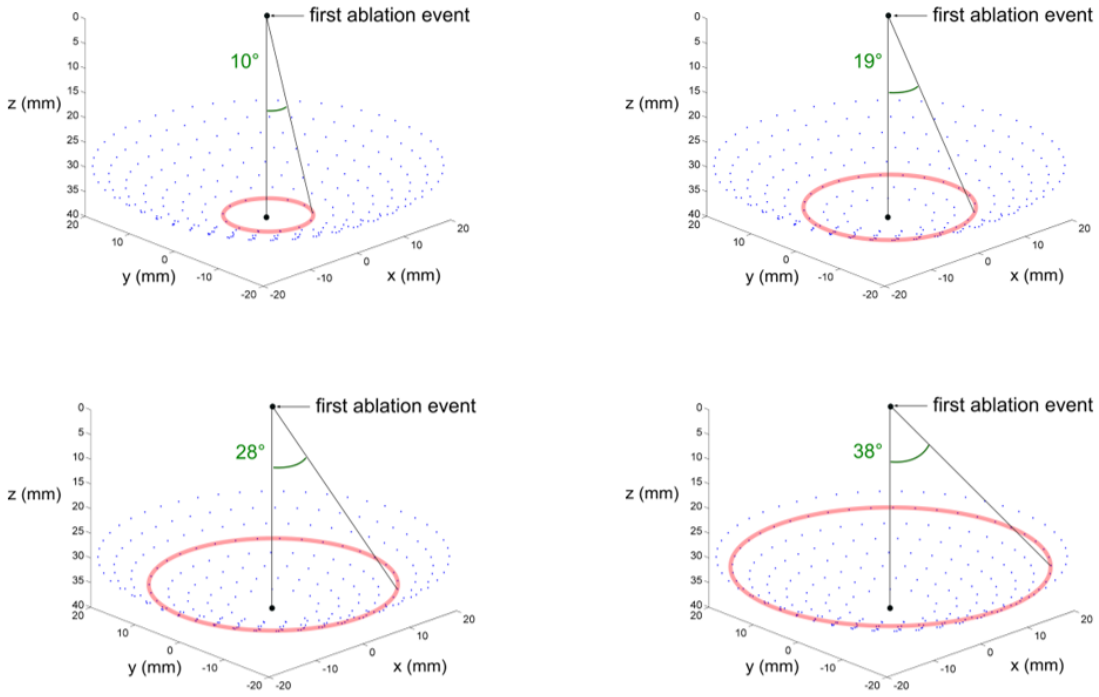

Figure 2.11: Ring-shaped subarrays of the 256 detector array and corresponding observation angles of 10°, 19°, 28° and 38°

2.4.6 Sensitivity Analysis

Reconstruction of the incision position based on data from all 256 detectors is an overdetermined inverse problem as only four unknowns (x, y, z, c) need to be calculated. Thereby, measurement of the shock wave at four different positions is in principle sufficient to reconstruct the location of the ablation event. While additional information may result in a better reconstruction and minimize the effect of errors in the measured propagation times, it could also be unnecessary and redundant and only result in excessive costs in terms of number of sensors and computational time.

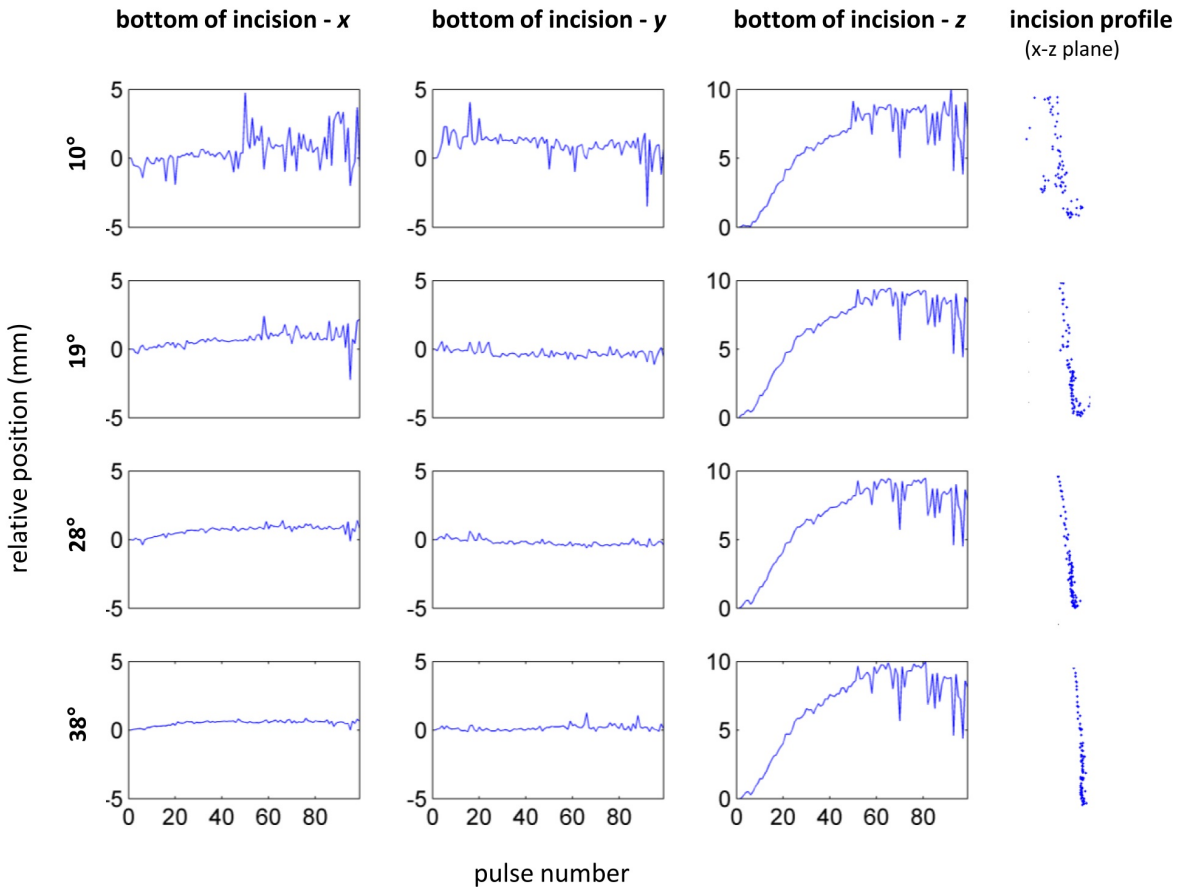

Figure 2.12: Coordinates indicating relative position of the bottom of the incision as determined using all the detectors from a single detector ring. The x-z plane of the incision profile for each reconstruction is also shown, indicating better reconstruction of the ablation position for larger observation angles. Reconstructions using observation angles of 10°, 19°, 28° and 38° are shown. (Figure published in [64], Copyright 2015, WILEY-VCH Verlag GmbH Co. KGaA, Weinheim)

To examine sensitivity of the reconstructed incision profile to the geometry and number of detectors used in the reconstruction, an average residual from a best-fit curve to the resulting coordinates x, y and z was defined. For this, a sixth order polynomial function was fit to each of the x, y, and z coordinates of the reconstructed profile as a function of the laser pulse number n. For example, the average residual in the x direction is defined as

$$R_x = \frac{\sum_{n=1}^{N} |P_x^6(n) - x(n)|}{N} \tag{2.3}$$

where $P_x^6(n)$ is the polynomial fit, N is the total number of laser pulses and $x(n)$ is the reconstructed x coordinate of the origin of the shock wave as a function of the laser pulse number. Analogous expressions are used to define the average residual in the y- and z-directions.

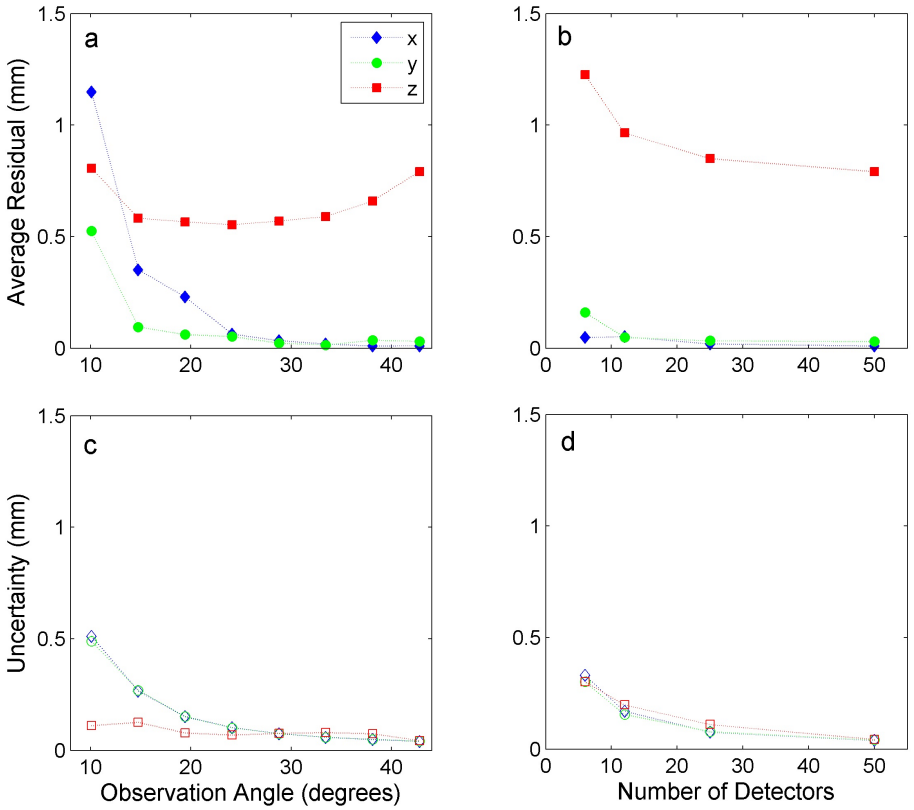

Figure 2.13: Experimental reconstruction quality described by the average residual over all ablation pulses as a function of the observation angle (a) and number of detectors used in the outer sensor ring for 42° observation angle (b). Uncertainty in the result of the reconstruction algorithm (caused by an uncertainty in the time of arrival of the shock waves) as a function of the observation angle (c) and the number of detectors used in the outer sensor ring for 42° observation angle (d). (Figure published in [64], Copyright 2015, WILEY-VCH Verlag GmbH Co. KGaA, Weinheim)

This average residual represents the level of noise in the reconstruction, i.e., how precisely the reconstruction method generates a smooth profile. While the incision profile is not expected to precisely follow a smooth polynomial fit, the average residual can be thought to have two components, an intrinsic component that describes the actual deviation of the real incision profile from a smooth fit due to physical phenomena, and an extrinsic component that represents errors caused by numerical inaccuracies or signal processing artifacts. The change in the extrinsic part of the average residual can be therefore used to assess the sensitivity of the reconstructed incision profile to changes in the geometry and number of detectors used for the reconstruction.

In this study, the precision of the reconstructed incision profile is examined through the average residual as a function of the observation angle of the detectors and the number of detectors used for the reconstruction. From Fig.2.13(a), it is clear that along the lateral directions (x- and y-) data from higher observation angle detectors contributes preferentially to more precise determination of the incision profile. The average residual approaches zero as the detection angle increases, suggesting that the extrinsic residual component becomes negligibly small while the incision profile in both lateral directions becomes very smooth.

In the axial z-direction, the average residual from the polynomial fit ranges from 0.55 to 0.80mm, and does not follow a decreasing trend with observation angle as for the lateral directions. This suggests that deviation from a smooth polynomial fit in the axial direction cannot be eliminated by changing the observation angle of the detectors used to collect data, and that this deviation of between 0.55 to 0.80mm is an intrinsic part of the average residual and is mostly influenced by fluctuations of the ablation location as the ablation rate slows down and the incision depth eventually ceases to increase, as discussed in Section 2.4.5.2.

Figs.2.12 and 2.13(a) illustrate that using data from the detectors positioned with higher observation angles yields a more precise reconstruction of the incision position. As shown in Fig.2.8 the number of detectors in each ring increases with observation angle, therefore an increase in the number of detectors might equally explain the trend observed in the measurements. Fig.2.13(b) plots the average residual for the reconstructions from different number of equally spaced detectors in the outer ring (observation angle of 42°). As can be clearly observed, the average residual gradually decreases in all three dimensions as data from a greater number of detectors are used for reconstruction. The fact that the average residual becomes negligibly small in the lateral directions (x- and y-) while it seems to gradually decrease to a steady value around 0.7mm in the axial z-direction, sug-

gests that, by increasing the number of detectors, the extrinsic component of the average residual can be effectively reduced in all dimensions until only an intrinsic component remains in the z-dimension. Using as few as 12 detectors is already sufficient to reduce the extrinsic component to about 0.2mm in the axial and less than 0.1mm in the lateral dimensions. Comparison with Fig.2.13(a) shows that dependency of the extrinsic component of the average residual on the number of elements is not significant enough to fully justify the strong trend observed for the x and y dimensions in Fig.2.13(a), suggesting that the average residual is in fact strongly influenced by the observation angle. Therefore, it can be concluded that a reduction in average residual can be achieved by increasing only the observation angle and keeping the number of detectors constant.
To further validate the experimental findings in Figs.2.13(a) and 2.13(b), a numerical analysis was performed. The sensitivity of the reconstructed incision position to errors in the measured t_{im} can be quantified for different detector configurations using inversion of the system of equations in Eq.(2.1) and subsequent numerical analysis which propagates a small uncertainty ε into t_{im} and then examines the resulting uncertainty in the reconstructed position. The resulting uncertainty in the reconstructed location of the origin of the shock wave, for any given pulse, is defined for the x-dimension as

$$U_x = \max_{i\in[1,N]} |x(\overrightarrow{t_m}) - x(\overrightarrow{t_m} + \varepsilon \cdot \overrightarrow{e_i})| \tag{2.4}$$

where $\overrightarrow{t_m}$ is the array of all the t_{im} values, ε is an uncertainty in the measured time, $\overrightarrow{e_i}$ is the i^{th} unit vector and N is the total number of detectors used in the configuration. Analogous expressions are used to define the uncertainty in the y- and z-directions.
Calculations were performed for the laser pulse number corresponding with the deepest point of the incision profile, and with an uncertainty of ε = 0.5µs in the measured time, and the results are shown in Figs.2.13(c) and 2.13(d). The reconstructions of the x- and y- positions of the incision become increasingly sensitive to errors in the measured time-of-flight with decreasing observation angle, while the sensitivity of the z-position does not significantly depend on the observation angle. This supports the trend of the average residual with changes in observation angle, as was shown in Fig.2.13(a). The sensitivity of the reconstruction to uncertainties in time increases with fewer detectors, proving the point that fewer detectors lead to a less robust reconstruction. The experimental data shows this as well since the average residual in Fig.2.13(b) increases when the number of the detectors used is reduced.

2.4.7 Discussion

The current results demonstrate that highly precise and accurate measurements of the position of an ablation event during laser cutting can be determined through detection of the generated shock waves by multiple acoustic sensors. It was shown that as few as 12 detectors, positioned in the appropriate geometry, could form a system capable of accurately measuring the position of ablation, in both the plane perpendicular to the laser beam and the axial direction, yielding lesion mapping in good agreement with histological evaluations. A computational time of 1.8ms was required to reconstruct each ablation position using data from 12 channels and a standard consumer level processor (Intel Core i5 at 3.3GHz). This renders this method capable of inexpensive real-time monitoring of surgical applications with laser repetition rates up to 500Hz. Using optimized algorithms and more advanced processors or GPU-based algorithmic implementations, repetition rates in the tens of kHz range are likely to be achieved.
Several simplifications were allowed for this proof-of-concept study. For convenience of this proof-of-concept study, we have utilized an existing detector array whose number of detectors and geometry were obviously not optimized for any specific surgical application. Yet, the sensitivity analysis provided in the current work was able to address the question of the relationships between detection geometry and reconstruction accuracy and precision. As a rule of thumb, it has been determined that the proposed method is capable of accurately detecting the ablation position as long as at least 12 detectors are utilized and placed with a sufficient observation angle of at least 24° with respect to the ablating beam. This finding can serve as a basis for future design of an optimized detector array for monitoring typical incision profiles generated in specific surgical applications. Furthermore, in the current study the detector array was placed on the opposite side of the tissue from the ablating laser beam. Clearly, in a clinical application of a method of this type for surgical feedback, the ablated tissue volume might only be accessible from one side. Therefore, the detectors would have to be placed on the same side as the ablating laser. In principle, the proposed method should be capable of providing comparable results also for different orientations of the detection array as long as the observation angles with respect to the incident beam are sufficient. It should be noted, however, that in case the detectors are located on the same side of the incident ablating laser, the air-tissue boundaries at the incision crater may result in shock wave reflections that may eventually reach the acoustic detectors. These reflections would however arrive at the detector positions at later time points (as compared to the initial shock wave) thus can be filtered out.

In the current study acoustic coupling was achieved by placing a homogeneous body of agar covered with a thin layer of ultrasonic gel between tissue and the detector array. In practice, coupling would need to be achieved by other means. Considering that the detector array might likely be placed on the same side as the ablating beam, coupling could be ensured by placing the detector in contact to the tissue surface. If a contact-based approach is not feasible, the shock waves will need to be detected through air. Due to high intensity of the shock waves, as seen in the saturation of the current measurements, it can be hypothesized that acoustic coupling through air could be made to work for the proposed method. Shock waves have already been successfully detected in air during pulsed laser ablation using piezoelectric transducers [67] or probe beam deflection [68, 69], supporting this hypothesis. Moreover, special air-coupled piezoelectric transducers have been developed to further enhance sensitivity for ultrasound detection in air [70–72]. Whether similar precision and accuracy can be maintained when detection is performed through air needs to be further investigated.

Despite the fact that only homogeneous muscle tissue was used in the current study, the shock waves formed due to ablation are result of a rapid increase in pressure due to absorption of laser light energy. Shock wave generation would obviously occur in all tissue types as long as the incident laser energy exceeds the corresponding ablation thresholds. Because the proposed method depends only on the time-of-flight information, similar incision monitoring capabilities are expected for laser ablation processes in inhomogeneous tissue samples, provided that the differences in the rate of shock wave velocity attenuation and the speed of sound between the different tissue types are negligible, as is the case between different types of soft tissues, although further experiments are needed to confirm this. In principle, the suggested technique should also work in hard tissues. However, while ablation in hard tissue will also lead to micro-explosions [57], similar to those generating shock waves in soft tissue ablation, acoustic attenuation, especially of the high frequencies components, is considerably higher. This may in turn lead to higher uncertainties in the measured time-of-flight information in case no steep changes in the detected acoustic signals can be recognized.

In highly heterogeneous tissues with significant changes in the speed of sound, e.g. cases of more complex geometries comprising of soft and hard tissues, the average propagation speed of the shock wave to different detectors will likely differ so that the current reconstruction method cannot be applied directly. Incision profiling in those cases might be achieved by expanding the current reconstruction method to include more unknowns for additional speed of sound values and making certain assumptions on the relative ge-

ometry of the different tissue types. In case laser cutting is performed in heterogeneous tissue samples with varying speed of sound, it has also been shown that the amplitude of the generated acoustic waves changes when ablation passes through an interface between tissue types with considerable differences in optical and mechanical properties, such as necrotic and vital tissue [45]. Therefore, it may also be possible to use the amplitude of the measured shock wave to detect interfaces where transition between tissues occurs, and use this information to appropriately account for the changes in the speed of sound. It should also be noted that in heterogeneous tissue, interfaces between different tissue types may lead to shock wave reflections. However, any measured reflections will arrive at the detectors at a later time than the initial shock wave and thus can be separated.
Compared to the other methods reported in the literature for sensing ablation depth [45, 59, 60], the current method can be used to track the incision profile in all three dimensions instead of only in the axial direction. The additional information might be useful in facilitating the development of a more robust and reliable feedback system capable of performing accurate measurements of the incision profile and depth even if challenged by surgeon tremor or patient movement. Furthermore, laser-generated incisions of several millimetres are common in various applications in bone surgery and can even reach depths of up to 15mm [11]. The current method establishes capacity to measure accurate incision profiles of at least 9mm in depth, which has yet to be demonstrated by other methods.

2.4.8 Conclusion

The work presented in this paper demonstrates that the depth, as well as the entire three-dimensional profile of an incision generated by pulsed-laser ablation cutting, can be measured using acoustic sensing from a multi-position detector array. An incision of approximately 9mm in depth in bovine muscle tissue was generated with a pulsed laser, while the proposed technique was able to capture the incision profile with high positional accuracy and good agreement with histological measurements. The presented reconstruction sensitivity analysis has demonstrated that the proposed technique can be effectively accomplished with relatively small number of detectors placed in appropriate positions. The sensitivity analysis has also provided a solid basis for design of optimized detection schemes, which is the subject of ongoing investigations. Since the presented technique is capable of making real-time measurements of the ablation location in three-dimensions, it holds great promise for being developed into an affordable real-time sensor to provide

incision depth feedback in a number of commonly applied pulsed-laser ablation surgical procedures.

2.5 An optoacoustic method for discerning critical tissues

2.5.1 Motivation

The study shown in section 2.4 showcased how an optoacoustic monitoring method can provide precise feedback on the ablation process by tracking the three-dimensional incision profile. Reliable information about the incision depth might significantly increase safety when incisions are performed close to critical structures. However, in order to avoid ablating critical tissues, prior knowledge about the distance of critical structures from the upper edge of the incision is necessary. Therefore, it would be highly beneficial if the proposed three-dimensional incision profiling method could be combined with a forward-looking sensing technique in order to detect critical structures, such as nerves, underneath the incision. A particular and very promising application might be distinguishing nerve and fat tissues.
It has been shown that different tissue types such as nerve, fat and bone tissue could be distinguished based on their characteristic optical properties using a method called diffuse reflectance spectroscopy that measures the intensity of light that has been back-scattered from the illuminated tissue [18, 47]. The findings suggest, for instance, that nerve and fat tissues have different scattering properties. Since optoacoustic signals are influenced by absorption as well as scattering properties of the illuminated tissues, it is worth evaluating whether optoacoustics might be used for tissue differentiation, in particular in the case of nerve and fat tissues.

2.5.2 Method and experimental setup

When a homogeneous tissue sample is illuminated by a broad laser beam, the optoacoustic signal originating from the tissue volume can be approximated as an exponentially decaying function

$$S(z) = C\, e^{-\mu_{eff} z} \tag{2.5}$$

where z denotes the distance from the tissue surface, C is a constant number determined by biophysical properties of the illuminated tissue and the fluence on the tissue surface and μ_{eff} denotes the effective absorption coefficient $\mu_{eff} = \sqrt{3\mu_a(\mu_a + \mu_{s'})}$, with μ_a and $\mu_{s'}$ denoting the absorption and reduced scattering coefficients.
The experimental setup that was used to investigate whether nerve and fat tissues can be distinguished using Optoacoustics is shown in Fig.2.14. The collimated, unfocused beam of a Q-switched Nd-YAG laser (Spectra Physics,Santa Clara, CA), operating at 355nm with pulse duration of 8ns (full width at half maximum), was used to illuminate the tissue samples. Nerve and fat tissue samples were extracted from a fresh porcine neck, which was obtained from a local slaughterhouse, and cut into small pieces of a minimum thickness of 3mm. Using a single mirror and no additional optics, the laser beam was guided onto the tissue surface and the optoacoustic signal originating from the illuminated tissue was collected by the same optoacoustic detector array as in the previous study (see section 2.4.3).

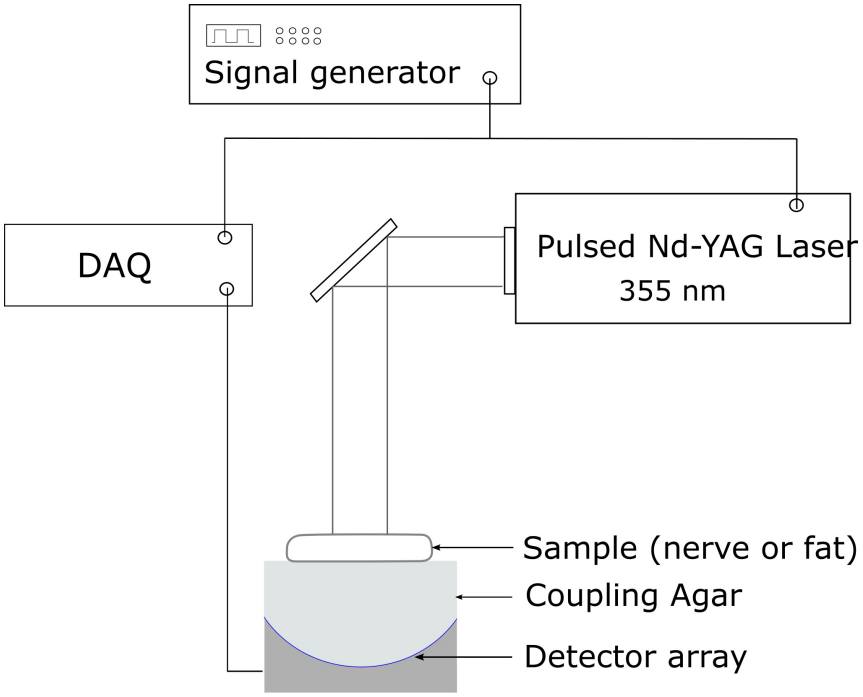

Figure 2.14: Schematics of the experimental setup for distinguishing nerve and fat tissues

2.5.3 Preliminary results and discussion

The optoacoustic signal detected from the surface of a fat tissue sample is shown in Fig.2.15(a), while the corresponding natural logarithm of the signal is depicted in Fig.2.15(b). As can be clearly obtained from Figs.2.15(a-b), the signal amplitude shows an exponential decay with an increasing distance from the tissue surface. From the slope of the decaying signal in Fig.2.15(b) an effective attenuation coefficient of 0.8mm^{-1} can be obtained. Experiments with a total of 4 fat tissue slices, including the slice shown in Fig.2.15, resulted in effective attenuation coefficients in the range of 0.7-1.0mm^{-1}, with a mean value of 0.8mm^{-1}. Experiments performed with the same laser settings but 4 different nerve tissue slices resulted in an effective attenuation coefficient within the range of 0.5-2.5mm^{-1}, with a mean value of 1.6mm^{-1}.

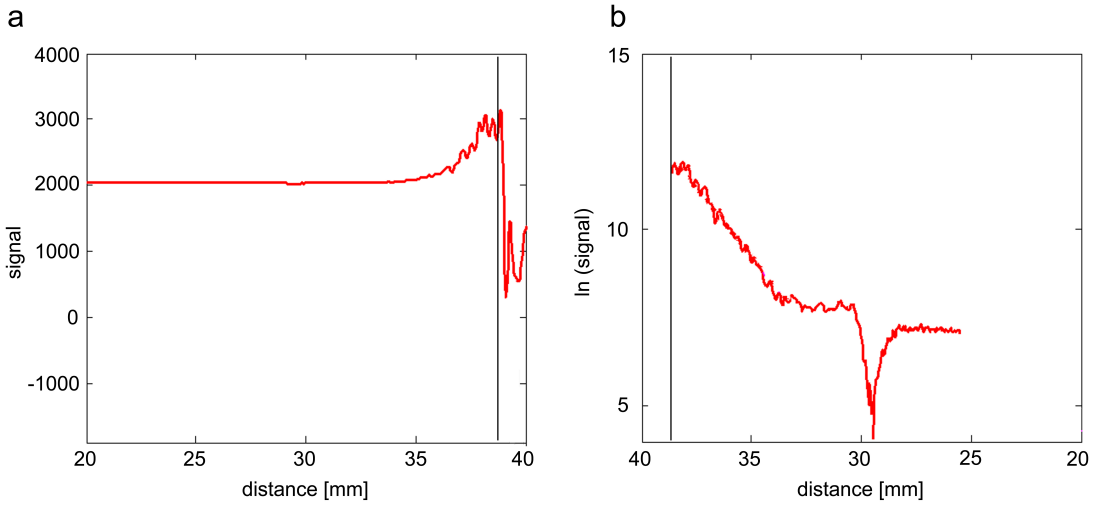

Figure 2.15: (a) Optoacoustic signal detected from the surface of a fat tissue sample. Here only a single one-dimensional signal from one of the innermost detectors of the detector array is shown (b) logarithm of the detected signal showing a linear slope at the tissue surface corresponding to an effective attenuation coefficient of 0.8mm^{-1} (a-b) dark vertical line represents tissue surface, x-axis represents distance from transducer.

Nerve tissue samples were taken from the porcine neck and therefore consisted of myelinated nerve fibers, which are characterized by a fatty sheath around the axon. As a consequence, the absorption coefficient of nerve tissue is closely related to the absorption coefficient of fat tissue. The significant difference in the effective attenuation coefficients measured in our experiments is therefore likely due to a significantly higher optical scattering

of nerve tissue. This would also be supported by the findings of previous studies [18, 47] which detected higher optical scattering in nerves compared to fat tissue samples.
The advantage of our proposed method for distinguishing different tissue samples, such as nerve and fat tissues, is that it could be combined with the same optoacoustic monitoring technique that we have previously shown to be capable of detecting the three-dimensional cutting profile in real-time (see section 2.4). As a disadvantage, however, it has to be noted that the slope of the optoacoustic signal might also be affected by the geometry of the ultrasonic detector as well as its bandwidth. Therefore, for future work, we recommend using high-bandwidth detectors with small active detector surfaces, such as needle hydrophones. Future work also needs to investigate whether thin structures of a thickness of less than 1mm can also be realibly detected using the proposed method.

2.6 Summary and outlook

Several optoacoustic monitoring techniques were proposed to overcome mayor disadvantages of laser surgeries, namely the risk of collateral thermal damage and the lack of haptic feedback, which in turn results in a high risk of undesired damage to adjacent, critical tissues such as blood vessels or nerves. The first study (section 2.3) showcased how a simple, cost-effective system utilizing a single ultrasonic transducer can already detect the onset of severe thermal damage and concurrently monitor cutting efficiency. The second study (section 2.4) proved that, using a more elaborate detector array, it is possible to reconstruct the entire three-dimensional cutting profile in real-time and thereby provide a very valuable, precise feedback on the outcome of the incision process. In a final, preliminary study (section 2.5) it was shown how a single detector of the detector array could be used to estimate the type of tissue underneath the irradiated tissue surface. The previously proposed three-dimensional monitoring technique might therefore be combined with a forward-sensing technique for tissue type differentiation. Such an integrated monitoring system could solve all problems arising from the lack of haptic feedback during laser surgeries by providing a precise measurement of the depth of the cut as well as identifying the type of tissue underneath the cut.

3 Optoacoustic Monitoring of Radio-frequency Catheter Ablation

3.1 Clinical Background: Treatment of cardiac arrhythmia

Cardiac arrhythmia is a very common disease characterized by irregular or very high heart beat frequency. Atrial fibrillation (AF), the most common type of cardiac arrhythmia with more than a projected 2 million cases [73], is associated with increased morbidity and mortality. Cardiac arrhythmias are due to the occurrence of faulty electrical pathways within the myocardium that lead to erroneous activity of the cardiac muscle. Due to its advantages over long-lasting medicative treatments of cardiac arrhythmias, radio-frequency ablation (RFA) has been widely applied in clinical practice with a 15000 annually performed procedures in the United States [74].

3.2 Need for real-time monitoring

Despite its wide use in clinical practice, RFA is a procedure that is technically challenging and highly operator dependent, leading to significant variances of success in different treatment facilities, and a non-negligible rate of procedures needing follow-up treatment to successfully eliminate AF re-occurrence [75]. While continuously improving technologies have led to corresponding growth of success rates in recent history, post-RFA arrhythmia still occurs in up to 25% of patients [75]. Thus, a large room exists to increase the success rate of RFA treatment of AF and other cardiac arrhythmias.
Recent technological advances in cardiac RFA treatment have provided novel methods for

accurate guidance and placement of the ablation catheter [76–78] and have shown to improve treatment safety and increase success rates. Despite these significant improvements in catheter navigation, lesion geometry and size remain unobservable during the ablation process, and are currently estimated by the surgeon based on minimal indirect feedback such as ablation power and contact monitoring, a judgement highly sensitive to previous experience and training. The overestimation of lesion size by the operator can result in the need for re-treatment, and conversely, underestimated lesion size can cause undesired tissue damage. In a recent 2010 study [79], major complications including cardiac tamponade, transient ischemic attacks, stroke, and even death were reported in 4.5% of catheter ablation procedures for atrial fibrillation. As opposed to indirect feedback of the ablation process, direct feedback based on real-time sensory information can provide indisputable information on lesion characteristics and thus can significantly improve treatment efficacy and safety.

3.3 Overview of existing methods

Real-time monitoring of RFA lesion formation has been previously attempted with several different imaging modalities. Advances in magnetic resonance imaging (MRI) technology have led to MRI-based techniques for real-time visualization of RFA lesion formation in porcine hearts [80]. However, temporal and spatial resolution of MRI are limited, and the high costs of operation and specialized equipment prohibit MRI-based techniques from becoming commonplace in regular clinical treatments of RFA. A radio-frequency catheter with integrated ultrasound sensing capabilities has been proposed to detect RFA lesion depth progression in real time [81], which rendered unsatisfactory results due to poor imaging contrast and inability to clearly distinct the boundary between necrotic and unablated tissue. Novel ultrasound-based methods such as acoustic radiation force impulse (ARFI) imaging [82, 83] and thermal strain imaging [84, 85] attempt to improve the contrast between the necrotic and unablated tissue during RFA lesion formation by monitoring changes in tissue elasticity and temperature-dependent speed of sound variations, respectively. The ARFI technique in its current state is highly sensitive to motion artefacts and has poor temporal resolution, while thermal strain imaging is only capable of providing indirect information on lesion size by inference from measurement of an apparent temperature rise during RFA. Contrast between necrotic and unablated tissue can also

be observed with optical imaging techniques. Optical coherence tomography [86, 87] was shown to be capable of real-time monitoring of RFA lesion formation with high spatial resolution, however, penetration depth of this technique is limited to 1mm, which can only allow for monitoring of tissue effects in the vicinity of the electrode tip and for superficial imaging of the lesions, which typically extend to a depth of up to 6mm.
Optoacoustic imaging, as a hybrid technique of optical and ultrasound imaging, has the potential to overcome both the contrast limitation of pure ultrasound detection and the depth penetration limitation of pure optical imaging. Necrotic and unablated tissue have been shown to have distinct optoacoustic spectra [16], yet implementation of optoacoustics for real-time monitoring of lesion formation during RFA has not been reported.

3.4 Development of an optoacoustic catheter

3.4.1 Motivation

One objective of this work was to design, assemble and test an optoacoustic catheter prototype for monitoring RFA procedures. Due to the high sensitivity of optoacoustics to thermal effects, as explained in chapter 1.3.2, the developed catheter was expected to provide much better contrast for discriminating ablated from healthy tissue, as opposed to pure ultrasonic sensing catheters [81].

3.4.2 Catheter design and assembly

As can be obtained from the design shown in Fig.3.1, the optoaccoustic catheter comprises 3 major compontents: an electrode for delivery of RF current into the cardiac tissue, a bundle of optical fibers to guide laser light used for optoacoustic signal excitation and an ultrasonic detector to sense optoacoustic pressure waves generated within the target tissue. For the ultrasonic detector a compact PVDF-based needle hydrophone (Precision Acoustics, UK) was used due to its small outer diameter of 1mm and high detection bandwidth. The optical fiber bundle was designed as a ring of multimode optical fibers, each with a diameter of 230 µm (Thorlabs, USA) and the electrode as a metallic tube with an outer diameter of 2.4mm (Conrad Elektronik, Germany), yielding an overall design that is very compact and within the dimensions of clinical ablation catheters.

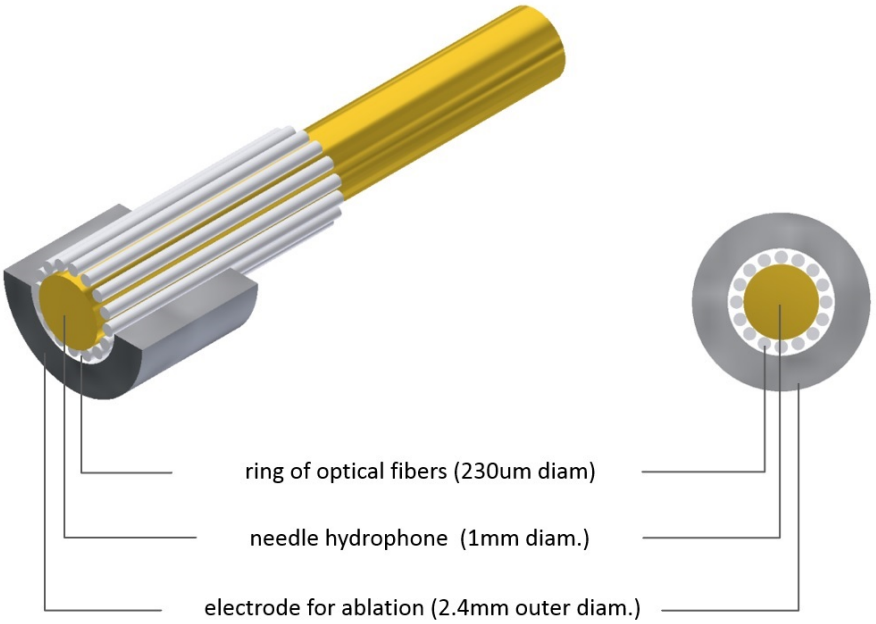

Figure 3.1: Design of optoacoustic intracardiac catheter

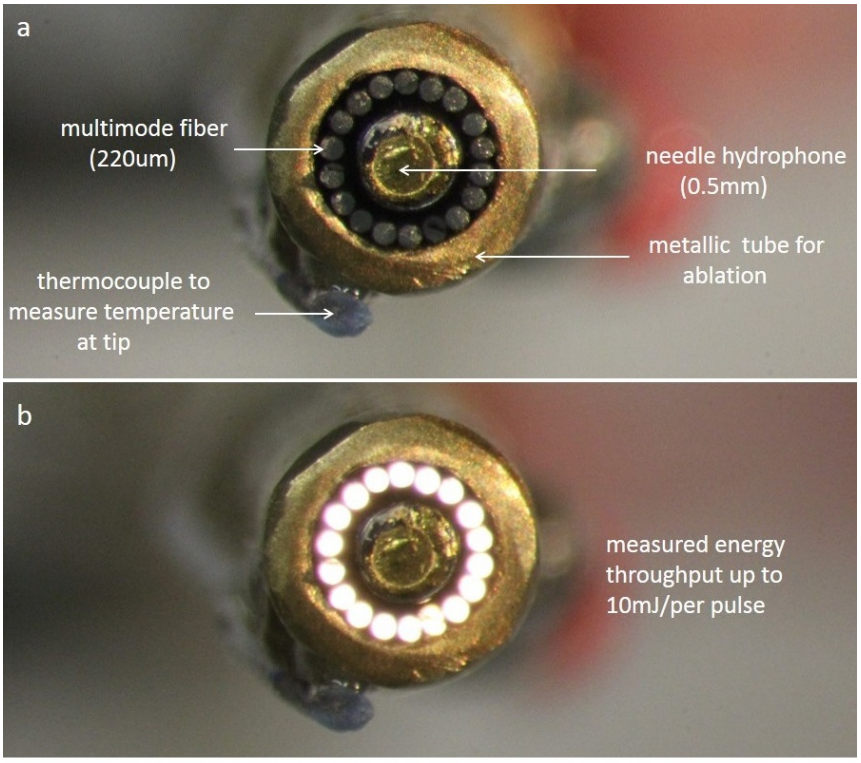

Figure 3.2: Catheter prototype (front view)

Fig.3.2 shows the resulting catheter prototype after all components were integrated. Additionally, a miniature thermocouple (Physitemp Instruments Inc., USA) with a diameter of 0.41mm was attached to the outer electrode in order to measure the temperature generated at the catheter tip (Fig.3.2(a)).
As can be seen in the side-view photograph in Fig.3.3(a), a standard copper wire was soldered onto the metallic tube in order to conduct the ablation current. At the catheter tip (Fig.3.3(b)), the total diameter was measured as ca. 2.4mm, which, in a future design, could be maintained along the entire catheter with an optimized wiring solution. As can also be obtained from (Fig.3.3(b)), while assembling the catheter components, care was taken to ensure that the hydrophone tip protrudes about 0.2mm from the edge of the metallic tube in order to prevent any acoustic reverberations, caused by the inner walls of the metallic tube, to be detected by the hydrophone.

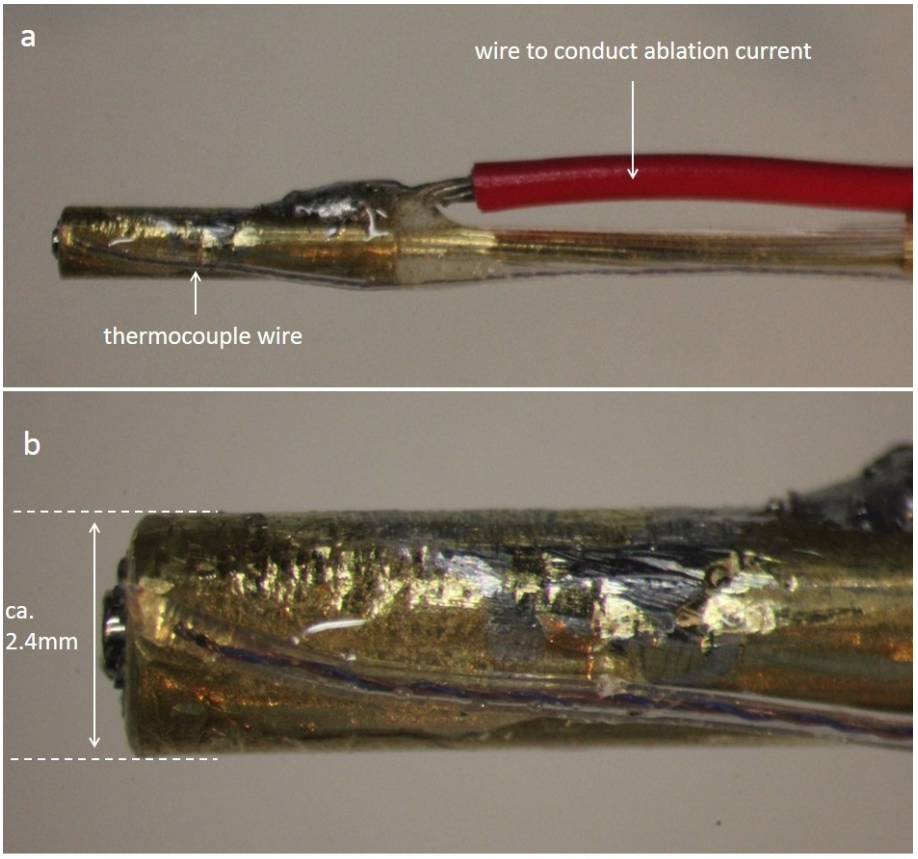

Figure 3.3: Catheter prototype (side view)

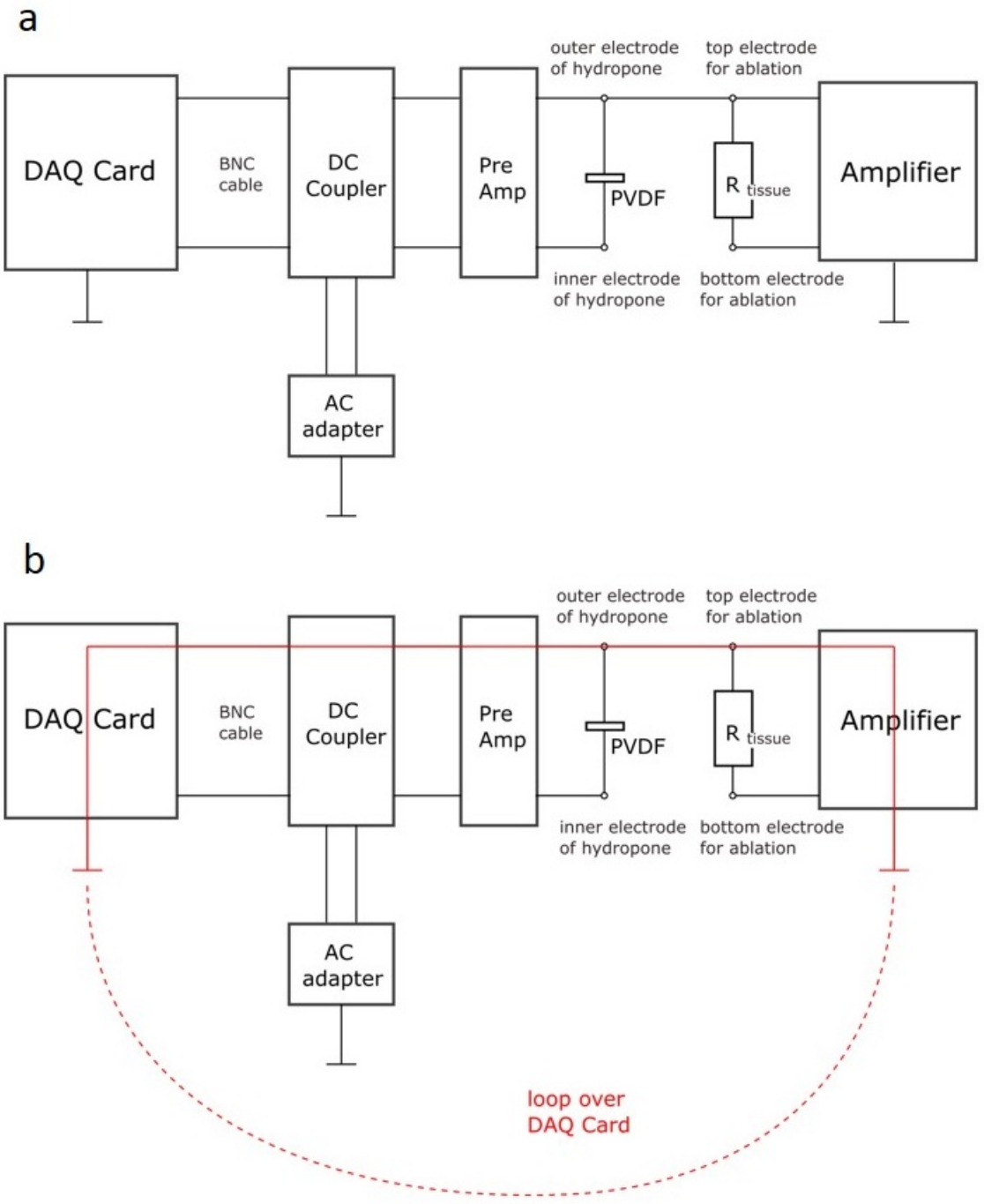

Figure 3.4: (a) electric circuit of the ablation and measurement setup (b) Possible ground loop over the data acquisition (DAQ) card highlighted. Since input and output of the AC adapter are electrically isolated due to the use of a transformer built into the AC adapter, a ground loop is not possible.

Since electric contact between the conducting surfaces of the ablation electrode and the needle hydrophone cannot be prevented, there is a risk that the ablation current will flow over the hydrophone and potentially cause damage, e.g. in the data acquisition electronics. As shown in the electric circuit of the ablation and measurement setup in Fig.3.4(b), the ablation current might flow from the top ablation electrode over the outer electrode of the needle hydrophone if there is a closed circuit, which can be the case if the ground of the DAQ card is connected to the ground of the amplifier. In order to prevent this and ensure safe measurements an opto-isolator circuit (ViTecco GmbH, Germany) with high transmission bandwidth was placed between DAQ card and DC coupler.

3.4.3 Characterization of catheter

In order to characterize the assembled catheter and assess the sensitivity of detecting optoacoustic signals several *ex vivo* experiments were conducted without performing ablation. Fig.3.5 shows an experiment that was set up to excite and detect optoacoustic signals in an unablated and fresh bovine tissue slab.

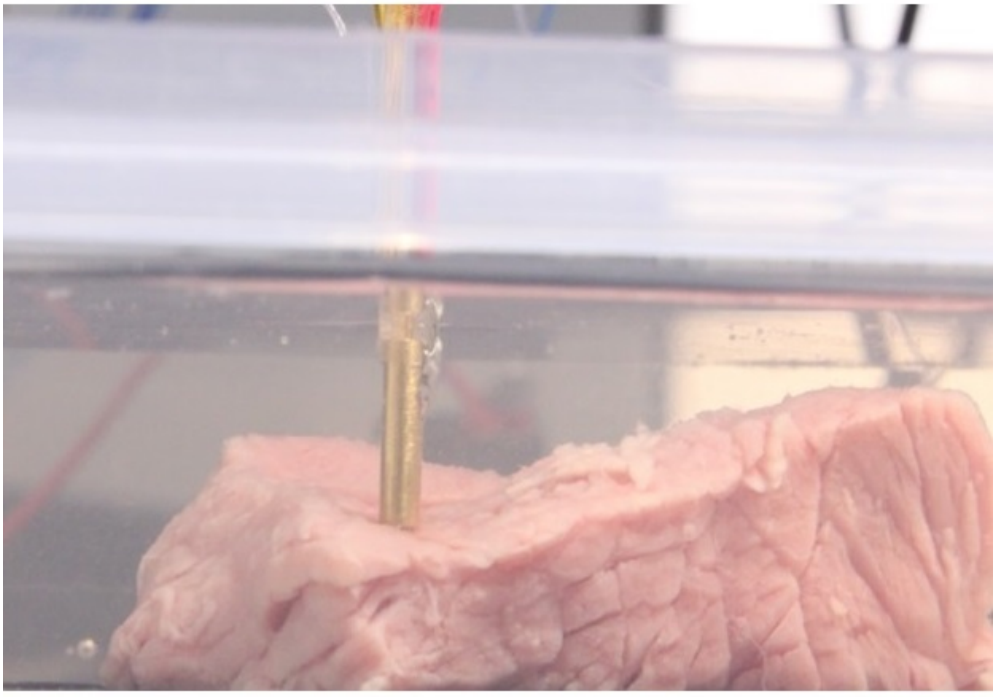

Figure 3.5: Experimental setup: cathether prototype inserted into bovine tissue slab. To maintain acoustic coupling, experiment was performed in a water tank

To this end, the assembled catheter was inserted into the bovine tissue slab, to a depth of about 1mm. Optoacoustic signals excited in the tissue were then detected and analyzed for different tissue slabs and laser settings. Two types of optoacoustic responses were detected: a low-frequency, exponentially decreasing signal (Fig.3.6(a)) and a signal of similar low frequency overlaid by an alternating component of much higher frequency (Fig.3.6(b)).

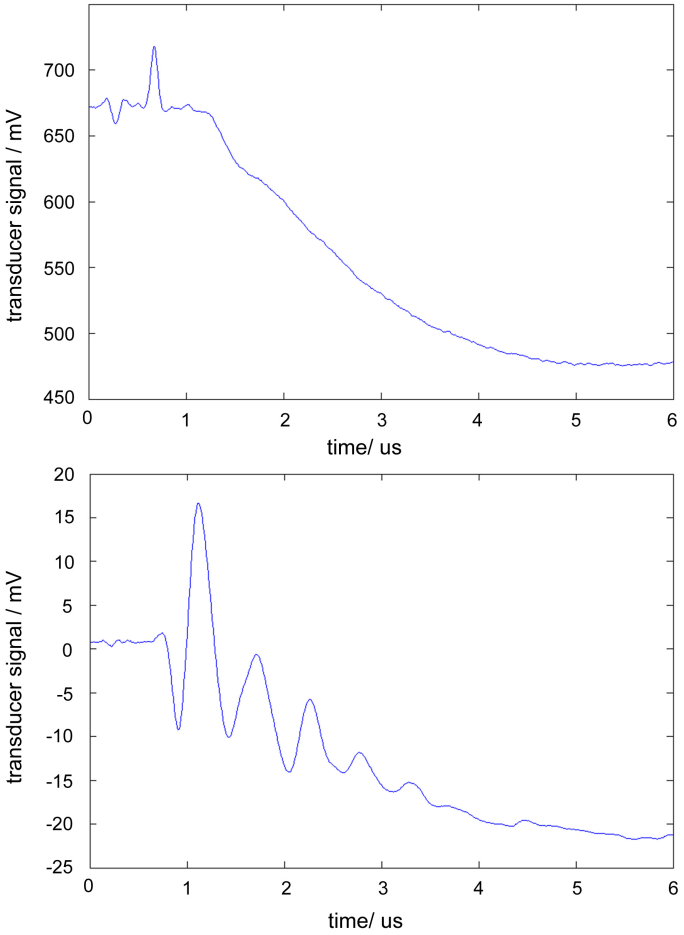

Figure 3.6: types of signals detected: (a) signal with plateau followed by slow exponential decrease (b) signal with slow exponentially decreasing component overlaid by alternating, high frequency component

Neither of the responses was reproducible. Which type of response was detected seemed to also depend on various factors such as tissues structure, insertion depth and pressure. As further experiments conducted at the institute for the purpose of characterizing the detection capabilities of the hydrophone have revealed, the sensor is highly sensitive to

laser illumination. More specifically, laser light backscattered from the illuminated tissue can lead to strong interference in the detected optoacoustic signals. Apparently, the gold coating around the needle hydrophone cannot reflect all of the backscattered light, leading to light absorption and optoacoustic signal excitation within the hydrophone. It was shown that the strong, exponentially decreasing signal of low frequency (Fig.3.6(a)) represented an optoacoustic response from the hydrophone and not from the illuminated tissue. For the high frequency component in the signal shown in Fig.3.6(b), a reasonable hypothesis would be reverberations of optoacoustic waves within the prototype. In order to test this hypothesis, finite difference time domain calculations were performed to simulate acoustic wave propagation. The geometry and acoustic properties of the needle hydrophone were taken into account by using a model provided by the manufacturer of the hydrophone. Simulations showed that reverberations can occur within the hydrophone if the incoming wave front is detected at a large angle of around 70°, which is approximately the angle between the active surface of the hydrophone and the illumination cone formed by the output beam of each multimode fiber.

Experiments with ablation were also conducted in order to characterize the lesions that can be generated using the prototype. A piece of aluminium foil was placed under the tissue slab and acted as the ground electrode. Temperature was measured continuously during the ablation process at the tip of the ablation electrode using miniature type-T thermocouples (Physitemp Instruments Inc., Clifton, New Jersey USA) with a diameter of 0.41mm. Since the PVDF layer within the needle hydrophone cannot withstand temperatures higher than 80°C, the ablation generator was turned off once the measured temperature exceeded 75°C. Experiments performed in bovine muscle tissue slabs produced lesions of a depth of up to 3mm. However, after removing the catheter from the ablation cite, heavily coagulated tissue was attached to the acoustic detector, optical fibers and the narrow spaces between the fibers, and couldn't be removed. Given strong absorption of highly coagulated or even carbonized tissue, the used catheter was not capable to generate the same light fluence as in the first ablation experiment. Therefore, and due to hygienic reasons, this catheter can only be used in a single ablation treatment, if used in a clinical environment.

3.4.4 Outlook for development of clinical probe

Integrating all necessary components for optoacoustic signal excitation and detection as well as for ablation into a single compact catheter leads to several problems. Since the optical fibers are located very close to the acoustic detector there is a high risk of interference: light backscattered from the tissue can enter the acoustic detector and generate a strong response that will dominate the detected signal.

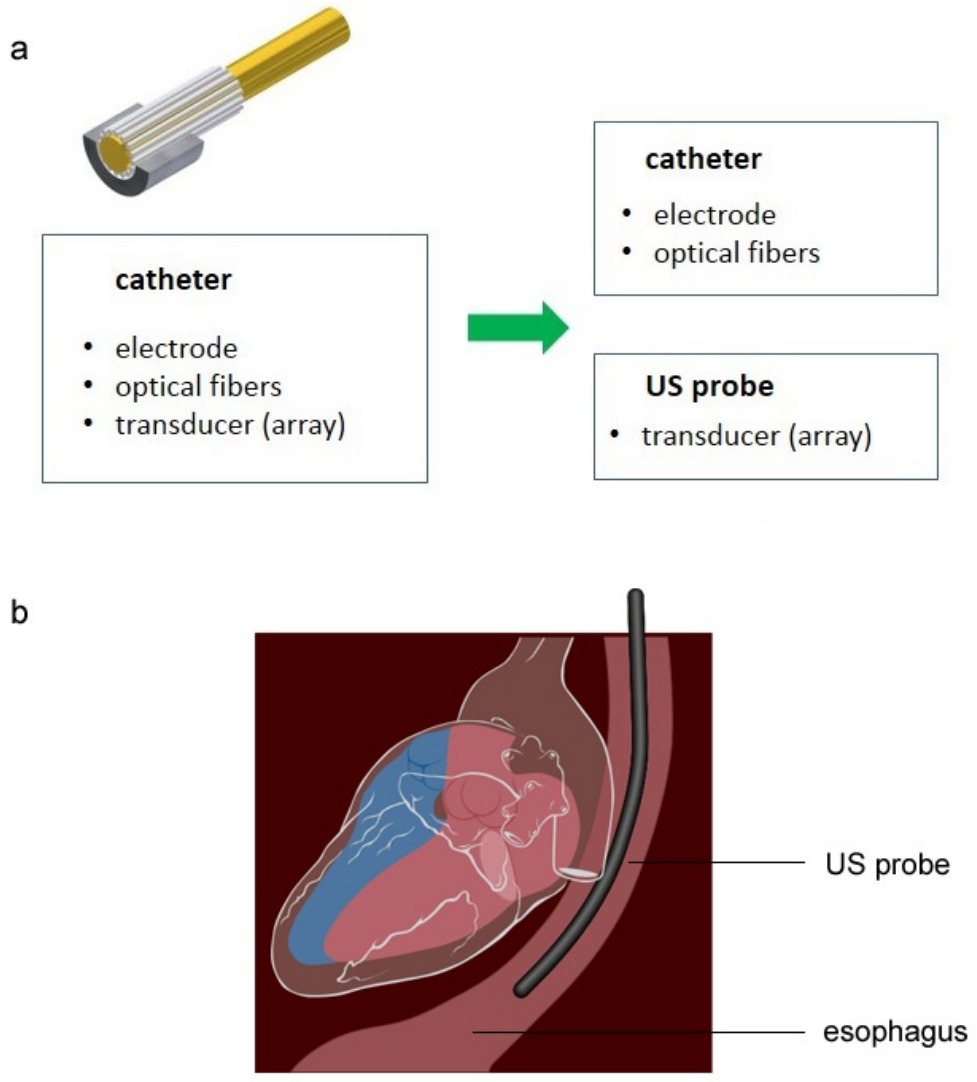

Figure 3.7: (a) Schematic showing a preferred monitoring principle: one catheter for ablation and optoacoustic signal excitation, and an ultrasonic (US) probe for detection of optoacoustic signals (b) example of US probe outside cardiac chamber ("transesophageal echocardiography ultrasound diagram" by Patrick J. Lynch, Creative Commons Attribution 2.5 License 2006)

Moreover, the acoustic wave front generated by the laser beams next to the detector can potentially cause strong reverberations within the detector when detected at a large incident angle. Given both artifacts, from interference and reverberations, it is not possible to discern the optoacoustic response of the illuminated tissue.
The optoacoustic ablation catheter also experienced practical problems that might well prohibit its use for clinical treatments. It was not possible to remove coagulated tissue fragments from the surfaces of the optical fibers and hydrophone as well as from the narrow spaces in between the individual components. As a result, over the course of several ablations, the optoacoustic excitation and detection capabilities deteriorated. Therefore, and also due to hygienic reasons, the proposed optoacoustic ablation catheter can only be used for a single ablation treatment.
Due to above limitations and complications, it is not advisable to integrate all components in a single catheter. As shown in Fig.3.7 (a-b), a more feasible solution would be to only integrate the optical fibers and the electrode in one catheter and then to perform the detection of optoacoustic signals from a different location, e.g. from a compact echocardiography probe inserted into the esophagus, or from outside the patient by a standard, clinical echocardiography probe. This way the lesion generated during ablation can be fully illuminated in order to ensure optimal optoacoustic signal generation and optoacoustic waves can be detected at a suitable position with higher sensitivity, preferentially with an imaging probe.

3.5 Study 1: Monitoring of lesion progression based on optical contrast

3.5.1 Motivation

In chapter 3.4.4 it was suggested to decouple the ablation electrode, optical fibers and the ultrasonic detector. A feasible monitoring concept for clinical settings would be for example to integrate fibers and electrode in one catheter and to detect optoacoustic signals with a seperate ultrasonic probe. The aim of this study was to use the technology currently available in the institute for monitoring ablation. Therefore a slightly different decoupling method was used: optoacoustic signals were generated and detected with the same handheld detector, which was already used in a previous study (see chapter 2.4), while ablation

was generated with a separate electrode. This way, problems observed with the integrated optoacoustic ablation catheter could be avoided. Moreover, using the optoacoustic hand-held detector it was possible to perform ablation and optoacoustic imaging simultaneously and in real-time, which has not been accomplished so far.

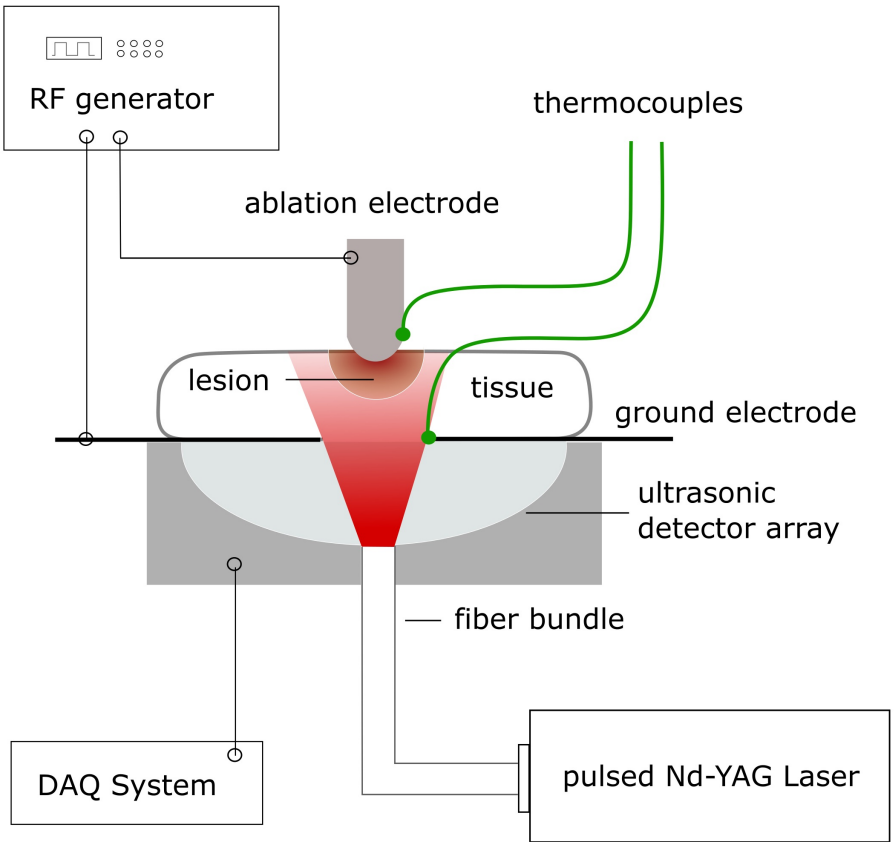

Figure 3.8: Schematic illustrating the experimental setup of the ablation experiment.

3.5.2 Experimental design

The experimental setup is shown in Fig.3.8. Excitation of optoacoustic responses was done using an optical parametric oscillator (OPO) laser source (Phocus, Opotek Inc., Carlsbad, California USA) capable of generating nanosecond duration pulses in the wavelength range between 720nm to 860nm. The illumination is directed toward the tissue using a custom made silica fused-end fiber bundle (CeramOptics GmbH, Bonn, Germany), creating a fluence rate of approximately 20mJ/cm^2 at the tissue surface, in accordance

with safety standards [88].
Acoustic detection was performed with a custom-made matrix ultrasonic array (Imasonic SAS, Voray sur l'Ognon, France) consisting of 256 elements distributed on a spherical surface with 40mm radius [65, 66]. The center of the spherical surface of the detector array was positioned such that it aligned with the location of the ablation electrode. More details on the acoustic detector array can be found elsewhere [65]. The acoustic signals were recorded with a custom designed multi-channel data acquisition system (Falkenstein Mikrosysteme GmbH, Taufkirchen, Germany).
Radiofrequency ablation was performed using a 3mm diameter ablation electrode. The ground electrode of 20cm^2 in surface area contained an aperture for allowing the fiber light to pass through and illuminate the tissue sample. This ground electrode of 20cm^2 in surface area was placed below the tissue sample under a 40mm thick layer of agar gel used for acoustic coupling. The tissue sample and the ablation electrode were submerged in solution for heat dissipation. Temperature was measured continuously during ablation at the tip of the ablation electrode and at the illumination side of the tissue sample using miniature type-T thermocouples (Physitemp Instruments Inc., Clifton, New Jersey USA) with a diameter of 0.41mm. Experiments were performed with either water or saline used for the coupling agar gel and the heat dissipation solution; in either case, the temperature at the ablation electrode tip was controlled in an identical manner and the results showed no dependence on whether water or saline was used as ablation power, lesion size, and the resulting images - all remained constant.
Potential influence of the radiofrequency energy application on the imaging process was assessed by performing experiments with the radiofrequency energy deposition halted during the image acquisition window (1ms every 100ms); however, imaging was also performed during experiments without halting the ablation process. However, no notable differences were observed in terms of image quality, noise or lesion formation as compared to experiments performed without halting the ablation process.

3.5.3 Experimental procedure

Fresh porcine hearts excised shortly before the experiment were used. Segments of homogeneous ventricular myocardial tissue of thicknesses ranging from 4 to 10 mm were excised with a clean scalpel before placement in the experimental setup. Optoacoustic measurements were recorded of the initial homogeneous tissue samples with illumination

wavelengths from 740nm to 860nm, in increments of 20nm, to empirically determine the light fluence correction at each experimental wavelength, discussed in the following section. In each ablation experiment, ablation was carried out for 60s at a steady-state power of approximately 5W. The ablation power was adjusted to maintain a temperature of 75°C at the surface of the ablation electrode. During each ablation, optoacoustic signals excited by a fixed illumination wavelength were simultaneously recorded for all 256 detector elements at a frame rate established by the pulse repetition frequency of the laser (10Hz). After completion of the ablation process, the tissue sample was allowed to cool to room temperature (25°C) and additional multispectral data were recorded using illumination wavelengths from 740nm to 860nm, in increments of 20nm, in order to obtain the absorption spectra of the lesions. Finally, the ablated samples were sectioned with a clean scalpel and inspected visually.

3.5.4 3D Image Reconstruction and Fluence Correction

Three-dimensional optoacoustic images were obtained from the measured data by means of a tomographic reconstruction algorithm. The algorithmic work-flow included band-pass-filtering of the signals between 0.1 and 3MHz to remove low frequency offsets, high frequency noise and reconstruction artefacts before a model-based inversion technique with good quantitative performance was applied [89]. This algorithm assumes a homogeneous speed of sound distribution in the medium, empirically set to 1540 m/s based on the corresponding speed of sound values of soft tissue and agar. While the considerable temperature increase occurring during ablation in the treated tissue volume leads to speed of sound changes, the same value of the speed of sound was used in all reconstructions because the heat-affected zone is relatively small and the agar gel, remaining near room temperature during the entire ablation process, constitutes the vast majority of the acoustic propagation volume. Thus, errors in the reconstructed position due to temperature-induced speed of sound variations are negligible. The reconstructed optoacoustic images were first normalized by the measured per-pulse laser energy at each wavelength and then corrected for optical attenuation by assuming the light fluence along the axial direction follows an exponential decay function, starting at unity at the tissue surface. The rate of exponential decay was approximated at each wavelength between 740and 860nm based on the respective empirically-determined axial decay in optoacoustic image for the uniform tissue sample before start of ablation.

3.5.5 Results

3.5.5.1 Static Lesion Visualization

Fig.3.9 shows a maximum amplitude projection through lateral planes of the reconstructed volume from a representative imaging experiment performed at 860nm.

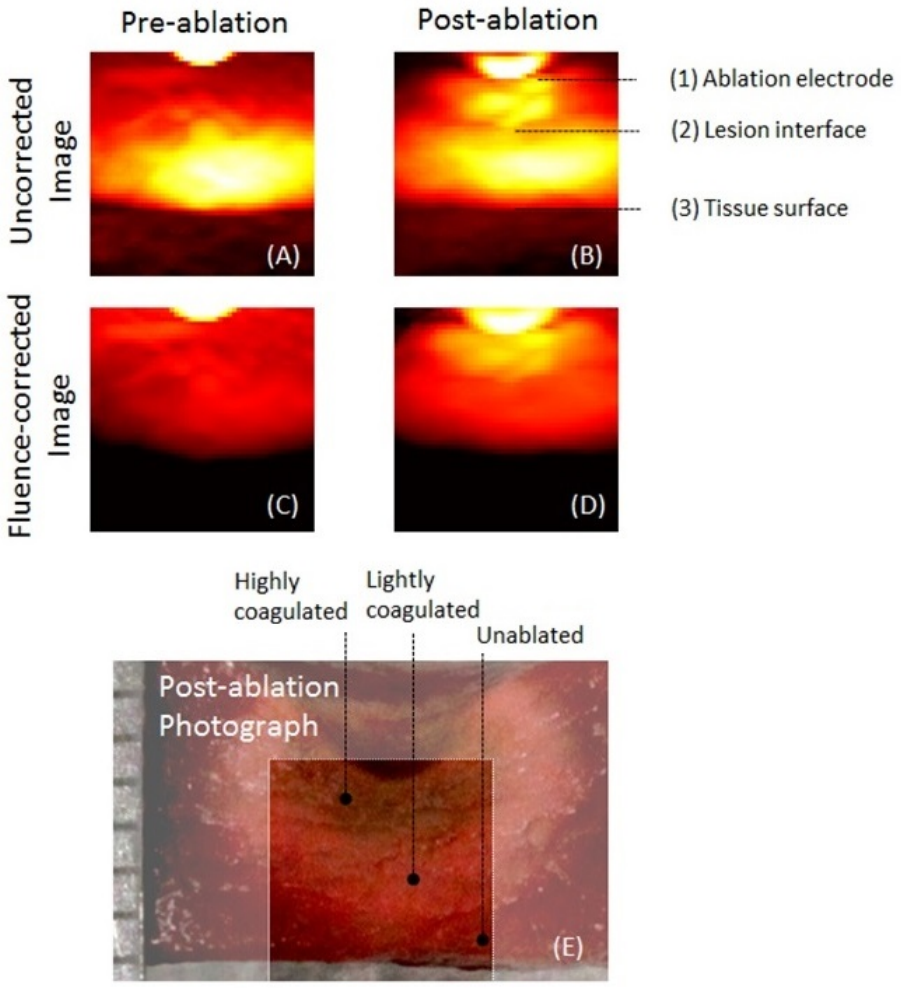

Figure 3.9: Optoacoustic images from a representative tissue sample (Sample 1) at 25°C. Illumination wavelength of 860nm. (a) Pre-ablation raw image. (b) Post-ablation raw image. (c) Pre-ablation image corrected for fluence. (d) Post-ablation image corrected for fluence. Image dimensions in (a)-(d) are 5 x 5mm. (e) Cross-sectional photograph taken after experiment with approximate imaging window marked; ruler increments 1mm (far left). (Figure published in [90], Copyright 2014, Wiley Periodicals, Inc.)

Fig.3.9(a) and (b) show the images before and after ablation, respectively, both at room temperature. Three distinct interfaces in the signal are clearly visible, from top to bottom: (1) between the electrode and the tissue sample, (2) between a region of high optoacoustic signal and a region of lower signal within the tissue sample, and (3) the illuminated surface of the tissue sample. The fluence correction yields an optoacoustic image of uniform intensity for the tissue sample prior to ablation (Fig.3.9(c)), and two areas of distinct intensity can be seen in the tissue sample after ablation (Fig.3.9(d)) representing damaged and undamaged tissue. The fluence correction in the volume of the necrotic tissue should not necessarily be the same as in the unablated tissue volume because of changes in optical attenuation of the damaged tissue, and a non-uniform fluence correction in the axial direction could therefore be used after lesion formation begins. For practical purposes of visualizing the lesion boundary, the uniform fluence correction was applied here, assuming uniform optical attenuation in the entire sample However, fluence correction does not constitute a prerequisite for successful application of our technique since the boundary of the lesion can be clearly discerned in the pre-corrected image.
Fig.3.9(e) presents a photograph of a cross-sectional view of the lesion cut along its central region. The lesion contains three distinct regions, one highly coagulated region close to the ablation electrode tip (darker, brownish), a less coagulated region (lighter, whitish), and the unablated tissue (reddish). There is a slight discrepancy in the imaged and photographed tissue thickness due to compression under the ablation electrode. Approximately a 27% compression of the total tissue thickness is observed in the current case, which is reasonable to expect from compression due to electrode placement and contact pressure. The depth of the visualized lesion is measured in the reconstructed image in Fig.3.9(d) as 1.2mm; if one assumes a uniform compression of the sample by the electrode, and thus a uniform expansion of the tissue in the post-ablation sample analysis, the lesion interface in the image can be assumed to represent the boundary of the highly coagulated tissue volume which extends to a depth of 1.6mm below the electrode in the cross-sectional photograph of the ablated tissue after slicing through the center of the lesion (Fig.3.9(e)). Presented in an alternate manner, the lesion depth is approximately 44% of the total tissue thickness in both the reconstructed optoacoustic image and the post-ablation photograph.
It has to be noted that, in the current imaging setup with 20 mJ/cm^2 fluence at the tissue surface, it was possible to get a sufficient signal-to-noise ratio in order to resolve the lesion boundary in up to 6mm thick samples (Fig.3.10) whereas experiments with 10mm thick tissues suffered under strong noise and yielded insufficient contrast (data not shown).

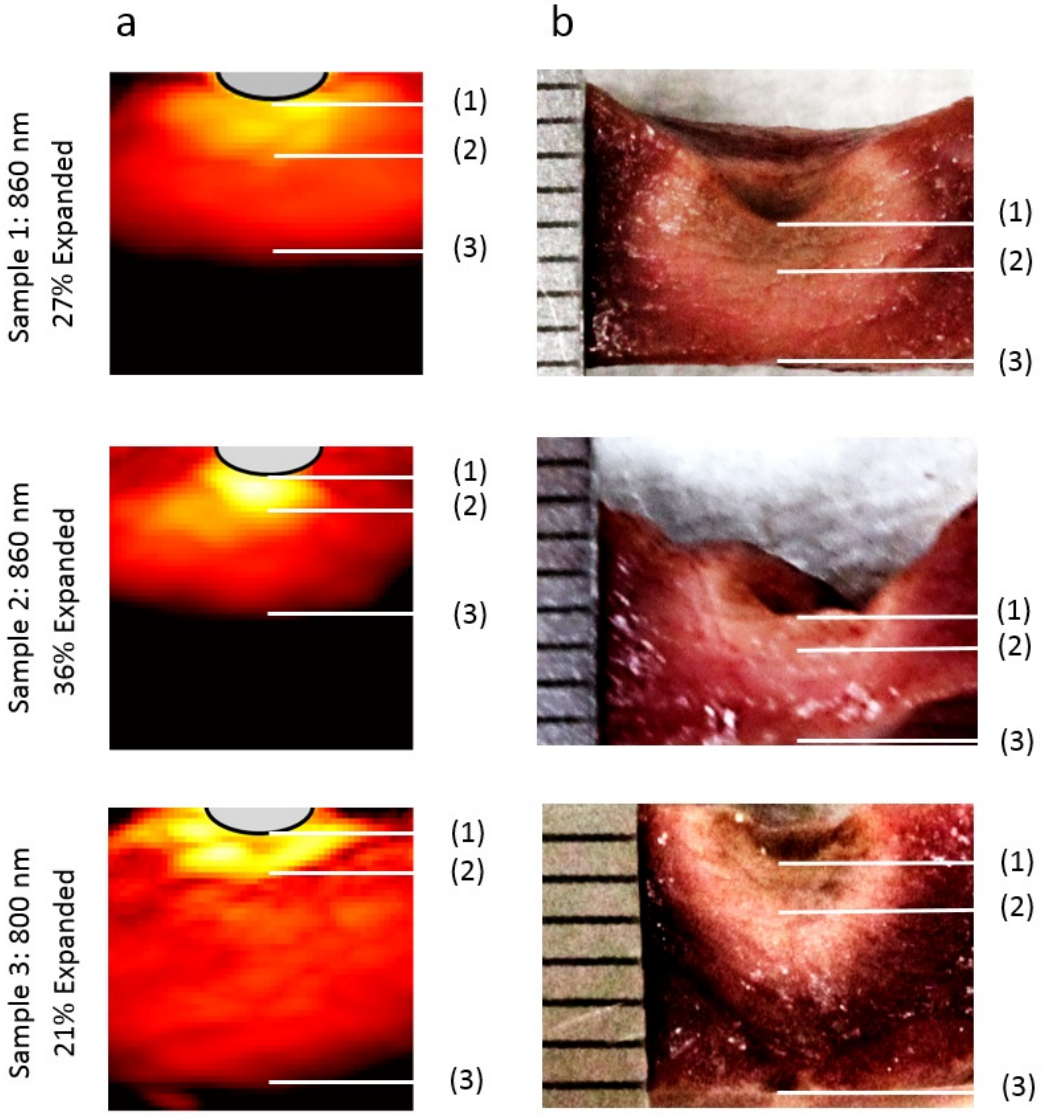

Figure 3.10: (a) Fluence-corrected reconstructed optoacoustic images (maximum amplitude projections) from three ablation experiments at room temperature. Image dimensions are 5 x 5 mm. (b) Corresponding post-ablation cross-sectional photographs. Scale differs slightly between photographs, but can be obtained from ruler increments of 1 mm on the left side. The key features are marked:(1) Ablation electrode, (2) Lesion interface, (3) Tissue surface; the location of the lesion interface in the cross-sectional photographs is marked based on the position determined in the optoacoustic image after scaled with the appropriate tissue compression/expansion factor, and agrees well with the depth of the highly coagulated tissue in the post-ablated sample.

For all experiments performed, the visualized lesion depth in the optoacoustic images (Fig.3.10(a)) was in agreement with the depth of the boundary of the highly coagulated tissue volume in the post-ablation photographs (Fig.3.10(b)), assuming uniform compression in the tissue thickness by the electrode. The electrode compression was not specified prior to each experiment, but instead determined by comparing total thickness of the specimen in the post-ablation photograph and the reconstructed image. The regions of damaged tissue due to ablation can be clearly identified in the photographs, and thus no staining was necessary in the post-ablation histological examination. The tissue compression ranged from 21% to 36% in all experiments, while the lesion depth, as observed in the reconstructed images, always matched the lesion boundary seen in the photograph within the tolerance of the tissue compression. Furthermore, the position of the electrode, lesion interface, and tissue surface from the three post-ablation images from three experiments are matched with their respective post-ablation photographs in Fig.3.10, with the positions scaled by the appropriate compression factor. These results confirm that the lesion interface seen in the optoacoustic image is in good agreement with the boundary of the highly coagulated zone.

As can be readily obtained from Figs.3.9(d) and 3.10(a), stronger optoacoustic responses are clearly observed within the strongly coagulated tissue volume. Both optical absorption and scattering of heat-damaged myocardial tissue have been previously reported to be higher as compared to unablated tissue in the spectral range between 600 to 700nm [33, 91, 92]. The increase in optical absorption coefficient is hypothesized to arise from the denaturation of blood [92]. Assuming that the optical properties behave similarly in the near-infrared spectrum and considering that optoacoustic signals correlate with light absorption supports our assumption that the region of stronger optoacoustic signals represents the highly-coagulated tissue of the RFA-generated lesion. Additionally, the optoacoustic signal further depends on the Grueneisen parameter, which is a function of the thermal expansion coefficient, the speed of sound, and the heat capacity, and these parameters are also expected to change in heat-damaged tissue [51].

3.5.5.2 Dynamic Lesion Visualization

The dynamics of the lesion formation can be characterized from the sequence of images, as shown in an example of monitoring results in Fig.3.11. Lesion formation is observed after a short heating period of 10 seconds, a delay that approximately coincides with the

time the temperature measurement at the electrode reaches 50°C, which has been previously suggested as the critical temperature for lesion formation [93]. The ablation process can be readily identified from the high optoacoustic contrast produced at the boundary of the highly coagulated tissue. After the lesion formation begins, the region of ablated tissue increases in size before nearly reaching a steady state value.

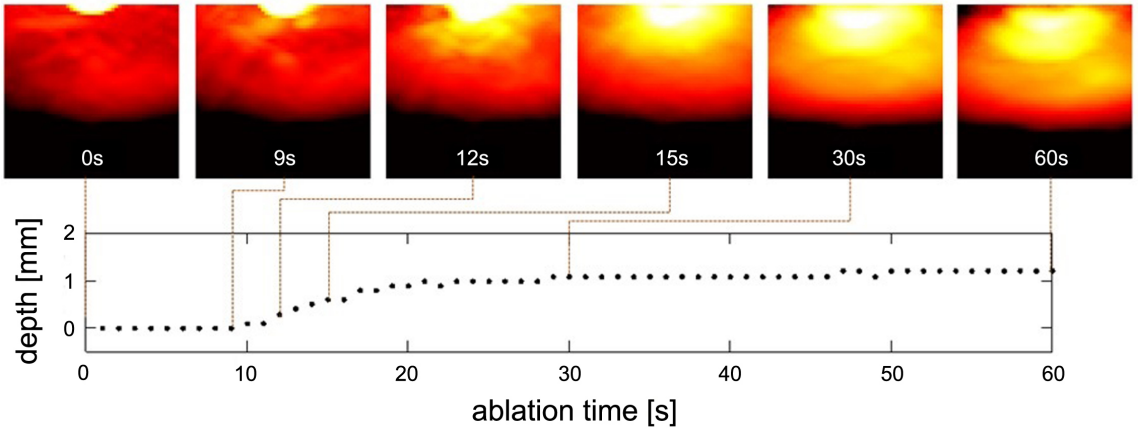

Figure 3.11: (top) Time evolution of the RFA-generated lesion from Sample 1 (results are from the same experiment as in Fig.3.9) with illumination wavelength of 860nm. Lateral MIP planes (corrected for fluence) from the 3D reconstructions are shown at selected time points. Image dimensions in each frame 5mm x 5mm. (bottom) Progression in time of the lesion boundary, as defined by an image intensity threshold. (Figure published in [90], Copyright 2014, Wiley Periodicals, Inc.)

The optoacoustic images depicting the time evolution of the lesion presumably convey two main effects: first, optical property changes in the ablated tissue volume and second, temperature changes in the heated tissue volume, with the latter primarily affecting the optoacoustic signal strength due to increase in the Grueneisen parameter [51]. The effect of temperature on the optoacoustic signal is clearly observed in Fig.3.11 at the bottom tissue surface, where optoacoustic signal intensity increases with time as the tissue surface is slowly heated with no tissue damage occurring in this area. The temperature distribution within the tissue sample should follow a smooth continuous profile, and therefore, the sharp signal change seen in each image can still be clearly distinguished as the lesion boundary even during ablation when temperature variations are present. Speed of sound changes in the tissue can also influence the time-of-flight of the optoacoustic signals, and thus, precise location of the features in the images. However, as discussed previously in section 3.5.4, these changes lead to negligible shifts in the images.

The depth of the lesion can be marked by the boundary of the necrotic, highly-coagulated tissue volume. One can define the leading edge of the lesion boundary as the first instance from the illumination-side surface of the tissue sample along the centerline signal where the optoacoustic signal exceeds an arbitrary threshold, in this case chosen to be a 30% increase from the original signal. With this arbitrary definition of the lesion boundary, the growth of the lesion depth in time can be then automatically established from the images, as shown in Fig.3.11. The precise correlation between the selected threshold and the physical lesion properties is still a matter which must be calibrated based on the desired extent of damage to be detected. The interface at the leading edge of the highly coagulate tissue is approximately 0.3mm wide, indicating that a precise lesion boundary position will have an uncertainty of this magnitude.

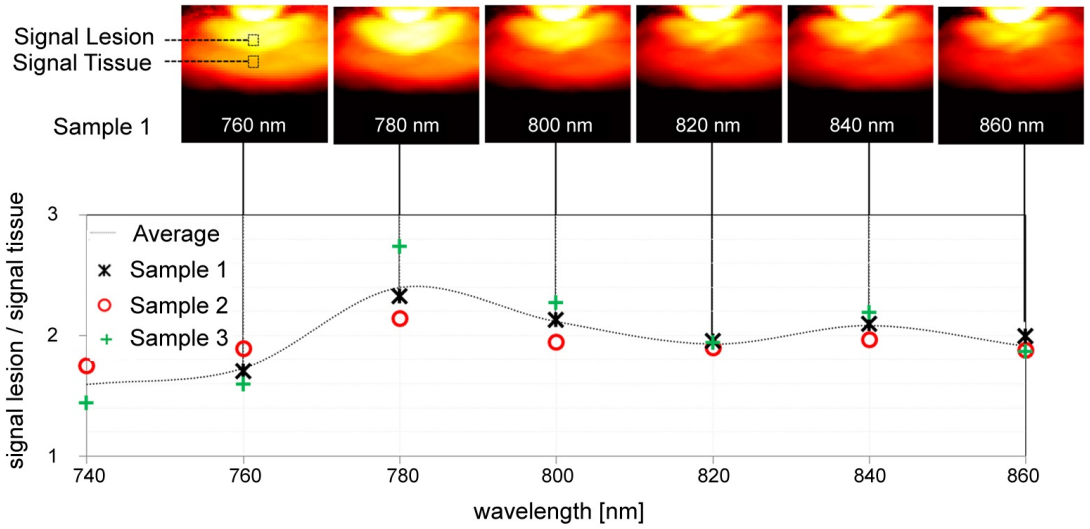

Figure 3.12: (top) Reconstructed images of the lesion in sample 1 (cooled down) at different illumination wavelengths. Each image normalized for laser power and corrected for fluence. Image dimensions 5mm x 5mm. (bottom) Contrast spectra from lesions generated in three different tissue samples. The black dashed line represents an approximation of the spectral shape for 740nm to 860nm determined through a fit to the average of the three experiments. (Figure published in [90], Copyright 2014, Wiley Periodicals, Inc.)

3.5.5.3 Spectral image analysis of RFA-generated lesions

Wavelength dependency of the reconstructed images between 740nm to 860nm was studied in the post-ablated sample cooled to 25°C. The respective fluence correction was sepa-

rately determined for each wavelength. As illustrated in Fig.3.12, the optoacoustic signal from the unablated tissue region of the image shows a maximum for a wavelength of 760nm, suggesting deoxygenated hemoglobin (with an absorption peak at 760nm) as the primary absorber in the unablated *ex vivo* tissue sample. The image contrast between highly-coagulated and surrounding tissue can be quantified by computing the ratio of the average value in two regions of interest located at opposite sides of the interface of the highly-coagulated tissue, as shown in the image for 760nm in Fig.3.12.
The contrast spectrum for illumination wavelengths from 740nm to 860nm and for lesions generated in 3 different experiments is plotted in Fig.3.12 (bottom). The contrast spectra derived from the different lesions have slightly different quantitative values, suggesting that the contrast may have some dependence on the morphology of the particular lesion. However, the spectral shape follows the same pattern for all studied lesions with contrast maximized near 780nm and minimized at the shorter wavelengths.

3.5.6 Discussion

Currently, success of RFA treatments depends on expertise and experience of the clinician in assessing lesion formation, leading to an undesirable amount of ineffective and failed treatments. An effective lesion monitoring technique would likely improve the learning curve for clinicians and would undoubtedly increase the success rate of RFA treatments. The current study demonstrates that three-dimensional optoacoustic imaging can provide powerful and effectic feedback for monitoring RFA ablation. Real time imaging was shown at a rate of 10Hz, while higher imaging rates are readily possible using lasers with higher repetition rates. Optoacoustic imaging shows excellent absorption-based contrast at the boundary of the highly coagulated tissue, providing an advantage over previously suggested ultrasound-based techniques [81–83]. Compared to purely optical techniques [87], the method can also visualize significantly deeper lesions. Furthermore, the current work demonstrates truly three-dimensional imaging of lesion formation dynamics, as opposed to previously reported two-dimensional, static optoacoustic lesion assessment done in post-ablated, cooled samples [16]. This illustrates that optoacoustics has the potential to capture reversible temperature changes in the tissue simultaneously with the irreversible changes in tissue structure. Finally, we were able to image the lesion contrast using only a single illumination wavelength, which yields a practical and cost effective solution for monitoring radiofrequency ablation.

In optoacoustics, imaging depth is limited due to the fluence decay within the illuminated tissue. In the current study, sufficient image quality was achieved in tissue slices up to a depth of 6mm. However, in the infra-red spectrum, higher fluence values are allowed for clinical imaging. For instance, the maximum permissible exposure (MPE) recommended for skin imaging at 700 nm is 20 mJ/cm^2 but increases to 40 mJ/cm^2 at 860 nm [88]. Therefore, deeper imaging depths are expected to be possible using a wavelength in the infra-red spectrum and higher illumination fluence. It should be also noted that optoacoustic imaging has been successfully applied up to depth of 15mm in soft human tissues without applying signal averaging [65].

Experiments were performed using excised samples of homogeneous porcine myocardial tissue. Tissue from the ventricles was used for this proof-of-concept study, because a larger volume of homogeneous tissue leads to clearer delineation of the RFA-generated lesion in the optoacoustic images. Optoacoustic contrast is expected to also delineate the highly coagulated tissue when ablation is performed in atrial myocardial tissue, though the quantitative contrast may differ. The ability to visualize the lesion boundary should not be affected when ablating through different tissue types, as optical heterogeneities in the imaged volume should not affect the basic ability of sound and light to pass though soft tissues. On the other hand, the presence of heterogeneities, such as scar tissue, may affect the fluence distribution within the imaged volume, thus, a more complex fluence correction method may become necessary to compensate for light attenuation more accurately. However, the lesion boundary would still be visible in the optoacoustic images even without applying fluence correction, as illustrated in Fig.3.9(b). In fact, optoacoustic imaging can even provide additional capacity of visualizing scar tissue or other heterogeneities prior to the ablation and thus attain further useful feedback information.

Compared to the current, *ex vivo* study, radio-frequency ablation performed *in vivo* may experience different ablation dynamics and contrast at the lesion boundary. For instance, the tissue is expected to have a higher oxygenation level when imaging is peformed *in vivo*, which could lead to changes in the contrast spectrum. However, at the isobestic point of hemoglobin at a wavelength of approx. 800 nm, optical absorption of oxygenated and deoxygenated hemoglobin is nearly identical, therefore changes in blood oxygenation level should not influence the optoacoustic contrast at this particular wavelength. The current study has shown good optoacoustic contrast at the lesion boundary at 800nm, as can be obtained from Fig.3.12. Therefore, similar good contrast can be expected in an *in vivo* experiment despite changes in blood oxygenation level. Indeed, certain biophysical responses in RFA-treated tissue have only been observed during *in vivo* studies, such as

edema formation [94], and therefore could not be considered in our *ex vivo* study. Yet, absorption-based contrast between necrotic and native tissue will remain also when ablating living tissues. Therefore, the presence of optoacoustic contrast at the lesion boundary should not be affected or might even be enhanced by the high blood content in living tissues. However, further investigations are clearly necessary to study any quantitative changes in the optoacoustic contrast spectra at the lesion boundary during *in vivo* tissue ablation, in order to provide more realistic data that is more representative for a clinical ablation scenario.

Many RFA treatments are performed using saline-irrigated-tip catheters to prevent overheating of the electrode and tissue surface [95]. Despite the fact that the current study utilized a non-irrigated-tip catheter, the properties of a lesion formed with an irrigated-tip catheter can be expected to be similar to the current results, thus still resulting in sufficient optoacoustic contrast to clearly delineate the areas of tissue coagulation. Nevertheless, the lesion formation dynamics and the final lesion size may be different when using an irrigated tip catheter, which will also be the subject of future investigations.

3.5.7 Conclusion

This study demonstrates that optoacoustic monitoring of RFA generated lesions formed in myocardial tissue can be achieved in three dimensions and real time by utilizing the strong optical contrast observed at the lesion boundary. Sufficient contrast can be obtained using only a single excitation wavelength, with the optimal illumination wavelength in the infrared spectrum found to be near 780 nm as shown in Fig.3.12. This technique is capable of fast monitoring of lesion formation, demonstrated here at a frame rate of 10 Hz but much finer time resolution is readily possible by using commercially available lasers with higher pulse repetition frequency.

While further development is needed to transition the proposed method into clinical use, especially with respect to the design of prototypes that can be used under clinical constraints (see section 3.4.4), the current study provides a clear indication that optoacoustic imaging has the potential of three-dimensional real-time imaging of RFA lesion formation with strong absorption-based contrast at the lesion boundary.

3.6 Study 2: Monitoring of lesion progression based on temperature

3.6.1 Motivation

In the previous study (chapter 3.5) an optoacoustic imaging method was shown that is capable of visualizing the highly damaged inner part of a lesion formed during RF ablation. This region is characterized by strongly coagulated tissue, typically showing brownish colour and increased stiffness, and represents the volume of highest tissue damage. A method capable of visualizing this volume might be of high practical interest. However, in all of the experiments conducted for the previous study, it was observed that only a fraction of the lesion generated shows strong coagulation, the majority of the lesion shows mild coagulation only.

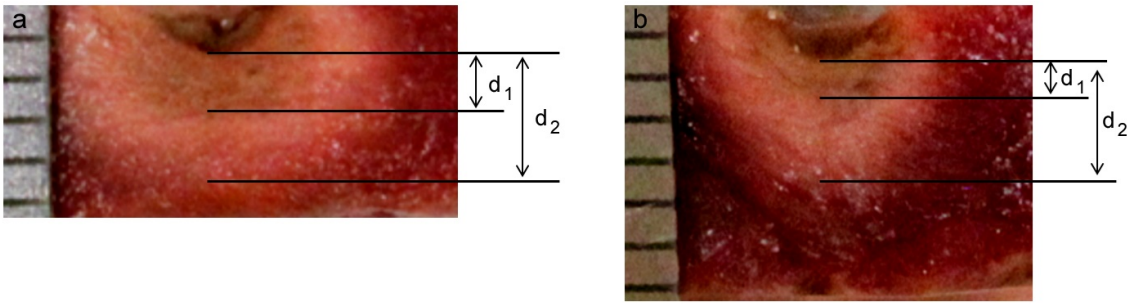

Figure 3.13: lesions showing varying extent of tissue damage. (a) depth of strongly coagulated tissue d_1=1.4mm, depth corresponding to discoloration d_2=3.1mm. (b) depth of strongly coagulated tissue d_1=0.8mm, depth corresponding to discoloration d_2=2.9mm.

Figs.3.13(a) and (b) show two samples from the previous study with strongly coagulated regions of a depth of 1.4mm and 0.8mm, respectively. It can be clearly seen that the rest of the lesion volume is only mildly coagulated.

Several methods have been proposed to mark the boundary of the mildly coagulated part of the lesion. A simple model assumes tissue damage to occur once the critical temperature of 50°C is reached [96]. It was also reported that tissue discolouration, as observed in cross-sectional photographs of post-ablated tissue such as in Fig.3.13, occurred at a higher tissue temperature of 60°C during RF ablation of bovine heart tissue. Therefore,

we can estimate the total depth of the lesion to be greater than the depth obtained from discolouration in the cross-sectional photograph. For the lesions in Figs.3.13(a) and (b) the depth obtained from discolouration is shown by d_2. The total depth of the lesion can be estimated to be greater than 3.1mm in Fig.3.13(a) and greater than 2.9mm in Fig.3.13(b). Consequently, the method shown in chapter 3.5 can only visualize a fraction of less than 45% of the total lesion in Fig.3.13(a) and a fraction of less than 28% in Fig.3.13(b).
Moreover, depending on the ablation parameters (slow ablation compared to fast ablation; maximum temperature at electrode tip of 70°C compared to 80°C or even 90°C; clean electrode compared to dirty electrode) the size of the strongly coagulated region can vary considerably. Various experiments conducted for the previous study have shown that, when ablation was performed at low electrode tip temperatures of approx 70°C no strong coagulation was observable in the lesions generated.
Therefore, it will be crucial to find a method that is capable of detecting the boundary of the mildly coagulated region. As the previous study has shown, the optoacoustic images obtained during real-time dynamic monitoring of the ablation process convey two important effects: strong optical contrast at the lesion boundary and a clearly visible heat-induced intensity gradient throughout the heated tissue volume. A strong relationship between optoacoustic signal amplitude and temperature in heated tissues has been shown [51], which might facilitate measuring tissue temperature by analysing changes in optoacoustic signal strength during ablation. Building on this temperature dependency of optoacoustics, the aim of this study was to compute a temperature map from optoacoustic images acquired dynamically during a full ablation sequence and to evaluate whether a temperature map can provide an accurate estimate of the dimensions of the mildly coagulated lesion.

3.6.2 Materials and methods

3.6.2.1 Experimental data

For this study no further ablation experiments were conducted. Instead the analysis was conducted on the existing data acquired during various experiments that were conducted within the previous study, as described in chapter 3.5. Reconstruction of optoacoustic images was performed using the same model-based reconstruction algorithm (see 3.5.4).However, in this study, reconstructed optoacoustic images were not analysed with

respect to changes in optical contrast at the lesion boundary, as done previously, but with respect to reversible changes in tissue temperature.

3.6.2.2 Algorithm for temperature mapping

A simple algorithm was implemented and tested. It relies on the linear relationship between optoacoustic signal strength and temperature that was observed during heating of tissue samples without coagulation [51]. In case of optoacoustic imaging, the linear relationship at time instant t between the map representing temperature distribution in the heated tissue $T_t(x,y)$ and the reconstructed optoacoustic image $I_t(x,y)$ can be written as

$$T_t(x,y) = \alpha \times I_t(x,y) + \beta \tag{3.1}$$

using constants α and β with the dimension [°C]. Given measurements of $T_t(x_{ref}, y_{ref})$ at two instances during a heating process without coagulation, performed at a reference position (x_{ref}, y_{ref}) and the corresponding optoacoustic signals $I_t(x_{ref}, y_{ref})$, the constants α and β can be obtained.
In the following initial study, a simplification is made by assuming a direct proportional relationship between the temperature map and the optoacoustic image, i.e. $\beta \approx 0$. Using this approximation, a temperature map $T_t(x,y)$ can be computed for the time instant t

$$T_t(x,y) \approx \frac{I_t(x,y)}{I_{t_0}(x,y)} \times T_{t_0}(x,y) \tag{3.2}$$

where $I_t(x,y)$ and $I_{t_0}(x,y)$ denote the reconstructed images for time t and the time at beginning of the experiment t_0 and $T_{t_0}(x,y)$ denotes the initial temperature distribution at time t_0. If we further assume equal temperature of T_0 throughout the sample at the beginning of the experiment we can further simplify Eq.(3.2) to

$$T_t(x,y) \approx \frac{I_t(x,y)}{I_{t_0}(x,y)} \times T_0 \tag{3.3}$$

For T_0 a value of 25°C was chosen, which corresponds to room temperature as measured by the thermocouples used during the experiments. It is known that this linear relationship

ceases to exist once a critical temperature is reached and the irreversible process of coagulation is induced [51]. However, it is already sufficient to measure the temperature in the native tissue until the critical temperature is reached. The progression of the lesion boundary could then be followed, even though temperature could only be measured reliably on the native side of the lesion boundary.

3.6.3 Results

Fig.3.14 shows reconstructed images as well as the resulting temperature map obtained for an ablation sequence corresponding to the lesion shown in Fig3.13(a). The resulting temperature map for the last frame of the ablation sequence ($t = 60s$) is depicted in Fig.3.14(c).

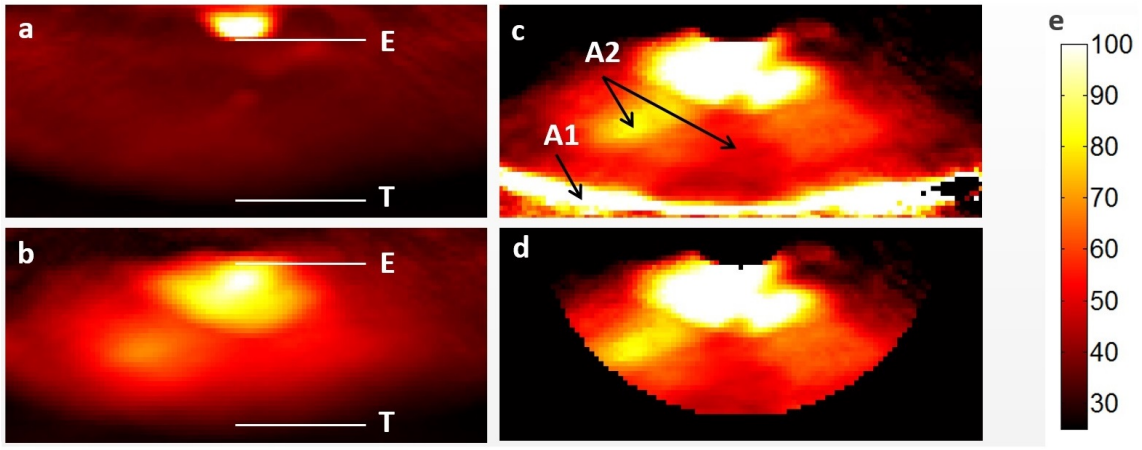

Figure 3.14: temperature map obtained for an ablation sequence corresponding to the lesion shown in Fig3.13(a). (a) Reconstructed image $I_{t_0}(x,y)$, with E denoting the tip of the ablation electrode and T denoting the bottom tissue surface. (b) reconstructed image $I_{t=60s}(x,y)$, again E denoting the tip of the ablation electrode and T denoting the bottom tissue surface. (c) resulting temperature map $T_{t=60s}(x,y)$, with $A1$ and $A2$ showing artefacts generated by the temperature mapping algorithm. (d) temperature map cropped to hide artifact $A1$. (e) corresponding temperature scale in °C.

The very strong response underneath the tissue surface, marked by $A1$, is clearly an artefact and possibly due to the fact that the reconstruction algorithm is not quantitative enough. Apparently the strong increase in signal strength within the heated tissue slab

leads to an increase in the background intensity. This ”spillover” effect might be due to a lack of projections or other reasons related to data processing and reconstruction. Since the artefact A1 is found outside of the tissue slab it can be easily removed by cropping the reconstructed temperature map, as shown in Fig.3.14(d), which is only suggested as a temporary solution. Similar spillover effects can be observed in the beginning of many ablations, when the strong response of the electrode creates streaking artefacts in neighbouring regions. The intensity of these streaking artefacts can be reduced by choosing a lower cut-off frequency of the low-pass filter, e.g. 3MHz instead of 5MHz. However, this might only be a cosmetic and merely qualitative improvement.
A more critical artefact is highlighted by $A2$. There is a significant difference in the temperature measurements of about 30°C between the locations marked by the arrowheads. Given the radial symmetry of tissue damage, as can be clearly observed in Fig.3.13(a), such a high difference in the measured temperatures seems very unrealistic and is therefore likely the result of a reconstruction artefact in the corresponding images.

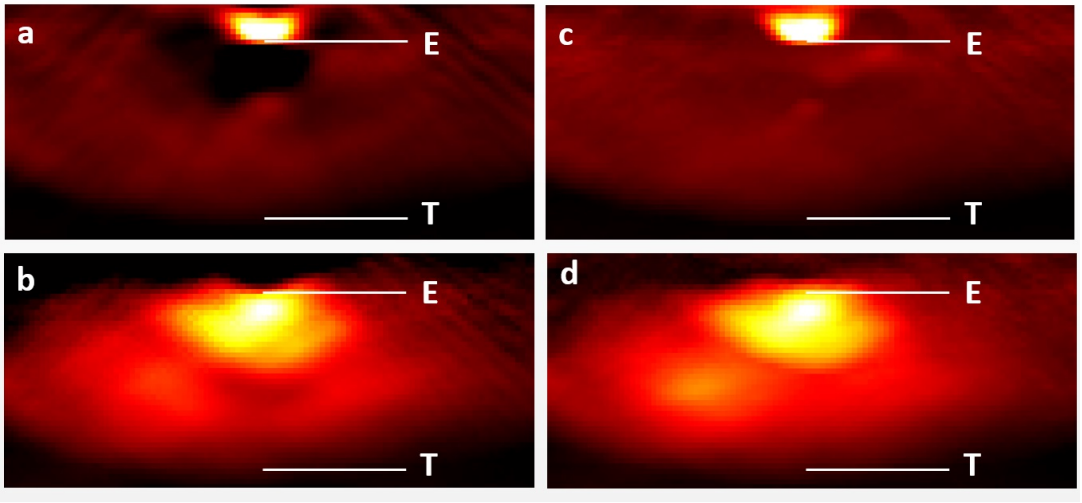

Figure 3.15: (a) Reconstructed image $I_{t_0}(x,y)$ obtained from cross-section through the reconstructed three-dimensional volume. (b) Reconstructed image $I_{t=60s}(x,y)$ obtained from cross-section through the reconstructed three-dimensional volume. (c) Reconstructed image $I_{t_0}(x,y)$ obtained from maximum intensity projection. (d) Reconstructed image $I_{t=60s}(x,y)$ obtained from maximum intensity projection.

It has to be noted that the images are maximum intensity projections of the reconstructed three-dimensional volume. As can be seen in Fig.3.15(a-b), images obtained from a cross-

section through the reconstructed volume differ significantly from the corresponding maximum amplitude projections shown in Fig.3.15(c-d). Apparently, strong absorbers in the reconstructed cross-sections, such as the electrode in Fig.3.15(a), are surrounded by darker regions of considerably lower or even negative signal. Maximum amplitude projections can hide these dark shadows, since negative regions are not projected, however they do not yield quantitative representations and distort the radial symmetry of temperature distribution. Therefore, for future work it is recommended to only use cross-sectional images from the reconstructed 3D volume for temperature map calculations. Then, however, the model based reconstruction algorithm has to be improved to yield a more quantitative representation of the initial pressure distribution, characterized by the product of Grueneisen parameter, optical absorption and fluence.

Figs.3.16 and 3.17 show the temperature maps calculated for the entire ablation sequence of the two lesions depicted in Fig3.13(a) and Fig3.13(b). For both cases the 5th iteration of the model-based algorithm was used. Reconstructions were performed at different cut-off frequencies for the low-pass filter, 3MHz in Fig.3.16 and 5MHz in Fig.3.17.

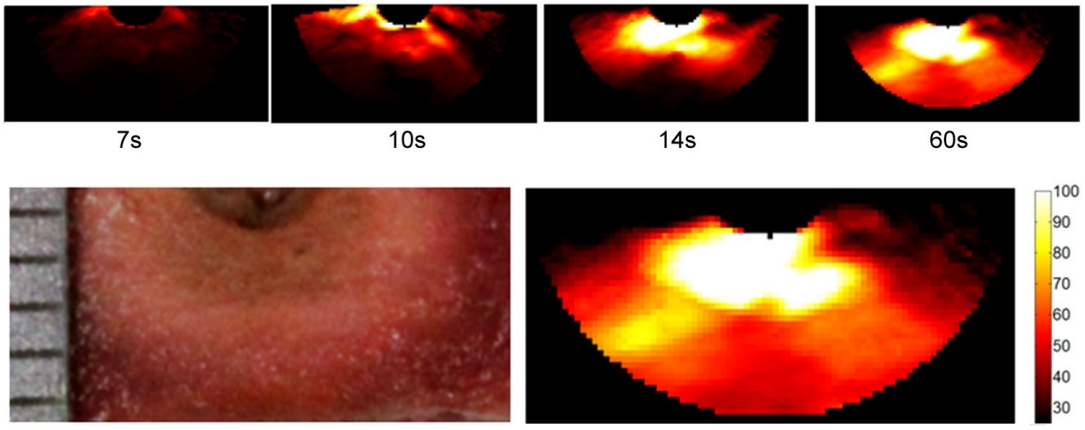

Figure 3.16: Temperature maps of the ablation sequence for the tissue slab depicted in Fig.3.13(a); instances of t=7s, t=10s, t=14s and t=60s shown

A comparison of the temperature maps shows much higher temperatures in the bottom part of the tissue slab in Fig.3.16 compared to Fig.3.17.

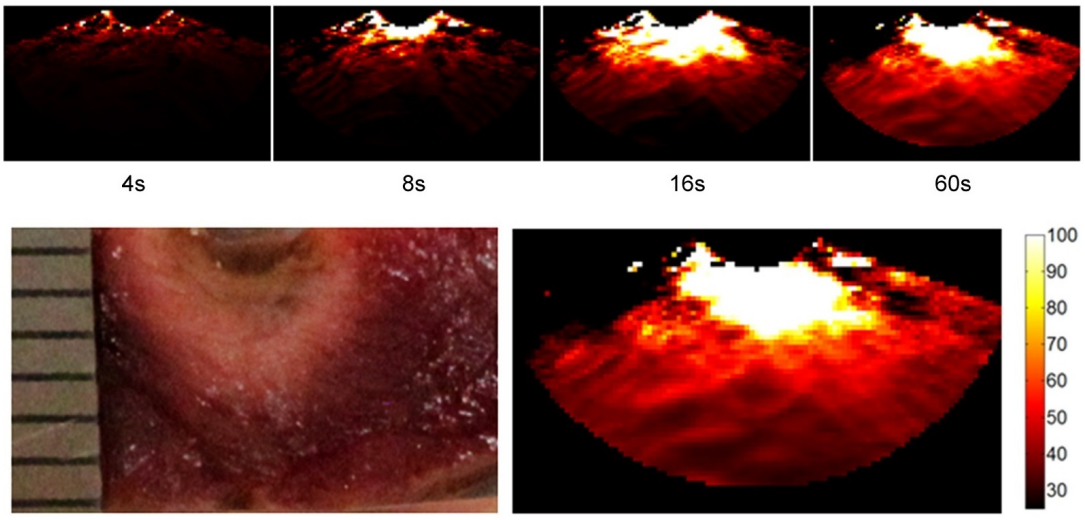

Figure 3.17: Temperature maps of the ablation sequence for the tissue slab depicted in Fig.3.13(b); instances of t=4s, t=8s, t=16s and t=60s shown

Since the contour of discolouration almost reaches the bottom edge of the tissue sample in Fig.3.16, high temperatures of close to 60°C can be expected to appear in the corresponding region in the temperature map. Whether this is the case is difficult to assess, due to the artefacts highlighted in Fig.3.14(c). In Fig.3.17, however, the contour of discolouration stops about 2-3mm above the bottom edge of the tissue slab. The depth of the contour of discolouration seems to correspond well with the 60°C iso-contour in the temperature map, although the temperature map needs to be smoothed for better comparison.

3.6.4 Discussion and conclusion

Although quantitative assessment of tissue temperature during ablation is not yet possible due to several artefacts corrupting the temperature maps, the proposed method could eventually provide measurements of the depth of the entire lesion, as suggested in Fig.3.17. To this end, however, the imaging artefacts observed in this study have to be eliminated and a more quantitative reconstruction algorithm needs to be employed. For future work, several steps can be taken to create more quantitative reconstructions:

- Account for frequency response (i.e. deconvolution with electrical impulse response):

it is known that the current electrical impulse response is not correct and leads to a loss of low frequencies when signals are deconvolved. As a result the temperature gradient is barely visible. Therefore, in this study, the frequency response was not accounted for. Future work has to focus on finding a more realistic frequency response. Computing the impulse response involves the integration of the time-resolved signal obtained from a micro-sphere. For this purpose, a 50µm micro-sphere was used to obtain the impulse response. Using such a small micro-sphere leads to realistic values of the estimated frequency response for high frequencies of several MHz, but causes a misrepresentation of the response for low frequencies of less than ca. 1MHz. Therefore using a much bigger micro-sphere of 200 or even 500µm might be advisable to obtain a reliable response for low frequencies. This requires further carefully planned experiments.

- Account for spatial impulse response
  The model-based algorithm assumes point detectors, the detectors of the cup-shaped detector array however have an element size of 3×3 mm^2. Accounting for the spatial impulse response might further increase reconstruction quality.

- Increase number of projections
  only 256 projections were used to reconstruct a volume of 1 million voxels ($100 \times 100 \times 100$). This translates into a severely under determined set of equations which is solved iteratively in the model-based code. The lack of information causes artefacts to appear in the reconstructed images. Reconstructing with a lower resolution ($50 \times 50 \times 50$) and subsequent interpolation of the temperature map might reduce artefacts. Another approach could be to interpolate between the detectors, i.e. to create "'virtual"' detectors between adjacent detectors by interpolating detector positions. Time-resolved signals will be interpolated correspondingly and the result assigned to the virtual detector.

- Non-negative reconstruction
  A non-negative model-based reconstruction developed at the institute could help to improve reconstructions and remove negative regions (dark shadows).

- Account for movement
  The method proposed for computing temperature maps further assumes the lack of any movement in the reconstructed tissue sample during the ablation process. This movement might be due to a non-negligible change in speed of sound during heating

or to actual physical movement of the tissue slab. Either way, movement needs to be detected on a pixel per pixel basis (e.g. using a correlation based tracking algorithm) and compensated for by shifting or transforming images before creating the temperature map

Future studies should consider validation of the generated temperature maps by measurements performed at various positions. Measuring temperature underneath the tissue slab, as done previously (see section 3.5.2), is certainly advisable. If estimating temperature along a centerline from the electrode tip to the bottom of the tissue slab is desired, another temperature measurement could be performed by a thermocouple placed inside the electrode, with the tip of the thermocouple slightly extruding into the heated tissue. Placing the thermocouple in this position might lead to a more accurate temperature measurement than placing it next to the electrode, as done previously.
Simulations are another promising way of validating temperature maps. Using Finite Element software (e.g. Comsol) to simulate heat transfer during RF ablation can be insightful. For accurate assessment of the optoacoustic temperature maps, the biophysical model used in the simulation needs to account for various parameters such as electrode insertion depth and cooling effects of the water volume surrounding the electrode.
As noted previously, a direct proportional relationship between temperature and optoacoustic signal strength was assumed within this first study. For more accurate temperature mapping in future studies both constants in Eq.(3.2) need to be determined. To this end, temperature needs to be measured in a reference position at two time instants during the heating process before the onset of coagulation. A suitable reference position might be inside the tip of the electrode where a thermocouple might be placed for future studies.

3.7 Summary and outlook

In order to investigate how Optoacoustics can be used for real-time monitoring of RF catheter ablation, a compact integrated catheter was designed, assembled and tested, comprising an electrode for RF current delivery, optical fibers for optoacoustic signal generation and a single compact, needle-like hydrophone for optoacoustic signal detection (section 3.4). The advantage of this particular design was to enable intra-cardiac monitoring of catheter ablation by using only a single ultrasonic detector resulting in high sensitivity and small size. Experiments, however, have shown that integrating all parts in

a single catheter probe leads to several technical problems such as acoustic reverberations and burning of the optical fibers which render the catheter probe incapable of reliably monitoring ablation in clinical treatments.
As a consequence, it is recommended to decouple electric current delivery and optical illumination from the detection of the optoacoustic signals, which can technically also be performed at distances of many centimeters, or in fact, even outside the patients body. A proof-of-concept study was therefore conducted to evaluate how a multi-element detector array can be used to enable three-dimensional monitoring of the RF ablation process (section 3.5). Results were very promising, showing that real-time monitoring of lesion progression can be achieved with Optoacoustics based on monitoring the size of the strongly coagulated tissue volume in the optoacoustic images. The study also showed strong sensitivity of the optoacoustic image intensity to the temperature profile within the heated tissue volume. A further preliminary study was therefore conducted on the same data set (section 3.6) in order to evaluate an algorithm designed to monitor the temperature gradient within the heated tissue volume based on changes in the intensity of the optoacoustic images. The study showed great potential for determining a precise temperature gradient and thereby estimating the entire lesion volume during clinical treatments. However, in order to realize reliable and indisputable temperature measurement several reconstruction artifacts identified in this study need to be eliminated in future work.

4 Conclusion and Outlook

4.1 Conclusion

The optoacoustic techniques developed and tested in this work, as shown in chapters 2 and 3, have proven to be capable of providing valuable real-time feedback on critical process parameters during ablation treatments. Optoacoustics was shown to be very sensitive to changes in tissue composition and structure that occur during the biophysical processes coagulation, carbonization and tissue removal. More specifically, it was shown that the onset of carbonization, the cutting efficiency of the laser beam as well as the three-dimensional incision profile can be precisely measured using optoacoustic monitoring. As a result, current disadvantages of laser ablation treatments such as the risk of collateral damage to critical tissues, either by excessive heating or due to the lack of haptic feedback, could be overcome by utilizing optoacoustic real-time feedback. Moreover, it was observed that optoacoustic images show excellent contrast between highly coagulated and native tissue and are very sensitive to the temperature gradient within the heated tissue volume. Therefore, Optoacoustics can be utilized for real-time monitoring of lesion progression and estimation of lesion size during RF ablation treatments. Further, widely applied ablation treatments such as high intensity focused ultrasound or microwave ablation are known to generate similar lesions of coagulated tissue, and might therefore also benefit from an optoacoustic monitoring technique, if the method is adapted to the specific requirements of the particular clinical treatment.

4.2 Outlook

Besides showing successful *ex vivo* studies to evaluate the feasibility of Optoacoustic monitoring of ablation treatments in medicine, this work has also provided detailed speci-

fications and recommendations for the development of sensor prototypes that can be used in clinical setups. For monitoring the three-dimensional incision profile during laser ablation treatments, a detailed analysis was performed to define the geometry of the detector array that is required for precise feedback during the ablation process. With respect to monitoring lesion progression during RF cardiac ablation, the experimental *ex vivo* studies performed in this work yielded various insights for developing algorithms as well as sensor prototypes that can overcome current limitations and can be used in clinical ablation procedures.

Acknowledgements

First of all, I would like to express my deepest thanks to my supervisor Prof. Dr. Daniel Razansky for providing me the exciting opportunity to develop novel technology at the forefront of Biomedial Imaging and for giving me the freedom necessary for creative ideas while guiding me with his deep knowledge in Optoacoustic Imaging and Sensing. Furthermore, I would like to thank Prof. Dr. Vasilis Ntziachristos for supporting me as a Ph.D. student and providing me with the rich resources and the creative, interdisciplinary environment at his institute IBMI.

While working on my research project at IBMI, I received a great deal of help from people in the institute. I would like to thank all the researchers in Prof. Razansky's team, especially Dr. Genny A. Pang and Dr. Xose Luís Deán-Ben for their insightful suggestions during countless scientific discussions and their contribution to critical experiments within my research. I also very much enjoyed and benefited from technical discussions with Dr. Hector Estrada, Dr. Andreas Buehler, Alexander Dima, Dr. Jérôme Gâteau and Dr. Miguel Ángel Araque Caballero. I would also like to express my thanks to the technical staff at IBMI, Sarah Glasl, Florian Jurgeleit and Uwe Klemm for providing me with their valuable technical help in the laboratory.

Finally, I would like to thank my family for their immense support and encouragements.

List of Figures

Bibliography

[1] H. Schwarzmaier and F. Eickmeyer, "Basic principles of laser induced interstitial thermotherapy in brain tumors," Medical Laser Application, vol. 17, no. 2, pp. 147–158, 2002.

[2] A. Vogel and V. Venugopalan, "Mechanisms of pulsed laser ablation of biological tissues.," Chemical reviews, vol. 103, no. 2, pp. 577–644, 2003.

[3] G. ter Haar and C. Coussios, "High intensity focused ultrasound: physical principles and devices," International Journal of Hyperthermia, vol. 23, no. 2, pp. 89–104, 2007.

[4] Y. Ni, S. Mulier, Y. Miao, L. Michel, and G. Marchal, "A review of the general aspects of radiofrequency ablation," Abdominal imaging, vol. 30, no. 4, pp. 381–400, 2005.

[5] C. Simon, D. Dupuy, and W. Mayo-Smith, "Microwave ablation: principles and applications," Radiographics, vol. 25, no. 1, pp. 69–84, 2005.

[6] F. Morady, "Radio-frequency ablation as treatment for cardiac arrhythmias," The New England Journal of Medicine, vol. 340, pp. 534–544, 1999.

[7] D. Saldanha and V. Khiatani, "Current tumor ablation technologies: basic science and device review," Seminars in Interventional Radiology, vol. 27, no. 3, pp. 247–254, 2010.

[8] S. Goldberg, "Radiofrequency tumor ablation: principles and techniques," European Journal of Ultrasound, vol. 13, no. 2, pp. 129–147, 2001.

[9] I. Van der Ploeg and S. van Esser, "Radiofrequency ablation for breast cancer: a review of the literature," European Journal of Surgical Oncology, vol. 33, no. 6, pp. 673–677, 2007.

[10] P. Wust, B. Hildebrandt, and G. Sreenivasa, "Hyperthermia in combined treatment of cancer," The lancet oncology, vol. 3, no. 8, pp. 487–497, 2002.

[11] S. Stübinger, "Advances in bone surgery: the Er: YAG laser in oral surgery and implant dentistry," Clinical, Cosmetic and Investigational Dentistry, vol. 2010, no. 2, pp. 47–62, 2010.

[12] J. M. White, H. E. Goodis, and C. L. Rose, "Use of the pulsed Nd:YAG laser for intraoral soft tissue surgery.," Lasers in surgery and medicine, vol. 11, pp. 455–61, Jan. 1991.

[13] S. Parker, "Lasers and soft tissue: 'loose' soft tissue surgery.," British dental journal, vol. 202, no. 4, pp. 185–91, 2007.

[14] M. Ivanenko, M. Werner, S. Afilal, M. Klasing, and P. Hering, "Ablation of hard bone tissue with pulsed CO2 lasers," Medical Laser Application, vol. 20, no. 1, pp. 13–23, 2005.

[15] J. White, S. Chaudhry, and J. Kudler, "Nd: YAG and CO2 laser therapy of oral mucosal lesions," Journal of Clinical Laser Medicine and Surgery, vol. 16, no. 6, pp. 299–304, 1998.

[16] N. Dana, L. Di Biase, A. Natale, S. Emelianov, and R. Bouchard, "In vitro photoacoustic visualization of myocardial ablation lesions," Heart Rhythm, vol. 11, pp. 150–157, Sept. 2014.

[17] F. Neukam and F. Stelzle, "Laser tumor treatment in oral and maxillofacial surgery," Physics Procedia, vol. 5, pp. 91–100, 2010.

[18] F. Stelzle, K. Tangermann-Gerk, W. Adler, A. Zam, M. Schmidt, A. Douplik, and E. Nkenke, "Diffuse reflectance spectroscopy for optical soft tissue differentiation as remote feedback control for tissue-specific laser surgery.," Lasers in surgery and medicine, vol. 42, pp. 319–325, Apr. 2010.

[19] H. Cui and X. Yang, "Real-time monitoring of high-intensity focused ultrasound ablations with photoacoustic technique: An in vitro study," Medical Physics, vol. 38, no. 10, p. 5345, 2011.

[20] S. Sapareto and W. Dewey, "Thermal dose determination in cancer therapy," International Journal of Radiation Oncology, Biology, Physics, vol. 10, no. 6, pp. 787–800, 1984.

[21] C. Li and L. V. Wang, "Photoacoustic tomography and sensing in biomedicine.," Physics in medicine and biology, vol. 54, no. 19, pp. 59–97, 2009.

[22] V. Ntziachristos and D. Razansky, "Molecular imaging by means of multispectral optoacoustic tomography (MSOT)," Chemical reviews, vol. 110, no. 5, pp. 2783–2794, 2010.

[23] S. a. Ermilov, T. Khamapirad, A. Conjusteau, M. H. Leonard, R. Lacewell, K. Mehta, T. Miller, and A. a. Oraevsky, "Laser optoacoustic imaging system for detection of breast cancer.," Journal of biomedical optics, vol. 14, no. 2, p. 024007, 2010.

[24] R. Siphanto and K. Thumma, "Serial noninvasive photoacoustic imaging of neovascularization in tumor angiogenesis," Optics Express, vol. 13, no. 1, pp. 89–95, 2005.

[25] G. Ku, X. Wang, X. Xie, G. Stoica, and L. Wang, "Imaging of tumor angiogenesis in rat brains in vivo by photoacoustic tomography," Applied optics, vol. 44, no. 5, pp. 770–775, 2005.

[26] H. Zhang, K. Maslov, M. Li, G. Stoica, and L. Wang, "In vivo volumetric imaging of subcutaneous microvasculature by photoacoustic microscopy," Optics Express, vol. 14, no. 20, pp. 9317–9323, 2006.

[27] X. Wang, Y. Pang, G. Ku, and X. Xie, "Noninvasive laser-induced photoacoustic tomography for structural and functional in vivo imaging of the brain," Nature biotechnology, vol. 21, pp. 803 – 806, 2003.

[28] D. Razansky, C. Vinegoni, and V. Ntziachristos, "Multispectral photoacoustic imaging of fluorochromes in small animals," Optics letters, vol. 32, no. 19, pp. 2891–2893, 2007.

[29] D. Razansky, M. Distel, C. Vinegoni, and R. Ma, "Multispectral opto-acoustic tomography of deep-seated fluorescent proteins in vivo," Nature photonics, vol. 3, pp. 412 – 417, 2009.

[30] N. Lozano, K. Kostarelos, and V. Ntziachristos, "Liposome-Gold Nanorod Hybrids for High-Resolution Visualization Deep in Tissues," Journal of the American Chemical Society, vol. 134, no. 32, pp. 13256–13258, 2012.

[31] A. Taruttis, S. Morscher, and N. Burton, "Fast multispectral optoacoustic tomography (MSOT) for dynamic imaging of pharmacokinetics and biodistribution in multiple organs," PloS one, 2012.

[32] D. Razansky and N. Deliolanis, "Deep tissue optical and optoacoustic molecular imaging technologies for pre-clinical research and drug discovery," Current Pharmaceutical Biotechnology, vol. 13, no. 4, pp. 504–522, 2012.

[33] R. Agah, a. H. Gandjbakhche, M. Motamedi, R. Nossal, and R. F. Bonner, "Dynamics of temperature dependent optical properties of tissue: dependence on thermally induced alteration.," IEEE transactions on bio-medical engineering, vol. 43, pp. 839–46, Aug. 1996.

[34] W. Lin, C. Buttemere, and A. Mahadevan-Jansen, "Effect of thermal damage on the in vitro optical and fluorescence characteristics of liver tissues," IEEE Journal of Selected Topics in Quantum Electronics, vol. 9, pp. 162–170, Mar. 2003.

[35] P. V. Chitnis, H.-P. Brecht, R. Su, and A. A. Oraevsky, "Feasibility of optoacoustic visualization of high-intensity focused ultrasound-induced thermal lesions in live tissue," Journal of Biomedical Optics, vol. 15, p. 021313, Mar. 2010.

[36] I. Apitz and A. Vogel, "Material ejection in nanosecond Er:YAG laser ablation of water, liver, and skin," Applied Physics A, vol. 81, pp. 329–338, Mar. 2005.

[37] R. O. Esenaliev, A. A. Oraevsky, V. S. Letokhov, A. A. Karabutov, and T. V. Malinsky, "Studies of acoustical and shock waves in the pulsed laser ablation of biotissue.," Lasers in surgery and medicine, vol. 13, pp. 470–84, Jan. 1993.

[38] A. Tuchmann, P. Bauer, H. Plenk, and O. Braun, "Comparative study of conventional scalpel and CO2-laser in experimental tumor surgery," Research in experimental medicine, vol. 186, pp. 375–86, Jan. 1986.

[39] R. J. Lanzafame, D. W. Rogers, J. O. Naim, H. R. Herrera, C. DeFranco, and J. R. Hinshaw, "The effect of CO2 laser excision on local tumor recurrence.," Lasers in surgery and medicine, vol. 6, pp. 103–5, Jan. 1986.

[40] M. A. Pogrel, K. J. McCracken, and T. E. Daniels, "Histologic evaluation of the width of soft tissue necrosis adjacent to carbon dioxide laser incisions.," Oral surgery, oral medicine, and oral pathology, vol. 70, pp. 564–8, Nov. 1990.

[41] A. V. Shakhov, A. B. Terentjeva, V. A. Kamensky, L. B. Snopova, V. M. Gelikonov, F. I. Feldchtein, and A. M. Sergeev, "Optical coherence tomography monitoring for laser surgery of laryngeal carcinoma.," Journal of surgical oncology, vol. 77, pp. 253–8, Aug. 2001.

[42] J. T. Walsh, T. J. Flotte, and T. F. Deutsch, "Er:YAG laser ablation of tissue: effect of pulse duration and tissue type on thermal damage.," Lasers in surgery and medicine, vol. 9, pp. 314–26, Jan. 1989.

[43] D. Das, S. Reed, P. Klokkevold, and B. Wu, "A high-throughput comparative characterization of laser-induced soft tissue damage using 3D digital microscopy," Lasers in Medical Science, vol. 28, pp. 657–668, June 2012.

[44] R. W. Ryan, T. Wolf, R. F. Spetzler, S. W. Coons, Y. Fink, and M. C. Preul, "Application of a flexible CO(2) laser fiber for neurosurgery: laser-tissue interactions.," Journal of neurosurgery, vol. 112, pp. 434–43, Feb. 2010.

[45] K. Nahen and A. Vogel, "Investigations on acoustic online monitoring of IR laser ablation of burned skin," Lasers in surgery and medicine, vol. 25, no. 1, pp. 69–78, 1999.

[46] S. Rupprecht, K. Tangermann-Gerk, J. Wiltfang, F. W. Neukam, and A. Schlegel, "Sensor-based laser ablation for tissue specific cutting: an experimental study.," Lasers in medical science, vol. 19, pp. 81–8, Jan. 2004.

[47] F. Stelzle, A. Zam, W. Adler, K. Tangermann-Gerk, A. Douplik, E. Nkenke, and M. Schmidt, "Optical nerve detection by diffuse reflectance spectroscopy for feedback controlled oral and maxillofacial laser surgery.," Journal of translational medicine, vol. 9, p. 20, Jan. 2011.

[48] A. Douplik, A. Zam, R. Hohenstein, A. Kalitzeos, E. Nkenke, and F. Stelzle, "Limitations of cancer margin delineation by means of autofluorescence imaging under conditions of laser surgery," Journal of Innovative Optical Health Sciences, vol. 03, no. 01, pp. 45–51, 2010.

[49] L. Wang, Photoacoustic imaging and spectroscopy. Baco Raton, Florida: CRC Press, 1 ed., 2009.

[50] D. Razansky, "Multi-Spectral Optoacoustic Tomography - Volumetric Color Hearing in Real Time," IEEE Journal of Selected Topics in Quantum Electronics, 2012.

[51] K. V. Larin, I. V. Larina, and R. O. Esenaliev, "Monitoring of tissue coagulation during thermotherapy using optoacoustic technique," Journal of Physics D: Applied Physics, vol. 38, pp. 2645–2653, Aug. 2005.

[52] E. Bay, A. Douplik, and D. Razansky, "Optoacoustic monitoring of cutting efficiency and thermal damage during laser ablation," Lasers in Medical Science, vol. 29, pp. 1029–1035, Oct. 2014.

[53] H. K. Park, D. Kim, C. P. Grigoropoulos, and A. C. Tam, "Pressure generation and measurement in the rapid vaporization of water on a pulsed-laser-heated surface," Journal of Applied Physics, vol. 80, no. 7, p. 4072, 1996.

[54] G. I. Jallo, K. F. Kothbauer, and F. J. Epstein, "Contact laser microsurgery," Child's nervous system : ChNS : official journal of the International Society for Pediatric Neurosurgery, vol. 18, pp. 333–6, July 2002.

[55] D. C. Jeong, P. S. Tsai, and D. Kleinfeld, "Prospect for feedback guided surgery with ultra-short pulsed laser light.," Current opinion in neurobiology, vol. 22, pp. 24–33, Feb. 2012.

[56] B.-M. Kim, M. Feit, A. Rubenchik, B. Mammini, and L. Da Silva, "Optical feedback signal for ultrashort laser pulse ablation of tissue," Applied Surface Science, vol. 127-129, pp. 857–862, May 1998.

[57] S. Stopp, D. Svejdar, E. von Kienlin, H. Deppe, and T. C. Lueth, "A new approach for creating defined geometries by navigated laser ablation based on volumetric 3-D data.," IEEE transactions on bio-medical engineering, vol. 55, pp. 1872–80, July 2008.

[58] L. A. Kahrs, J. Burgner, T. Klenzner, J. Raczkowsky, J. Schipper, and H. Wörn, "Planning and simulation of microsurgical laser bone ablation.," International journal of computer assisted radiology and surgery, vol. 5, pp. 155–62, Mar. 2010.

[59] B. Y. C. Leung, P. J. L. Webster, J. M. Fraser, and V. X. D. Yang, "Real-time guidance of thermal and ultrashort pulsed laser ablation in hard tissue using inline coherent imaging.," Lasers in surgery and medicine, vol. 44, pp. 249–56, Mar. 2012.

[60] D. Stern, W. Z. Lin, C. a. Puliafito, and J. G. Fujimoto, "Femtosecond optical ranging of corneal incision depth.," Investigative ophthalmology & visual science, vol. 30, pp. 99–104, Jan. 1989.

[61] J. T. J. Walsh and T. F. Deutsch, "Measurement of Er: YAG Laser Ablation Plume Dynamics," Appl. Phys. B, vol. 52, pp. 217–224, 1991.

[62] T. Juhasz, X. H. Hu, L. Turi, and Z. Bor, "Dynamics of shock waves and cavitation bubbles generated by picosecond laser pulses in corneal tissue and water.," Lasers in surgery and medicine, vol. 15, pp. 91–8, Jan. 1994.

[63] T. M. Buzug and J. Bongartz, "Navigation Concept for Image-Guided Laser Surgery," Proceedings of the International IEEE Conference on Mechatronics & Robotics, pp. 1403–08, 2004.

[64] E. Bay, X. L. Deán-Ben, G. A. Pang, A. Douplik, and D. Razansky, "Real-time monitoring of incision profile during laser surgery using shock wave detection," Journal of Biophotonics, vol. 8, pp. 102–111, Jan. 2015.

[65] X. L. Deán-Ben and D. Razansky, "Portable spherical array probe for volumetric real-time optoacoustic imaging at centimeter-scale depths," Optics Express, vol. 21, pp. 28062–71, Nov. 2013.

[66] X. L. Deán-Ben, A. Oezbek, and D. Razansky, "Volumetric real-time tracking of peripheral human vasculature with GPU-accelerated three-dimensional optoacoustic tomography," IEEE transactions on medical imaging, vol. 32, no. 11, pp. 2050–55, 2013.

[67] W. Leung and A. Tam, "Noncontact monitoring of laser ablation using a miniature piezoelectric probe to detect photoacoustic pulses in air," Applied physics letters, vol. 60, no. 1, pp. 23–25, 1992.

[68] P. L. G. Ventzek, R. M. Gilgenbach, D. M. Heffelfinger, and J. A. Sell, "Laser-beam deflection measurements and modeling of pulsed laser ablation rate and near-surface plume densities in vacuum," Journal of Applied Physics, vol. 70, pp. 587–593, 1991.

[69] S. Strgar and J. Možina, "An optodynamic determination of the depth of laser-drilled holes by the simultaneous detection of ultrasonic waves in the air and in the workpiece," in Ultrasonics, vol. 40, pp. 791–795, May 2002.

[70] A. Gachagan and G. Hayward, "Characterization of air-coupled transducers," IEEE transactions on ultrasonics, ferroelectrics, and frequency control, vol. 43, no. 4, pp. 678 – 689, 1996.

[71] M. C. Bhardwaj, "Evolution of piezoelectric transducers to full scale non-contact ultrasonic analysis mode," in World Conference on Non-Destructive Testing, 2004.

[72] T. Álvarez Arenas, "Acoustic impedance matching of piezoelectric transducers to the air," IEEE transactions on ultrasonics, ferroelectrics, and frequency control, vol. 51, no. 5, pp. 624–633, 2004.

[73] D. Lloyd-Jones, R. J. Adams, T. M. Brown, M. Carnethon, S. Dai, G. De Simone, T. B. Ferguson, E. Ford, K. Furie, C. Gillespie, A. Go, K. Greenlund, N. Haase, S. Hailpern, P. M. Ho, V. Howard, B. Kissela, S. Kittner, D. Lackland, L. Lisabeth, A. Marelli, M. M. McDermott, J. Meigs, D. Mozaffarian, M. Mussolino, G. Nichol, V. L. Roger, W. Rosamond, R. Sacco, P. Sorlie, V. L. Roger, T. Thom, S. Wasserthiel-Smoller, N. D. Wong, and J. Wylie-Rosett, "Heart disease and stroke statistics-2010 update: a report from the American Heart Association.," Circulation, vol. 121, 2010.

[74] C. M. Tracy, M. Akhtar, J. P. Dimarco, D. L. Packer, H. H, W. L. Winters, J. L. Achord, A. W. Boone, J. W. Hirshfeld, B. H. Lorell, G. P. Rodgers, and H. H. Weitz, "ACC / AHA Clinical Competence Statement American College of Cardiology / American Heart Association Clinical Competence Statement on Invasive," Journal of the American College of Cardiology, vol. 36, no. 5, pp. 1725–1736, 2010.

[75] A. Verma and A. Natale, "Should atrial fibrillation ablation be considered first-line therapy for some patients? Why atrial fibrillation ablation should be considered first-line therapy for some patients.," Circulation, vol. 112, pp. 1214–22, Aug. 2005.

[76] L. M. Epstein, M. A. Mitchell, T. W. Smith, and D. E. Haines, "Comparative study of fluoroscopy and intracardiac echocardiographic guidance for the creation of linear atrial lesions.," Circulation, vol. 98, pp. 1796–801, Oct. 1998.

[77] P. M. Kistler, K. Rajappan, M. Jahngir, M. J. Earley, S. Harris, D. Abrams, D. Gupta, R. Liew, S. Ellis, S. C. Sporton, and R. J. Schilling, "The impact of CT image integration into an electroanatomic mapping system on clinical outcomes of catheter ablation of atrial fibrillation.," Journal of cardiovascular electrophysiology, vol. 17, pp. 1093–101, Oct. 2006.

[78] D. Stephens, J. Cannata, and R. Liu, "Multifunctional catheters combining intracardiac ultrasound imaging and electrophysiology sensing," Ultrasonics, Ferroelectrics and Frequency Control, IEEE Transactions on, vol. 55, no. 7, pp. 1570–1581, 2008.

[79] R. Cappato, H. Calkins, S.-A. Chen, W. Davies, Y. Iesaka, J. Kalman, Y.-H. Kim, G. Klein, A. Natale, D. Packer, A. Skanes, F. Ambrogi, and E. Biganzoli, "Updated worldwide survey on the methods, efficacy, and safety of catheter ablation for human atrial fibrillation.," Circulation. Arrhythmia and electrophysiology, vol. 3, pp. 32–8, Feb. 2010.

[80] G. R. Vergara, S. Vijayakumar, E. G. Kholmovski, J. J. E. Blauer, M. a. Guttman, C. Gloschat, G. Payne, K. Vij, N. W. Akoum, M. Daccarett, C. J. McGann, R. S. Macleod, and N. F. Marrouche, "Real-time magnetic resonance imaging-guided radiofrequency atrial ablation and visualization of lesion formation at 3 Tesla.," Heart rhythm : the official journal of the Heart Rhythm Society, vol. 8, pp. 295–303, Feb. 2011.

[81] M. Wright, E. Harks, S. Deladi, and F. Suijver, "Real-time lesion assessment using a novel combined ultrasound and radiofrequency ablation catheter," Heart Rhythm, vol. 8, no. 2, pp. 304–312, 2011.

[82] B. J. Fahey, K. R. Nightingale, S. A. McAleavey, M. L. Palmeri, P. D. Wolf, and G. E. Trahey, "Acoustic radiation force impulse imaging of myocardial radiofrequency ablation: initial in vivo results," IEEE Trans Ultrason Ferroelectr Freq Control, vol. 52, no. 4, pp. 631–641, 2005.

[83] S. A. Eyerly, T. D. Bahnson, J. I. Koontz, D. P. Bradway, D. M. Dumont, G. E. Trahey, and P. D. Wolf, "Intracardiac acoustic radiation force impulse imaging: A novel imaging method for intraprocedural evaluation of radiofrequency ablation lesions," Heart Rhythm, vol. 9, no. 11, pp. 1855–1862, 2012.

[84] C. H. Seo, D. N. Stephens, J. Cannata, A. Dentinger, F. Lin, S. Park, D. Wildes, K. E. Thomenius, P. Chen, T. Nguyen, A. De La Rama, J. S. Jeong, A. Mahajan, K. Shivkumar, A. Nikoozadeh, O. Oralkan, U. Truong, D. J. Sahn, P. T. Khuri-Yakub, and M. O'Donnell, "The feasibility of using thermal strain imaging to regulate energy delivery during intracardiac radio-frequency ablation," IEEE Transactions on Ultrasonics, Ferroelectrics, and Frequency Control, vol. 58, no. 7, pp. 1406–1417, 2011.

[85] D. Stephens, "First In Vivo Use of a Capacitive Micromachined Ultrasound Transducer ArrayâBased Imaging and Ablation Catheter," Journal of Ultrasound in Medicine, vol. 31, no. 2, pp. 247–256, 2012.

[86] C. P. Fleming, K. J. Quan, H. Wang, G. Amit, and A. M. Rollins, "In vitro characterization of cardiac radiofrequency ablation lesions using optical coherence tomography.," Optics express, vol. 18, pp. 3079–92, Feb. 2010.

[87] C. P. Fleming, N. Rosenthal, and A. M. Rollins, "First in vivo Real-Time Imaging of Endocardial Radiofrequency Ablation by Optical Coherence Tomography : Implications on Safety and The Birth of Electro-structural Substrate-Guided Ablation," The Journal of Innovations in Cardiac Rhythm Management, vol. 2, no. March, pp. 199–201, 2011.

[88] Laser Institute of America, "American National Standard for Safe Use of Lasers ANSI Z136," 2007.

[89] X. L. Dean-Ben, A. Buehler, V. Ntziachristos, and D. Razansky, "Accurate model-based reconstruction algorithm for three-dimensional optoacoustic tomography," IEEE Transactions on Medical Imaging, vol. 31, no. 10, pp. 1922–1928, 2012.

[90] G. A. Pang, E. Bay, X. L. Deán-Ben, and D. Razansky, "Three-dimensional optoacoustic monitoring of lesion formation in real time during radiofrequency catheter ablation.," Journal of cardiovascular electrophysiology, vol. 26, no. 3, pp. 339–45, 2015.

[91] S. Thomsen, S. Jacques, and S. Flock, "Microscopic Correlates of Macroscopic Optical Property Changes During Thermal Coagulation of Myocardium," in SPIE Vol. 1202 Laser-Tissue Interaction, vol. 1202, pp. 2–11, 1990.

[92] J. W. Pickering, S. Bosman, P. Posthumus, P. Blokland, J. F. Beek, and M. J. van Gemert, "Changes in the optical properties (at 632.8 nm) of slowly heated myocardium.," Applied optics, vol. 32, pp. 367–371, 1993.

[93] D. E. Haines and D. D. Watson, "Tissue heating during radiofrequency catheter ablation: a thermodynamic model and observations in isolated perfused and superfused canine right ventricular free wall.," Pacing and clinical electrophysiology : PACE, vol. 12, pp. 962–976, 1989.

[94] D. Schwartzman, J. F. Ren, W. A. Devine, and D. J. Callans, "Cardiac swelling associated with linear radiofrequency ablation in the atrium," Journal of Interventional Cardiac Electrophysiology, vol. 5, pp. 159–166, 2001.

[95] H. Nakagawa, W. S. Yamanashi, J. V. Pitha, M. Arruda, X. Wang, K. Ohtomo, K. J. Beckman, J. H. McClelland, R. Lazzara, and W. M. Jackman, "Comparison of in vivo tissue temperature profile and lesion geometry for radiofrequency ablation with a saline-irrigated electrode versus temperature control in a canine thigh muscle preparation.," Circulation, vol. 91, pp. 2264–2273, 1995.

[96] D. Panescu and J. Whayne, "Three-dimensional finite element analysis of current density and temperature distributions during radio-frequency ablation," IEEE TRANSACTIONS ON BIOMEDICAL ENGINEERING, vol. 42, no. 9, 1995.